Dissipative Fluid Dynamics for Ultra-Relativistic Nuclear Collisions

by

Victor Roy

Enrolment No.- PHYS04200704003

Variable Energy Cyclotron Centre, Kolkata-700064, India.

A thesis submitted to
The Board of Studies in **Physical Sciences**
In the partial fulfillment of the requirements
For the Degree of

Doctor of Philosophy

of

HOMI BHABHA NATIONAL INSTITUTE

April, 2012

Homi Bhabha National Institute

Recommendation of the Viva Voce Board

As members of the Viva Voce Board, we certify that we have read the dissertation prepared by **Victor Roy** entitled **Dissipative Fluid Dynamics for Ultra-Relativistic Nuclear Collisions** and recommend that it may be accepted as fulfilling the dissertation requirement for the degree of Doctor of Philosophy.

.....**Date:**

Chairman- Prof. D. K. Srivastava

.....**Date:**

Convener- Prof. A. K. Chaudhuri

.....**Date:**

Member 1- Prof. J. Alam

.....**Date:**

Member 2- Prof. M. G. Mustafa

Finally approval and acceptance of this dissertation is contingent upon the candidate's submission of the final copies of the dissertation to HBNI. I hereby certify that I have read this dissertation prepared under my direction and recommend that it may be accepted as fulfilling the dissertation requirement.

Date:

Place:

STATEMENT BY AUTHOR

This dissertation has been submitted in partial fulfillment of requirements for an advanced degree at Homi Bhabha National Institute (HBNI) and is deposited in the Library to be made available to borrowers under rules of the HBNI.

Brief quotation from this dissertation are allowable without special permission, provided that accurate acknowledgment of source is made. Requests for permission for extended quotation from or reproduction of this manuscript in whole or in part may be granted by the Competent Authority of HBNI when in his or her judgment the proposed use of the material is in the interests of scholarship. In all other instances, however, permission must be obtained from the author.

Victor Roy

DECLARATION

I, hereby declare that the investigation presented in the thesis has been carried out by me. The work is original and has not been submitted earlier as a whole or in part for a degree/diploma at this or any other Institution/University.

Victor Roy

Acknowledgments

I would like to thank my supervisor Dr. A.K. Chaudhuri for his continuous support and careful supervision throughout the PhD period. The second person without whose constant support and inspiration this work would have not been complete is Dr. Bedangadas Mohanty. I would like to express my sincere gratitude to both of them. I was also fortunate to have Dr. Dinesh K. Srivastava (Head Physics Group), Dr. Jan-e Alam, and Dr. M.G. Mustafa as the members of my doctoral committee. I would like to thank them all for helpful suggestions and useful physics discussions. It is also my pleasure to thank the former director Prof. Bikash Sinha and the present director Dr. Rakesh Kumar Bhandari of the Variable Energy Cyclotron Centre (VECC), Dean academics of Homi Bhabha National Institute (HBNI) Dr. Partha Barat, and the head theoretical physics division Dr. Santanu Pal for providing me the opportunity to carry out my research work at VECC.

It was a pleasure to collaborate with the following colleagues at VECC, Dr. Subhasis Chattopadhyay, Dr. Sourav Sarkar, Dr. Sidharth K. Prasad, Mr. Partha P. Bhaduri, Mr. Santosh K. Das, Mr. Sabyasachi Ghosh, and Ms. Payal Mohanty. It was also a pleasure to have following people as friends and colleagues at VECC, Dr. Rupa Chatterjee, Dr. Mriganka M. Mandal, Dr. Saikat Biswas, Dr. Tapasi Ghosh, Dr. Arnomitra Chatterjee, Dr. Umme Jamil, Mr. Prasun S. Chaudhuri, Dr. Sharmishtha Banik, Mr. Jajati K. Nayak, Mr. Haridas Pai, Mr. Prithwish Tribedy, Mr. Pratap Roy, Mr. Amlan Dutta, Mr. Somnath De, Mr. Sudipan De, Mr. Md. Younus, Mr. Nihar R. Sahoo, Mr. Arnab Banerjee, Mr. Manish R. Gohil, Mr. Subhash Singha,

Mr. Md. Nasim, Mr. Abhishek Mishra, Mr. Amal Giri, Mr. Trambak Bhattacharjee, Ms. Sukanya Mitra, Ms. Surasree Mazumder, Md. Rihan Haque, Mr. Sumit Basu, Mr. Arindam Roy, Mr. Subikash Choudhury, Ms. Maitreyee Mukherjee, Mr. Vishal Srivastava, Mr. Balaram Dey, and Mr. Sanoar Molla.

In the first year of the PhD program at VECC, we went through a one year of detail pre-doctoral course. I am thankful to the teachers of this course for their wonderful teaching. Throughout the whole research period I have extensively used and benefited from the computing facility at VECC provided by the computer and informatics group. I am thankful to the administrative, library, accounts, and canteen/guest house staff of VECC for their co-operation.

During the PhD period, I got the opportunity to attend and deliver a talk at the Berkeley School on Collective Dynamics held at the Lawrence Berkeley National Laboratory, Berkeley, California. I would like to thank the organizers of the school, specially Dr. Nu Xu, for their support and Department of Science and Technology, Govt. of India, for generously providing the funding to attend the school. I have also attended and delivered talks at the International School on High-Energy Nuclear Collisions and the 7th International Workshop on Critical Point and Onset of Deconfinement, Wuhan, China. I would like to thank the organizers of the school/workshop and the Homi Bhabha National Institute, Department of Atomic Energy, India for their kind support. I express my sincere thanks to Professor Sourendu Gupta for inviting me for an academic visit to Tata Institute of Fundamental Research, Mumbai and to TPSC for the travel support. I presented my first plenary talk at the Workshop on High En-

ergy Physics and Phenomenology (WHEPP-2012) organized at Mahableswar by TIFR, Mumbai. I would like to thank DAE-SRC project of Dr. Mohanty, project sanction No. 2010/21/15-BRNS/2026 for providing partial travel support. I was fortunate to be able to attend the Quark Matter Conference held at Jaipur, 2008, and ICPAQGP - 2010 at Goa, the experience of meeting several scientists of our field at one place was quite unique. I would like to thank the organizers of the conferences for providing me with this opportunity.

Like thousands of physics students, I am inspired by the famous three volumes of the lectures by Professor Richard P. Feynman, to pursue the research in the field of high energy physics. I would like to thank Professor Chirantan Neogy of University of Kalyani for his encouragement to pursue research in physics.

Finally, I would like to express my most sincere thanks to my parents for their constant support throughout the research period.

List of Publications

1. **2+1 dimensional hydrodynamics including bulk viscosity: A Systematics study.**

   Victor Roy, A.K. Chaudhuri.

   Published in Phys. Rev. C. 85 (2012) 024909.

2. **Charged particle's elliptic flow in 2+1D viscous hydrodynamics at LHC ($\sqrt{s_{NN}}$ = 2.76 TeV) energy in Pb+Pb collision.**

   Victor Roy, A.K. Chaudhuri.

   Published in Phys. Lett. B 703 (2011) 313.

3. **Elliptic flow of thermal dilepton as a probe of QCD matter.**

   Payal Mohanty, **Victor Roy,** Sabyasachi Ghosh, Santosh K Das, Bedangadas Mohanty, Sourav Sarkar, Jane Alam, Asis K Chaudhuri.

   Published in Phys. Rev. C. 85 (2012) 031903.

4. **Hydrodynamical analysis of centrality dependence of charged particle's multiplicity in $\sqrt{s_{NN}}$ = 2.76 TeV Pb+Pb collision.**

   A.K. Chaudhuri, **Victor Roy.**

   Published in Phys. Rev. C . 84 (2011) 027902.

5. **Hadronic resonance gas and charged particle's p_T spectra and elliptic flow in $\sqrt{s_{NN}}$ = 200 GeV Au+Au collisions.**

   Victor Roy, A.K. Chaudhuri.

   Published in Phys. Rev. C 82 (2010) 031901.

6. **Transverse Momentum Spectra and Elliptic Flow in Ideal Hydrodynamics and Geometric Scaling.**

   Victor Roy, A.K. Chaudhuri.

   Published in Phys. Rev. C 81 (2010) 067901.

7. **Elliptic flow (v_2) in pp collisions at energy available at the CERN Large Hadron Collider: A hydrodynamical approach.**

   S.K. Prasad,**Victor Roy,** S. Chattopadhyay , A.K. Chaudhuri.

   Published in Phys. Rev. C 82 (2010) 024909.

8. **Equation of state dependence of Mach cone like structures in Au+Au collisions.**

   Victor Roy, A.K. Chaudhuri.

   Published in J.Phys.G 37 (2010) 035105.

Papers Communicated

1. **Comparison of results from a 2+1D relativistic viscous hydrodynamic model to elliptic and hexadecapole flow of charged hadrons measured in Au-Au collisions at $\sqrt{s_{\rm NN}}$ = 200 GeV.**

   Victor Roy, A. K. Chaudhuri and Bedangadas Mohanty.

   Submitted to the Physical Review C. e-Print: arXiv:1204.2347.

2. **Fluctuating initial condition and smoothening effect on elliptic and triangular flow.**

   Md.Rihan Haque, **Victor Roy,** A. K. Chaudhuri.

   Submitted to the Physical Review C. e-Print: arXiv:1204.2986.

Conference proceedings

1. **Transverse Momentum Spectra and Elliptic Flow in Ideal Hydrodynamics and Geometric Scaling.**

   Victor Roy, A. K. Chaudhuri.

   Proceeding of the DAE Symp. On Nucl. Phys. 55 (2010) 582.

2. **Lattice Based Equation and Transverse Momentum Spectra of Identified Particles in Ideal and Viscous Hydrodynamics.**

   Victor Roy, A. K. Chaudhuri.

   Proceeding of the DAE Symp. On Nucl. Phys. 55 (2010) 624.

3. **Charged particle p_T spectra and elliptic flow in a 2+1D viscous hydrodynamics including shear and bulk viscosity.**

   Victor Roy, A K Chaudhuri.

   Proceeding of the DAE Symp. On Nucl. Phys. 56 (2011) 844.

4. **Probing elliptic flow of QCD matter by lepton pairs.**

   Payal Mohanty,**Victor Roy,** Sabyasachi Ghosh, Santosh K Das, Bedangadas Mohanty, Sourav Sarkar, Jan-e Alam, Asis K Chaudhuri.

   Proceeding of the DAE Symp. On Nucl. Phys. 56 (2011) 856.

5. **Transport properties of the matter formed in heavy-ion collisions at the Large Hadron Collider.**

   Victor Roy, A K Chaudhuri.

   Proceeding of the DAE Symp. On Nucl. Phys. 56 (2011) 910.

Synopsis

Nuclear collisions at relativistic energies are extensively used to study the properties of Quantum Chromodynamic (QCD) vacuum. At high temperature and pressure, QCD matter can undergo a confinement-deconfinement transition. The deconfined state of quarks and gluons is commonly called as the Quark-Gluon-Plasma (QGP). Recent experiments at the Relativistic Heavy Ion Collider (RHIC) at Brookhaven National Laboratory and at the Large Hadron Collider (LHC) at CERN have provided strong indications that in central heavy-ion collisions, a QGP state is formed.

Relativistic hydrodynamics provides a useful tool to analyze the experimental data from the relativistic heavy-ion collisions. It is assumed that in such a collision a fireball is produced. Constituents of the fireball collide frequently to establish local thermal equilibrium sufficiently fast and after a certain time τ_0, hydrodynamics becomes applicable. If the macroscopic properties of the fluid e.g. local energy density, pressure, fluid velocity etc. are known at the equilibration time τ_0, the relativistic hydrodynamic equations can be solved to give the space-time evolution of the fireball. The evolution proceeds as per the input equation of state (EoS), which is a thermodynamic relation between the energy density, pressure, and number density of the fluid. EoS may or may not include phase transition. Hydrodynamics models are unique, because the phenomena of phase transition can be explicitly incorporated via EoS. When the interactions between the constituents are too weak (mean free path comparable/larger than the system size) the hydrodynamic evolution ends and freeze-out occurs. Using suitable algorithm (e.g. Cooper-Frye), the fluid information at the freeze-out can be converted

into the invariant distribution for particle, which can then be directly compared with the experimental data. The mass dependence of slope of invariant yields of produced hadrons as a function of transverse momentum (p_T) and elliptic flow value at low p_T (< 1 GeV) observed in experimental data provides support for applying relativistic hydrodynamics to high energy heavy-ion collisions.

Ideal hydrodynamics has been extensively used for comparison with the experimental RHIC data. Theoretical calculations (QCD and AdS/CFT based) indicate presence of finite dissipative effects for the temperature range achieved in collisions at RHIC and LHC. In addition, the centrality dependence of elliptic flow measurements at RHIC also indicates that dissipative effects need to be considered in hydrodynamic simulations. This dissertation focuses on understanding the dissipative effects in the QCD matter formed in the heavy-ion collisions. Specifically we estimate the shear viscosity to entropy density ratio (η/s) by comparing the simulated results from a 2+1D relativistic viscous hydrodynamic model to the experimental data measured at RHIC and LHC.

We will follow the second order Israel-Stewart theory of causal viscous hydrodynamics for the numerical simulation of viscous fluid. Treating shear and bulk viscosity coefficients as input parameters, the evolution of shear and bulk viscous fluid are obtained by solving the energy-momentum conservation and corresponding viscous relaxation equations. The numerical code is named as AZHYDRO-KOLKATA. For our study we have constructed an EoS using lattice QCD data for the QGP phase with the hadron resonance gas EoS for the hadronic phase. We have implemented the necessary equations for bulk viscous evolution of the fluid and bulk viscous correction to the freeze-out

distribution function. These are in addition to the corresponding equations and corrections due to shear viscosity. Details of the temporal evolution of various components of shear and bulk stress, temperature of the fluid, average transverse velocity, and spatial and momentum anisotropy has been studied. The later results have been compared to corresponding values for the ideal fluid evolution. We have also studied in detail the effect of two different temperature dependent bulk viscosity to entropy density (ζ/s) ratio on experimental observables like p_T spectra and elliptic flow. We have followed the Cooper-Frye prescription to obtain the invariant yield of the hadrons. The resonance decay contribution to the thermal pion yields have been considered at a given freeze-out temperature. For the studies involving bulk viscosity we have presented the results of bulk viscous correction to the freeze-out distribution function following the Grad's 14-moment method. Specifically we point out the limitations of this approach. All the simulations have been done assuming finite baryon number density effects are small at top RHIC and LHC energies.

The simulated invariant yield ($dN/d^2p_Td\eta$) and elliptic flow (v_2) of charged hadrons as a function transverse momentum for different collision centralities are compared to the corresponding experimental measurements for Au-Au collisions at $\sqrt{s_{NN}} = 200$ GeV (RHIC) and Pb-Pb collisions at $\sqrt{s_{NN}} = 2.76$ TeV (LHC). The higher beam energy is accounted in the simulations by considering a higher value of initial transverse energy density profile and also larger value of inelastic nucleon-nucleon cross section. We have studied in detail the effect of varying initial energy density profile (by considering a Glauber model and CGC model based initial conditions, as well as varying the hard scattering fraction parameter value in the Glauber based initial condition) on

experimental observables such as pseudorapidity density of charged hadrons ($dN_{ch}/d\eta$), $dN/d^2p_Td\eta$, $v_2(p_T)$ for various collision centralities. The simulations are carried out for various input values of a temperature independent η/s (0.08 - 0.2). The centrality dependence of experimentally measured $dN_{ch}/d\eta$ at RHIC and LHC has been used in our hydrodynamic simulations to fix the corresponding initial conditions. From the simulations we observe that the p_T spectra becomes flatter (average transverse velocity becomes larger) with increase in the input η/s values. While simulated $v_2(p_T)$ values become smaller (momentum anisotropy becomes smaller) with increase in the input η/s values. Comparison of our viscous hydrodynamic simulation results to the experimental data at RHIC and LHC shows that both $dN/d^2p_Td\eta$ and v_2 demands higher values of η/s as we go from central (0-10%) to peripheral collisions (40-50%). We find the observable $v_2(p_T)$ is more sensitive to the viscous effects compared to $dN/d^2p_Td\eta$. Our study suggests that the η/s estimated from the RHIC and LHC data have values around 0.08 - 0.18. A comparison of our estimate of η/s to those obtained by other groups has been discussed in the last chapter of this thesis. The small value of η/s estimated for the QGP system formed in high energy heavy-ion collisions indicate that the system is strongly coupled, where the inter-particle potential energy dominates over the (thermal) kinetic energy of the particles.

Contents

Chapter 1

Introduction

1.1 QCD and QGP

There are four fundamental interactions in nature: (i) Gravitational, (ii) Weak, (iii) Electromagnetic, and (iv) Strong interaction, which governs the behavior of all the known matter. Quantum Chromodynamics (QCD) is the theory of strong interaction. In the 1960's, discovery of a large number of strongly interacting particles (hadrons) and the subsequent explanation of the properties of hadrons by Gell-mann and Zweig suggests that hadrons are not elementary particles, rather it consists of more fundamental particles called quarks. It was then possible to explain the properties of dozens of observed hadrons by considering three kinds (flavor) of quarks and their antiparticles. In 1973 Gross, Wilczek, and Politzer [1, 2] came up with a proposal for a quantum field theory for the strong interactions, QCD, a non-abelian gauge field theory based on the

gauge group SU(3) for quarks with massless vector particles mediating the force. These particles were to be named gluons.

Gluons are like photons, which according to the theory of Quantum electrodynamics are the carrier of electromagnetic force. Photons does not interact with each other [1], whereas the situation becomes complex in the case of strong interaction because the mediator gluons carry color charges and hence interacts with each other.

No free quarks or gluons are observed in nature. They are always confined inside hadrons. The QCD predicts this confinement property, although it is not easy to prove. It was shown by Wilczeck, Gross, and Politzer that the running coupling constant of strong interaction α_s becomes small in the limit of high momentum transfer (Q) between the two colliding partons. This phenomenon is related to the asymptotic freedom [3].

With further advances in QCD, theoretician was now able to understand and predict new phenomenon in the field of nuclear physics at high temperature and density. T.D. Lee proposed that by distributing high energy or high nucleonic density over a relatively large volume one could temporarily restore broken symmetries of the physical vacuum and possibly create novel abnormal dense states of nuclear matter [4, 5]. Collins and Perry [6] realized that the asymptotic freedom property of QCD implies the existence of an ultra-dense form of matter with deconfined quarks and gluons, called the Quark-Gluon Plasma (QGP) [7].

[1] At very high energies non-linear phenomenon occurs where photon can interact among themselves, J.D. Jackson, Classical Electrodynamics,Third Edition.

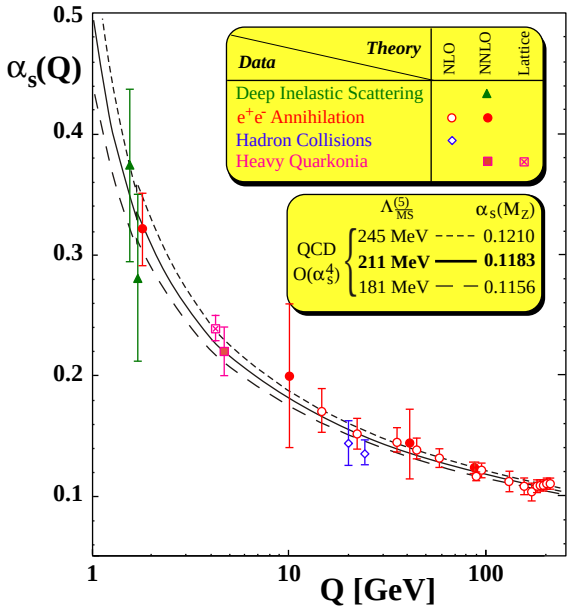

Figure 1.1: Summary of the measurements of $\alpha_s(Q)$ as a function of Q. Perturbative QCD calculations are shown by the lines. The figure is from reference [8].

Depending upon the value of strong coupling constant α_s, QCD theory is broadly divided into two main regimes : (i) Perturbative: where the value of α_s is small such as in the collision of two partons where the momentum transfer is large. Perturbative QCD calculation shows excellent agreement with the experimental estimates of α_s as shown in figure 1.1 [8].

(ii) Non-perturbative: where the value of α_s is large. In this regime, the perturbative QCD calculation breaks down. One way to do a first principle calculation in the non-pertubative regime is through numerical simulations on a space-time lattice. This can be further divided into two cases. (a) In the zero temperature region, lattice QCD (lQCD) calculations of mass of hadrons has good agreement with the experimentally measured masses as shown in figure 1.2. In the zero temperature limit, lQCD also predicts the

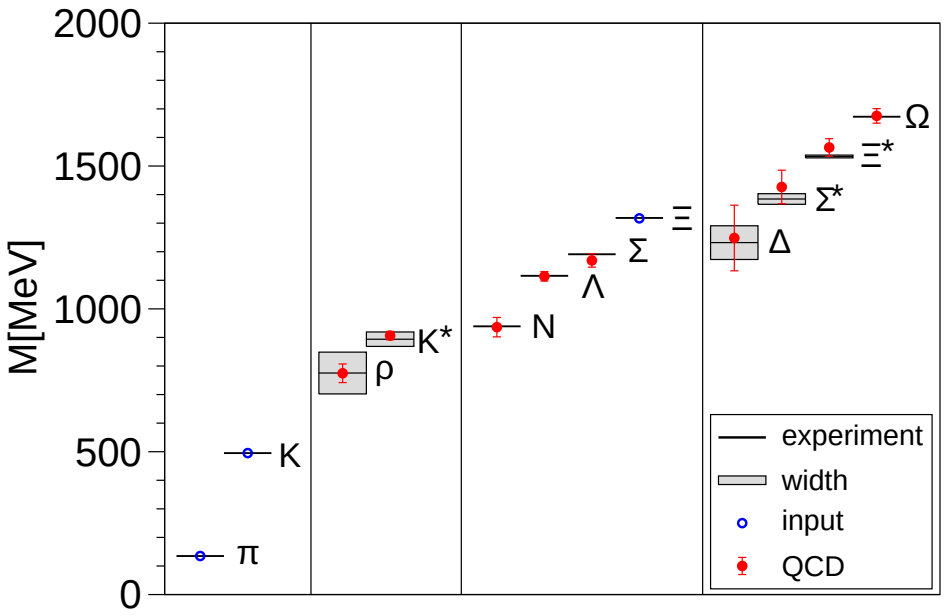

Figure 1.2: The light hadron spectrum of QCD. Horizontal lines and bands are the experimental values with their decay widths. Symbols are lattice QCD calculation by Durr et al. [9].

breaking of chiral symmetry. (b) In the high temperature limit lQCD predicts that chiral symmetry will be restored. It also predicts the phenomenon of deconfinement where the colorless hadrons will decompose into quarks and gluons or formation of QGP. According to the recent lQCD calculation with 2+1 flavor and for realistic quark masses, the quark-hadron transition should occur at a cross over temperature ($T_{\rm co}$) $\sim$ 175 MeV [10].

Figure 1.3 shows the entropy density over cube of the temperature from a lQCD calculation with 2+1 flavor as a function of temperature [10]. For relativistic particles, to a very good approximation, $s/T^3 = \frac{2\pi^2}{45} g_{\rm eff}$. Where $g_{\rm eff}$ is the effective degrees of freedom of the system. From figure 1.3 at low temperatures $\sim$ 110 MeV the $g_{\rm eff}$ $\sim$

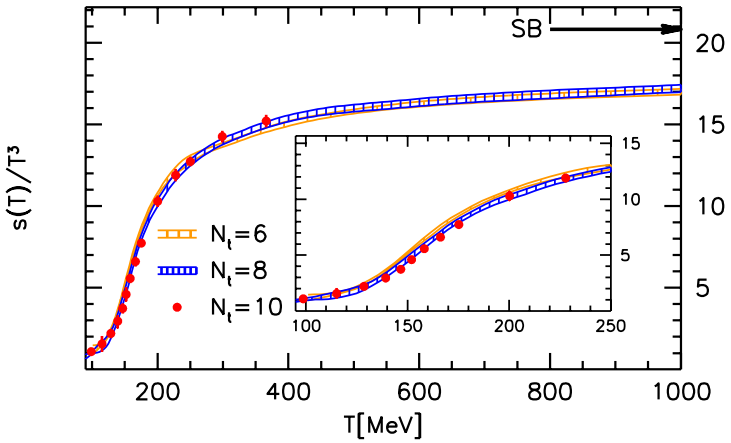

Figure 1.3: Lattice QCD results of entropy density (s) normalized by T^3 as a function of the temperature (T) [10]. The Stefan-Boltzmann limit $s_{\rm SB} = 4P_{\rm SB}/{\rm T}$ is indicated by an arrow.

3.4. For a system of pion gas the effective degrees of freedom is around 3. At high temperatures $\sim$ 250 MeV the $g_{\rm eff} \sim 30$. For a massless system of quarks with 3 flavors, their anti-particles and gluons the $g_{\rm eff} = (g_{\rm gluon} + \frac{7}{8} g_{\rm quark}) = (8 \times 2 + \frac{7}{8} N_{\rm c} N_{\rm f} N_{\rm s} N_{\rm a}) = 47.5$. Where $N_{\rm c}$ is the number of colors = 3, $N_{\rm f}$ is the number of flavors = 3, $N_{\rm s}$ is the spin degrees of freedom = 2, and $N_{\rm a} = 2$ is the degrees of freedom for the particles and anti-particles. So lQCD predicts a transition from a state where quarks and gluons are confined inside hadrons (relevant degrees of freedom are hadronic) to a state where quarks and gluons are deconfined (relevant degrees of freedom are partons) at high temperatures. The s/T^3 value does not reach the Stefan-Boltzmann limit for a non-interacting massless system of quarks and gluons, indicating that the system of quarks and gluons in the temperature range 170 - 1000 MeV is strongly interacting.

The formation of QGP in the laboratory is possible by colliding heavy ions at relativistic energies as it is done at Relativistic Heavy Ion Collider (RHIC) or Large Hadron

Collider (LHC) experiments. Results from these experiments (presented in the section on QGP signatures) as well as the lQCD calculations discussed above indicates the formation of a strongly coupled QGP (sQGP). The strongly coupled quark-gluon plasma is in many ways similar to certain kinds of conventional (electromagnetic) plasmas consisting of electrically charged particles (electrons, ions or large charged mesoscopic grains), which also exhibit liquid or even solid-like behavior. The strongly coupled plasmas are characterized by an inter-particle potential energy which dominates over the (thermal) kinetic energy of the particles. Strongly coupled plasmas occur in electrical discharges, in cryogenic traps and storage rings, in semiconductors, and in astrophysical systems (interior of giant planets and white dwarfs) [11].

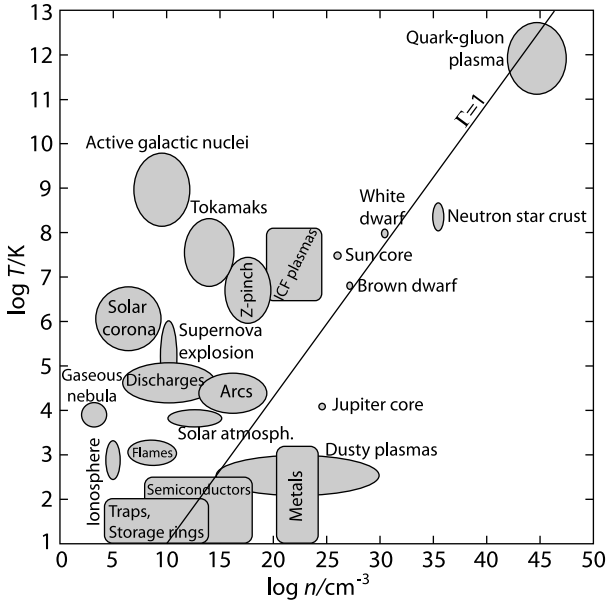

Figure 1.4: Different types of plasmas over the density (n) - temperature (T) plane. Strongly coupled plasmas are located right from the $\Gamma = 1$ line. Γ characterizes the ratio of the potential to kinetic energy. The figure is from reference [11]

.

Figure 1.4 illustrates the different plasma types over temperature - density plane.

Besides the conventional plasmas, the approximate location of the sQGP is also shown. Strongly coupled systems are characterized by the coupling parameter Γ which is the measure of the ratio of average potential energy to the average kinetic energy per particle. The strong coupling regime corresponds to $\Gamma > 1$. Recent work indicates that the coupling parameter for the sQGP is expected to be in the order of one [12, 13, 14, 15, 16, 17]. Understanding the transport properties of the sQGP is one of the main motivations of this thesis work.

Now we will discuss about the space-time evolution of the system formed in relativistic heavy-ion collisions and give a brief note on the different experimental facilities for high energy heavy-ion collisions.

1.2 Relativistic Heavy Ion Collision

1.2.1 Space-time evolution

Figure 1.5 shows different stages of heavy-ion collision schematically. The proper time axis (τ) is along the horizontal direction. Though there are no sharp boundaries between different stages as shown in figure 1.5, we can broadly divided the whole evolution into the following sub-stages.

- **Initial stage :** In the initial stage two nuclei approaching each other with relativistic speed. Because of their high speed, the colliding nuclei are highly Lorentz

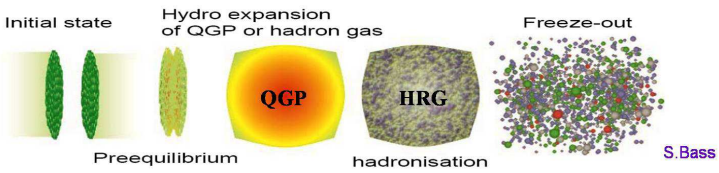

Figure 1.5: Schematic diagram illustrating the different stages of evolution for heavy-ion collisions at relativistic energies. The figure is from [18].

contracted along the direction of motion. According to the convention at $\tau = 0$ two nuclei collides. Before collision, the distributions of quarks and gluons in the colliding nucleus are described by the corresponding structure functions.

- **Pre-equilibrium stage :** After collision ($\tau > 0$), a large amount of initial kinetic energy of the incoming nucleons are deposited into a very small region of the reaction zone. Strong interaction between quarks and gluons of the colliding nucleons helps to achieve local thermal equilibrium quickly around $\tau \sim 1$fm. After thermalization, the quarks, antiquarks, and gluons of the thermalized medium follows the corresponding Fermi-Dirac or Bose-Einstein distributions. Heavy quark pairs such as $s\bar{s}$, $c\bar{c}$ and high energetic photons are also produced in the primary collision between two partons of the colliding nucleus in this early stages of evolution.

- **QGP evolution :** The state of the thermalized QGP can be described by a few thermodynamic variables like local temperature, pressure, energy density etc. The pressure gradient which builds up in the process of thermalization drives the QGP in the radially outward directions. The system expands and cools down. The space-time evolution of the QGP can be described by a relativistic hydrodynamics simulation. When the temperature of the QGP drops below a critical value (lQCD predicted cross over temperature), quarks and gluons and their corresponding

antiparticles forms colorless hadrons. This process is known as hadronization. In figure 1.6 we depict the constant temperature contours corresponding to $T_{\rm co}$ = 175 MeV and freeze-out temperature of 130 MeV in the τ - x plane (at $y = 0$) indicating the boundaries for the QGP and hadronic phases respectively. The life time of the QGP phase $\sim$ 6 fm and the duration of the hadronic phase is $\sim$ 6 - 12 fm. These contours are obtained from a relativistic ideal hydrodynamics, details of which will be discussed in chapter-2.

- **Hadron gas and freezeout :** The hadron gas, consists of stable and unstable hadrons, further expands and cools down until the mean free path of the constituent hadrons becomes large compared to the system size. When this happen, hadrons no longer collides among themselves and their momentum distribution remains unchanged hereafter. This is called kinetic freezeout. There is another freezeout called chemical freezeout. According to the statistical model calculation, the chemical freezeout happens in the hadronic phase, just after the hadronization, corresponds to the time when inelastic collisions ceases. Post chemical freezeout, the ratio of the number of different kinds of particles remains unchanged.

Hydrodynamics is believed to be applicable from the thermalization until kinetic freezeout. The typical time duration is of the order of $\sim$10-15 fm depending on the collision centrality. Using a smooth Glauber based initial condition, followed by subsequent space-time evolution within the framework of a relativistic 2+1D viscous hydrodynamics and a freeze-out prescription based on Cooper-Frey method we will attempt to understand the evolution of the system formed in heavy-ion collisions at RHIC and LHC in this thesis.

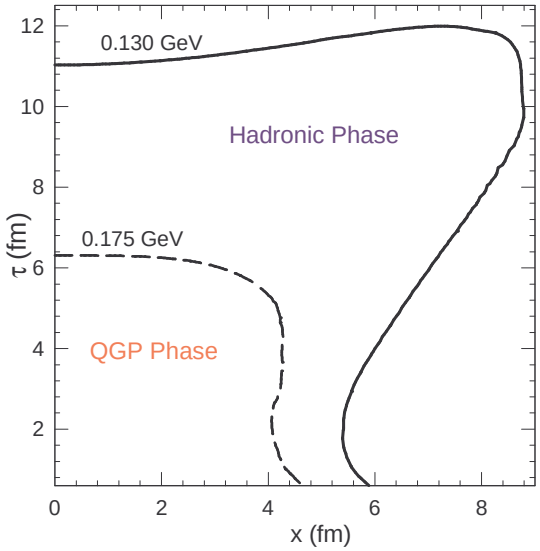

Figure 1.6: Constant temperature contours denoting the space-time boundaries of the QGP and hadronic phases in the τ-x plane (at y=0).

1.2.2 Experimental facilities

The first heavy ion collisions at relativistic energies were undertaken at the Lawrence Berkeley National Laboratory, LBNL, at Berkeley, USA, and at the Joint Institute for Nuclear Research, JINR, in Dubna, USSR. At the Bevatron in LBNL, the energy scale was at the level of 1-2 GeV per nucleon. The aim was to study the particle production from the nuclear matter with densities at few times normal nuclear matter density. The demonstration of the possibility of studying the properties of compressed and excited nuclear matter motivated further research programs at much higher energies. The fixed target experiments with relativistic nuclei in the energy range $\sqrt{s_{\rm NN}}$=4 - 20 GeV were carried out in the years 1987 - 1994. The projectile ions varied from Sulphur, Silicon, Oxygen, Gold, Nickel, Niobium, Indium, and Lead. The experiments made use of the Alternate Gradient Synchrotron (AGS) facility at Brookhaven National Laboratory

(BNL) and Super Proton Synchrotron (SPS) facility at the European centre of research in nuclear physics (CERN). The first high energy heavy-ion collider experiments started in 1999 at the Relativistic Heavy-Ion Collider (RHIC) facility at BNL and later at the Large Hadron Collider (LHC) at CERN in the year 2010. At RHIC the $\sqrt{s_{\rm NN}}$ range covered was between 7.7 to 200 GeV. The colliding ions includes Proton, Deuteron, Copper, and Gold. At LHC the heavy-ion collision data has been taken at $\sqrt{s_{\rm NN}} = 2.76$ TeV, with the future plan to raise it to 5.5 TeV. The dominant colliding ion species is Pb-Pb.

Table 1.1 shows various high energy heavy-ion accelerator facilities, their year of commissioning, colliding systems, and approximate highest $\sqrt{s_{\rm NN}}$ values. Figure 1.7

Table 1.1: Heavy Ion Collision.

Year	Accelerators	Colliding systems	Colliding energy
1987	BNL AGS	Au-Si (fixed target)	5 GeV
1987	CERN SPS	Pb-S (fixed target)	20 GeV
1992	BNL AGS	Au-Au (fixed target)	4 GeV
1994	CERN SPS	Pb-Pb (fixed target)	17 GeV
2000	BNL RHIC	Au-Au (collider)	200 GeV
2010	CERN LHC	Pb-Pb (collider)	2760 GeV

shows the charged particle pseudorapidity density ($dN_{\rm ch}/d\eta$) per average number of participating nucleon ($< N_{\rm part} >$) pair as a function of $\sqrt{s_{\rm NN}}$ for heavy-ion and p-p collisions [19]. The charged particle production seems to have a power law dependence on the $\sqrt{s_{\rm NN}}$ for both heavy-ion and p-p collisions, with the rate of increase in multiplicity being faster for heavy-ion collisions compared to p-p collisions. The $dN_{\rm ch}/d\eta$ is one among the several observables measured in the experiments, other relevant observables used in this thesis are the invariant yields of charged hadrons ($\frac{d^2N}{2\pi p_{\rm T} dp_{\rm T} d\eta}$) and elliptic

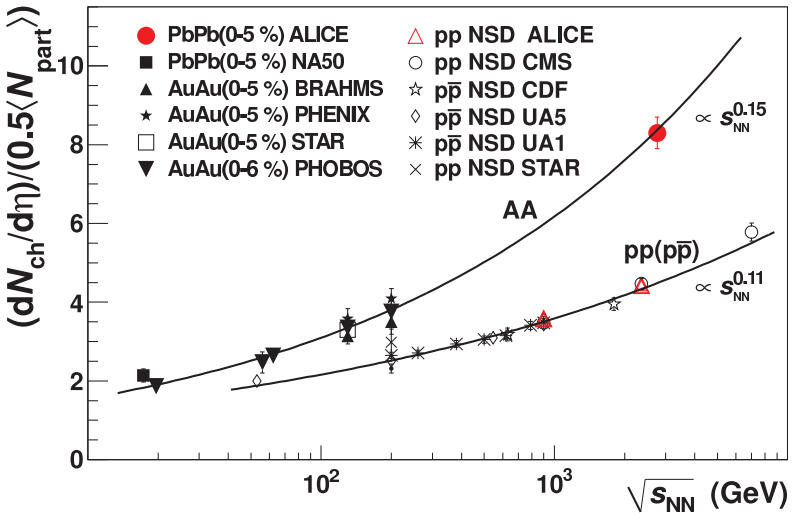

Figure 1.7: Charged-particle pseudorapidity density per participant pair for central nucleus-nucleus and non-single diffractive pp ($p\overline{p}$) collisions, as a function of $\sqrt{s_{\rm NN}}$ [19].

flow (v_2). Both of these observables are discussed in chapter- 5. A brief discussion of elliptic flow as a signature of QGP is given in the next section of this chapter.

1.2.3 Theoretical models

We have discussed earlier that in this thesis we are interested in modeling the evolution of QGP and subsequent hadronic matter by using relativistic hydrodynamics for relativistic heavy ion collision. The evolution phase of the QGP and hadronic matter can be alternatively simulated in a relativistic transport model.

Thus we have two Lorentz-covariant dynamical frameworks at our disposal: (i) relativistic hydrodynamics and (ii) covariant transport theory. They represents opposite limits in their underlying assumptions: the first is a macroscopic description and as-

sumes approximate local thermal equilibrium. The details of relativistic hydrodynamics is discussed in chapter-2. The second provides a microscopic description of the system and is suited for the early and late non-equilibrium stages. Transport theories based on parton degrees of freedom can also describe the early thermalization processes. The late hadronic rescattering and freeze-out stage requires a description in terms of a covariant hadron cascade and can be matched to the earlier hydrodynamic evolution of QGP phase [20]. Some of the typical transport based calculations are A Multi Phase Transport (AMPT) model [21] and Ultra Relativistic Quantum Molecular Dynamic (URQMD) model [22]. All these theoretical descriptions are well-developed and can be further advanced.

Research on hydrodynamics as is carried out in this thesis mainly focuses on viscous effects and the extraction of the QGP viscosities from experimental hadron data at low transverse momentum ($p_{\mathrm{T}} < 3$ GeV). The most dramatic effect of shear viscosity (η) is its ability to inhibit the buildup of anisotropic collective flow, thereby reducing the elliptic flow of the emitted final-state hadrons. In heavy-ion collisions, these effects are strong due to large expansion rates, especially at early times. Hence, the elliptic flow is considered as one of the sensitive observable to phenomenologically constraint even a small value of shear viscosity to entropy density ratio (η/s) of the fluid.

However, a quantitative determination of η/s of QGP requires comparison of the experimental data with a full-simulation model which incorporates all the stages of the evolution from pre-equilibrium to freezeout. It should be borne in mind that the precise determination of η/s depends on the uncertainties of various model parameters. To

reduce this uncertainty in such an extraction process of η/s by comparing experimental data to model calculations, a judicious comparison of the results from hydrodynamic approach with transport theory will be helpful.

1.3 QGP Signatures

1.3.1 Jet quenching

One of the most exciting results obtained at RHIC is the discovery of suppression in the production of high transverse momentum ($p_{\rm T}$) mesons in nucleus-nucleus collisions compared to corresponding data from p-p collisions scaled with the number of binary collision [23, 24, 25, 26]. This phenomena is called as the jet quenching in a dense partonic matter [27] and has been interpreted in terms of energy loss of partons in QGP. The energy loss by energetic partons traversing the hot and dense medium formed in high-energy heavy-ion collisions is predicted to be proportional to both the initial gluon density [28, 29] and the lifetime of the dense matter [30]. The results on high-$p_{\rm T}$ suppression of mesons are usually expressed in terms of the nuclear modification factor ($R_{\rm AA}$), defined as:

$$R_{\rm AA} = \frac{dN_{\rm AA}/dyd^2p_{\rm T}}{T_{\rm AB}d\sigma_{\rm NN}/dyd^2p_{\rm T}} \tag{1.1}$$

where the overlap integral $T_{\rm AB} = N_{\rm binary}/\sigma^{pp}_{\rm inelastic}$ with $N_{\rm binary}$ being the number of binary collisions estimated from Glauber model calculation [31].

In figure 1.8 we show the experimental data (symbols) for the $R_{\rm AA}(p_{\rm T})$, for various

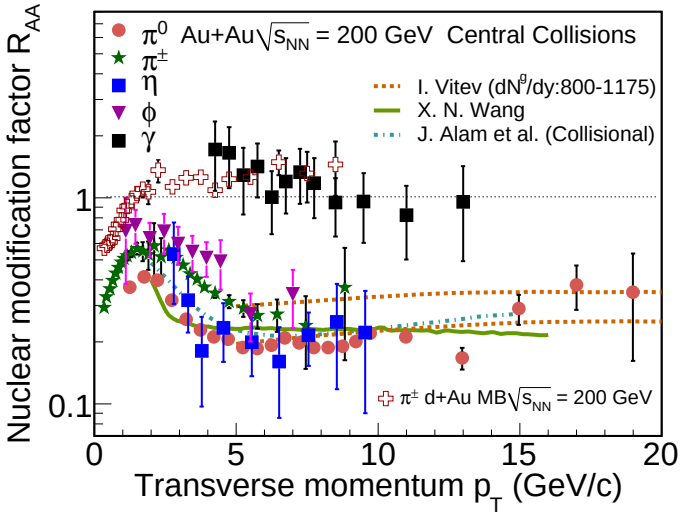

Figure 1.8: The nuclear modification factor ($R_{\rm AA}$) for mesons and direct photons as measured in RHIC experiments at midrapidity for central Au-Au collisions at $\sqrt{s_{\rm NN}}$ = 200 GeV [32]. Also shown are the $R_{\rm dAu}$ for charged pions for $\sqrt{s_{\rm NN}}$ = 200 GeV. The lines are results from various model calculations. See text for more details.

produced mesons [33, 34, 35] and direct photons [36] in the central Au-Au collisions at midrapidity. A large suppression in high $p_{\rm T}$ meson production is observed, and those for π^0's being almost flat at $R_{\rm AA} \simeq 0.2$ up to 20 GeV. From figure 1.8 it is clear that the level of suppression for π^0's, η's, and ϕ-mesons are very similar, which supports the conclusion that the suppression occurs in the partonic phase, not in the hadronic phase. This strong suppression of meson production is in contrast to the behavior of direct photons, also shown in the figure 1.8 by filled black boxes. The direct photons follow binary scaling (i.e. $R_{\rm AA} \simeq 1$) or no suppression. This observation is a strong evidence that the suppression is not an initial state effect, but a final state effect caused by the high density medium with color charges created in the collision. This is further supported by the experimental measurement from deuteron on Au ion collisions, which gave a $R_{\rm dAu}(p_{\rm T}) \sim 1$ for $\pi^{\pm}$ at midrapidity and high $p_{\rm T}$ [37].

The various curves in figure 1.8 are different theoretical calculations. The dashed curve shows a theoretical prediction using the GLV parton energy loss model [28, 29] . The model assumes an initial parton density $dN/dy = 800 - 1100$, which corresponds to an energy density of approximately 5-15 GeV/fm^3. The solid curves are predictions from reference [30].The parton energy loss calculations discussed above attributes the opacity to plasma induced radiation of gluons, much like ordinary bremsstrahlung of photons by electrons. The dot-dashed curve in figure 1.8 is a theoretical result on $R_{\rm AA}$ by considering only the collisional energy loss [38].

1.3.2 Elliptic flow

The elliptic flow coefficient v_2 measured in high energy heavy-ion collision is an important observable. Elliptic flow is a measure of anisotropy of the momentum distribution of the produced particles for non-central nucleus nucleus collision [39]. The elliptic flow is defined as [40]

$$v_2 = \langle cos2(\phi - \Psi) \rangle \,, \tag{1.2}$$

where ϕ is the azimuthal angle of the particle and Ψ is the azimuthal angle of impact parameter. The angular bracket denotes the averaging over particles and events.

Alternatively, the momentum distribution of the produced hadrons in the azimuthal direction can be decomposed into a Fourier series in ϕ as

$$\frac{dN}{p_{\rm T} dp_{\rm T} d\phi dy} = \frac{dN}{2\pi p_{\rm T} dp_{\rm T} dy} \left[1 + 2 \sum_{1}^{\infty} v_{\rm n} cos \left[n \left(\phi - \Psi \right) \right] \right] . \tag{1.3}$$

Where $v_{\rm n}$'s are various order of flow harmonics, v_1 is the directed flow, v_2 is the elliptic flow, v_3 is triangular flow and so on.

In non-central heavy-ion collisions, the initial spatial anisotropy of the almond shape overlap region of the colliding nuclei is transformed into an anisotropy in momentum space through interactions between the particles. As the system expands, anisotropy is reduced and the system becomes more spherical, thus the driving force quenches itself. Therefore the elliptic flow is sensitive to the collision dynamics in the early stages.

The left panel of figure 1.9 shows the experimentally measured v_2 as a function of $p_{\rm T}$ of $\pi^{\pm}$, $K^0_{\rm s}$, $\bar{p}$ and $\Lambda + \bar{\Lambda}$ for minimum bias Au-Au collision at $\sqrt{s_{\rm NN}} = 200$ GeV [41]. Hydrodynamics calculations assuming early thermalization, ideal fluid expansion, an equation of state consistent with lattice QCD calculations including a phase transition at T_c=165 MeV, and a sharp kinetic freezeout at a temperature of 130 MeV, are shown as dot-dashed lines [42]. A clear and systematic mass-dependence of v_2 is seen in the data. It is a strong indicator that a common transverse velocity field underlies the observations. This mass-dependence, as well as the absolute magnitude of v_2, is reproduced reasonably well (at the $\sim$ 30% level) by the hydrodynamics calculations with QGP equation of state [41]. The inferred early thermalization suggests that at the early stage, collisions are dominated by strongly interacting matter, with short constituent mean free paths essentially a perfect liquid with small viscosity. Extracting the viscosity of the produced QCD matter in the heavy-ion collisions from the elliptic flow measurements is one of the main goals of this thesis. The comparison of the charged hadron v_2 from a 2+1D viscous hydrodynamic simulation to the corresponding

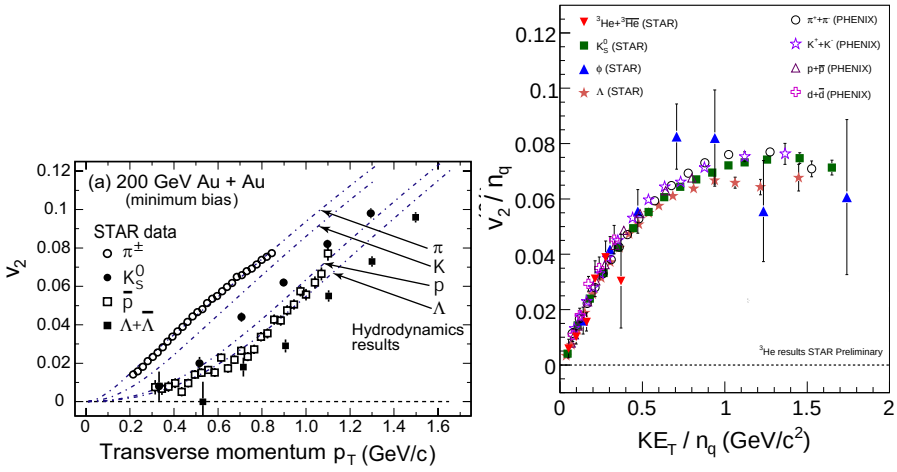

Figure 1.9: Left panel: STAR experimental results for the transverse momentum dependence of the elliptic flow parameter in 200 GeV minimum bias Au-Au collisions for $\pi^{\pm}$, K^0_s, $\bar{p}$ and $\Lambda + \bar{\Lambda}$ [41]. Hydrodynamic calculations [42] are shown as the dot-dashed lines. Right panel: Compilation of the number of constituent quark scaled v_2 as a function of the scaled transverse kinetic energy [32].

experimental measurements at RHIC and LHC are discussed in chapter 5 of this thesis.

The right panel of figure 1.9 shows the elliptic flow v_2 of several identified particles versus the transverse kinetic energy (m_T - m_0), both divided by the number of constituent quarks (n_q). Where m_0 is the rest mass of particle and $m_{\rm T}$ is the transverse mass $\sqrt{p_{\rm T}^2 + m_0^2}$. The v_2 for all identified hadrons as well as light nuclei below m_T - $m_0 <$ 1 GeV falls on a universal curve [32]. This scaling behavior is believed to provide the evidence for formation of partonic matter during the Au-Au collision process at 200 GeV. It is very hard to explain this observed pattern in a scenario where only hadronic matter exists throughout the interaction, whereas the hypothesis of coalescence of quarks from de-confined QGP phase offers a ready explanation [43].

1.3.3 J/ψ suppression

J/Ψ is a bound state of $c\bar{c}$ and it is produced in the initial stage of the nucleus nucleus collision. Suppression of J/Ψ production in high energy heavy ion collisions relative to p-p collisions is considered as a signature of QGP. This was pointed out almost 30 years ago by Matsui and Satz [44].

To understand the phenomenon of J/Ψ suppression in the QGP, we consider the following points [45]: (a) The string tension k in the inter quark potential $v(r) = -\frac{q}{4\pi r} + kr$ tends to 0 in the high temperature QGP phase. Where q is the color charge of the quarks and r is the inter quark distance. (b) Debye screening of color charges (q) between c and $\bar{c}$ leads to the rearrangement of the parton densities around c and $\bar{c}$. The potential gets modified and has the following form,

$$v(r) = -\frac{q}{4\pi}\frac{e^{-r/\lambda_{\mathrm{D}}}}{r}. \tag{1.4}$$

Where the Debye screening length (λ_{D}) according to perturbative QCD calculation is inversely proportional to the plasma temperature and a function of g ($=\sqrt{4\pi\alpha_{\mathrm{s}}}$), $\lambda_{\mathrm{D}} = \frac{1}{\sqrt{\left(\frac{N_{\mathrm{c}}}{3}+\frac{N_{\mathrm{f}}}{6}\right)g^2T}}$. N_{c} and N_{f} are the number of colors and flavors respectively. (c) The value of λ_{D} becomes small at high temperature and consequently the range of attractive potential (equation 1.4) become small. At high enough temperatures , it may be impossible for $c\bar{c}$ pair to form a bound state. That particular temperature when the dissociation of $c\bar{c}$ pair happens is called critical dissociation temperature T_{cd}. Using the charm quark mass m_{c}=1.84 GeV, a lowest order perturbative QCD calculation gives $T_{\mathrm{cd}} = 0.291\sqrt{\alpha_{\mathrm{eff}}}$, where α_{eff} is the effective strong coupling constant. By using the

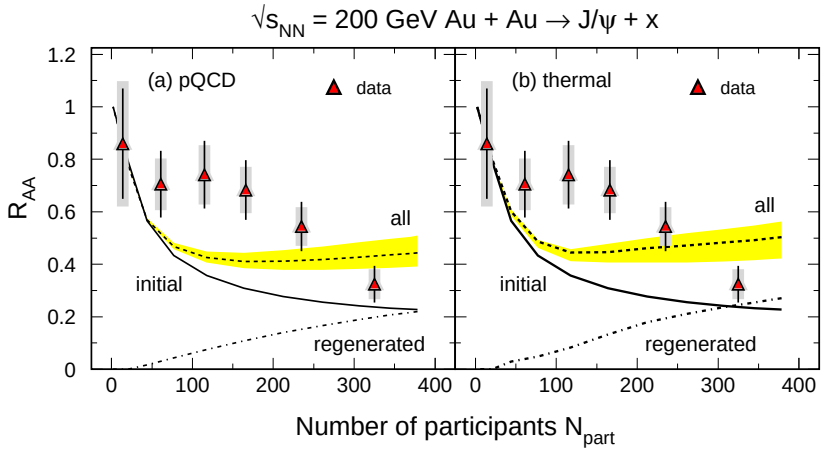

Figure 1.10: The J/Ψ nuclear modification factor $R_{\rm AA}$ as a function of number of participant $N_{\rm part}$ [47]. The red triangles are experimentally measured data for $\sqrt{s_{\rm NN}}$=200 GeV collision at mid rapidity by the PHENIX collaboration [46]. See text for details.

approximate value of $\alpha_{\rm eff}$ in the QGP phase, the above expression gives $T_{\rm cd}$ values 100-200 MeV[45]. In the heavy ion collision at both RHIC and LHC the initial temperature of the produced QGP is well above this predicted value of $T_{\rm cd}$.

The separated c and $\bar{c}$ quark in the QGP phase subsequently hadronizes by combining with other light quark present in the system. Thus in a nucleus-nucleus collision where QGP is formed, the final yield of J/Ψ particle will be suppressed as compared to p-p collision where QGP is not formed. However, the produced J/Ψ in nucleus nucleus collision may also interact with other hadrons produced in the collision and this may lead to the break up of the J/Ψ particles and hence results in suppression of J/Ψ yields.

The red triangles in figure 1.10 shows the experimental measurement of nuclear modification factor $R_{\rm AA}$ as a function of $N_{\rm part}$ for $\sqrt{s_{\rm NN}}$=200 GeV collision at midra-

pidity [46]. Where the nuclear modification factor $R_{\rm AA}$ is a measure of J/Ψ suppression and is defined as $R_{\rm AA} = \frac{N_{J/\Psi}(Au-Au)}{N_{\rm coll}\times N_{J/\Psi}(p-p)}$. Where $N_{\rm coll}$ is the number of binary collision. A value of $R_{\rm AA}$ <1 indicates J/Ψ suppression in heavy ion collision relative to p-p collision. From figure 1.10 we see that J/Ψ is suppressed for nucleus-nucleus collisions at $\sqrt{s_{\rm NN}}$=200 GeV at mid rapidity. The suppression is more for central compared to peripheral collision. The solid lines in the figure corresponds to $R_{\rm AA}$ values considering only the suppression in QGP of initially produced J/Ψ through pQCD (left panel) and thermal (right panel) processes [47]. The dashed-dotted curves corresponds to contribution due to the effect of regeneration of J/Ψ in the hot QGP phase, where the dissociated c and $\overline{c}$ come close to one another in the process of hadronization and form J/Ψ. The sum of the two contribution is shown as dashed lines in the figure 1.10.

1.3.4 Electromagnetic probes

Photons and dileptons produced in nuclear collisions are combinedly known as electromagnetic probes. They are produced throughout the whole space-time evolution of the fireball from early stage of pre-equilibrium upto the freezeout. After production, photons and dileptons interacts with the medium dominantly via electromagnetic interactions (electromagnetic coupling constant $\alpha_{\rm e}$ is small compared to strong coupling constant $\alpha_{\rm s}$). The mean free path of the photons and dileptons are large compared to the system size, hence, they suffer almost no collision inside the medium before reaching the detectors. We will consider here only photon production as a possible signature of QGP formation. Some nice reviews on photon and dileptons production and their use

as a signal of QGP formation in high energy heavy ion collision can be found in refs. [48, 49, 50, 51, 52, 53].

In the QGP phase the photon production rate and the photon momentum distribution depend on the momentum distribution of the quarks, antiquarks and gluons from which it is produced. Therefore, photon produced in quark gluon plasma phase carry information on the thermodynamical state of the medium at the moment of their production. The dominating processes by which photon is produced in the QGP phase are,

- Annihilation : In this process a quark interact with an antiquark and produce a photon and a gluon. The corresponding reaction is $q + \overline{q} \rightarrow \gamma + g$. The other possibility $q + \overline{q} \rightarrow \gamma + \gamma$ is suppressed compared to the previous one by a factor of $\alpha_{\mathrm{e}}/\alpha_{\mathrm{s}}$ and is generally not considered in calculation.

- Compton process : In Compton process, a gluon interact with a quark (anti-quark) and produce a photon and quark (anti-quark). Corresponding reactions are $q + g \rightarrow \gamma + q$ and $\overline{q} + g \rightarrow \gamma + \overline{q}$.

- Bremsstrahlung process : $\mathrm{q} + \mathrm{g} \rightarrow \mathrm{g} + q^* \rightarrow \mathrm{g} + \mathrm{q} + \gamma$.

- Fragmentation process : $\mathrm{q} + \mathrm{g} \rightarrow \mathrm{q} + g^* \rightarrow \mathrm{q} + \gamma + \mathrm{X}$.

Measuring these direct photons will help us to detect the formation of QGP in heavy-ion collisions and understand its thermodynamic properties.

However, there exists other sources of photons in heavy-ion collisions. Photons are also produced in the hadronic phase. For example, $\pi^+ + \pi^- \rightarrow \gamma + \rho^0$ and $\pi^\pm + \rho^0 \rightarrow \gamma + \pi^\pm$ etc. There is no direct experimental way to separate the photon from the above mentioned sources from those coming from QGP. Besides the emission of photons from the QGP and hadronic phase, photons can also be produced at the time of collision between two nucleus. The dominating production mechanism of photon in this case is same as QGP phase (i,e. annihilation and Compton processes) but involving quarks and gluons inside the incoming nucleons. The difference between the photon production from the QGP phase and from the initial state of the collision is that in the QGP phase the quark, antiquark, and gluon from which photon is produced follows the corresponding thermal distribution, whereas for the other case quarks and gluons are distributed inside the colliding nucleus according to their structure function. Experimentally this contribution of photons in heavy-ion collisions is estimated by measuring the direct photon distribution in p-p collisions and scaling the yields with the number of binary collisions. Finally photons are produced copiously from the decay of hadrons such as π^0 and η which are produced in heavy ion collisions through soft QCD processes. These contributions can be removed experimentally through the invariant mass reconstruction technique.

Figure 1.11 shows the invariant cross section (p-p) and invariant yield (Au-Au) of direct photons as a function of p_{T} at mid rapidity for $\sqrt{s_{\mathrm{NN}}} = 200$ GeV collision [54]. The three curves on the p-p data represent NLO pQCD calculations. The dashed curves show a modified power-law fit to the p-p data, scaled by Glauber nuclear overlap function (T_{AA}). Excess number of direct photon is observed in Au-Au collision compared to p-p collision in the p_{T} range 1-3 GeV. The solid black curves are exponential plus the T_{AA}

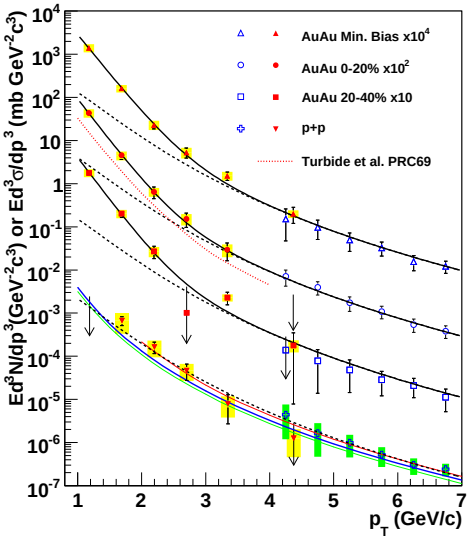

Figure 1.11: Invariant cross section (p-p) and invariant yield (Au-Au) of direct photons as a function of p_{T} at mid rapidity for $\sqrt{s_{\mathrm{NN}}} = 200$ GeV collision measured by the PHENIX collaboration at RHIC [54]. See the text for details.

scaled p-p fit. This indicates that the excess direct photon distribution is exponential and hence thermal in nature. The inverse slope parameter for the exponential function is 221 MeV for 0-20% centrality collision. The red dotted curve near the 0-20% centrality data is a hydrodynamical model based theory calculation with initial temperature 370 MeV [55]. Both these temperature values are larger than the critical temperature (∼174 MeV)[10] predicted by lQCD calculation for quark-hadron phase transition.

1.3.5 Strangeness enhancement

The phenomenon of strangeness enhancement as a signature of QGP formation in high energy heavy ion collision was reported more than 30 years ago [56, 57]. In a nucleus

nucleus collision, no valence strange quarks are present in the initial colliding nucleons. However, $s\overline{s}$ pair can be created in the subsequent QGP or hadronic phase formed in heavy ion collision. In the QGP phase $g + g \rightarrow s + \overline{s}$ is the dominating process for strangeness production [59]. These interactions could occur very rapidly and the s-quark abundance would equilibrate in the plasma. In a hot hadronic system, strange mesons can be produced through the following reactions, $\pi + \pi \rightarrow K + \overline{K}, N + N \rightarrow N + \Lambda + K$ etc. The strangeness enhancement in QGP with respect to a non-QGP system (hadronic gas) at the same temperature can be understood in the following simplified calculation. The ratio of number densities of strange quark to non strange quark (u and d quarks) can be calculated theoretically for a hadron gas and for QGP in thermal and chemical equilibrium. Let us first consider the strangeness content of a hadronic gas in thermal and chemical equilibrium. Considering only valence quark content of strange meson $K^{\pm}, K^0, \overline{K^0}$ and non-strange mesons $\pi^{\pm}, \pi^0$ one can arrive at the following relationship [45]

$$\frac{s + \overline{s}}{u + \overline{u} + d + \overline{d}} = \frac{K^+/\pi^+}{1.5 + K^+/\pi^+}. \tag{1.5}$$

The number density of a species with mass $m_{\rm i}$ at temperature T in a hadronic gas can be expressed as

$$n_{\rm i} = \frac{T m_{\rm i}^2}{2\pi^2} \sum_{k=1}^{\infty} \frac{1}{k} K_2 \left(\frac{k m_{\rm i}}{T} \right), \tag{1.6}$$

where K_2 is the modified Bessel function of order 2. Using this expression we can evaluate the ratio of number of positive Kaons (n_{K^+}) to that of positive Pions (n_{π^+}) [45] at temperature 200 MeV, which is $\frac{n_{K+}}{n_{\pi^+}} \approx 0.38$. Using this value of K^+/π^+ ratio into equation 1.5 we have the ratio of strange quark density to non-strange quark density in hadron gas at temperature 200 MeV as 0.20.

Similarly, the number density of strange and non strange quarks in QGP phase can be calculated by considering a QGP in thermal and chemical equilibrium state. The number density of quarks for zero chemical potential and temperature T is obtained by the following expression

$$n_{\mathrm{q}} = \frac{N_{\mathrm{c}} N_{\mathrm{s}}}{(2\pi)^3} \int_0^\infty \frac{4\pi p^2 dp}{1 + e^{\sqrt{p^2+m_{\mathrm{q}}^2}/T}}, \tag{1.7}$$

where N_{c}, N_{s} are the number of colors and number of spins of quarks respectively and m_{q} is the corresponding quark mass. Now we can calculate the same ratio $\frac{s+\overline{s}}{u+\overline{u}+d+\overline{d}}$ in QGP phase by using the equation 1.7. For a net baryon free QGP at temperature 200 MeV the ratio $\frac{s+\overline{s}}{u+\overline{u}+d+\overline{d}}$ is 0.42. This above calculation shows that the number of strange quark content in QGP is almost 2 times larger (strangeness enhancement) than the corresponding number of strange quark in hadronic gas at the same temperature. The higher number of s and $\overline{s}$ quarks in the QGP phase will finally shows up as an enhancement of strange hadrons (ϕ, K, Λ etc.) production compared to the case where the QGP is not formed like in p-p collisions. Figure 1.12 shows the enhancement of strange hadron production at RHIC for Au-Au and Cu-Cu collisions [62]. Upper panel shows the ratio of strange hadron production normalized to N_{part} in nucleus-nucleus collisions relative to corresponding results from p-p collisions at $\sqrt{s_{\mathrm{NN}}}$=200 GeV. The results are plotted as a function of N_{part}. All the strange hadrons $K^-, \phi, \overline{\Lambda}, \Xi$ and $\overline{\Xi}$ shows an enhancement. The observed enhancement increases with centrality and reaches a maximum for central collisions. The bottom panel of figure 1.12 shows the enhancement of ϕ meson for Au-Au and Cu-Cu collisions at $\sqrt{s_{\mathrm{NN}}}$=62.4 and 200 GeV. The observation of ϕ meson enhancement has helped us to solve the issue of canonical suppression, which challenged the idea of strangeness enhancement [60, 61]. According to the idea of canonical suppression, (a) the strangeness enhancement in

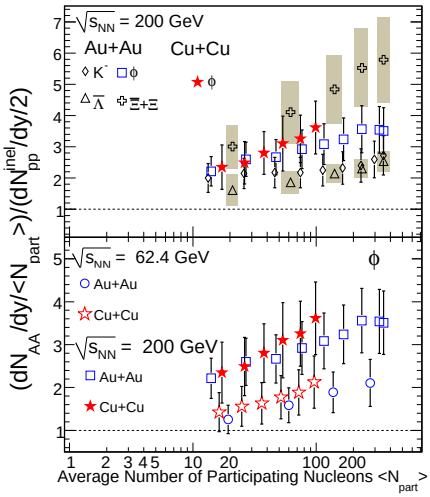

Figure 1.12: Upper panel: The ratio of the yields of $K^-, \phi, \overline{\Lambda}, \Xi$ and $\overline{\Xi}$ normalized to $\langle N_{\rm part} \rangle$ in nucleus-nucleus collisions to the corresponding yields in inelastic p-p collisions as a function of $\langle N_{\rm part} \rangle$ at 200 GeV [62]. Lower panel: Same as above but for ϕ mesons in Cu-Cu and Au-Au collisions at 200 and 62.4 GeV. The p-p collision data at 200 GeV are from the STAR experiment and at 62.4 GeV from the ISR [63].

nucleus-nucleus collisions, relative to p-p collisions, should increase with the valence strange quark content of the hadrons and (b) the enhancement is predicted to decrease with increasing beam energy. From figure 1.12 we see that both this points are in disagreement with the experimental measurement of ϕ meson suppression. All these observations is a clear indication for the formation of a dense partonic medium being responsible for the strangeness enhancement in Au-Au collisions at $\sqrt{s_{\rm NN}}$=200 GeV.

1.4 Transport properties

In the previous section we have seen that a strongly coupled state of quarks and gluons or QGP is formed in the high energy heavy ion collisions at RHIC. This provides us the unique opportunity to study the transport coefficients of this fundamental form of matter. For a system slightly away from equilibrium, according to the linear theory of non-equilibrium thermodynamics, the thermodynamic fluxes are proportional to the thermodynamic forces. The proportionality constants are known as the transport coefficients. The table 1.2 shows the thermodynamic fluxes and thermodynamic forces with corresponding transport coefficients.

Table 1.2: Thermodynamic flux, thermodynamic force, transport coefficient and their relationship.

Flux	Force (gradient of)	Transport coefficient	Equation
Momentum π_{ij}	Velocity v_i	Viscosity η, ζ	$\pi_{ij} = -\eta \left(\frac{\partial v_i}{\partial x_j}\right)$
Heat h_i	Temperature T	Heat conductivity k	$h_i = -k \left(\frac{\partial T}{\partial x_i}\right)$
Diffusion flow Φ_i	Number density n	Diffusion constant D	$\Phi_i = -D \left(\frac{\partial n}{\partial x_i}\right)$

Below we will only discuss shear viscosity, bulk viscosity, and heat conductivity.

1.4.1 Shear viscosity

The shear viscosity arises in a fluid when a velocity gradient is present. The shear viscosity coefficient η is a measure of how a fluid will flow under an applied force. The

inverse of η is called the fluidity. As we have seen in the table 1.2, the shear viscous coefficient η is the proportionality constant between momentum flux and the velocity gradient (force). The most general definition of viscous stress can be written as

$$\pi_{\mathrm{ij}} = \eta \left(\frac{\partial v_{\mathrm{i}}}{\partial x_{\mathrm{j}}} + \frac{\partial v_{\mathrm{j}}}{\partial x_{\mathrm{i}}} - \frac{2}{3}\delta_{\mathrm{ij}} \frac{\partial v_{\mathrm{k}}}{\partial x_{\mathrm{k}}} \right) + \zeta \delta_{\mathrm{ij}} \frac{\partial v_{\mathrm{k}}}{\partial x_{\mathrm{k}}}, \tag{1.8}$$

where ζ is the coefficient of bulk viscosity and is discussed in the next subsection. According to the above definition, there will be no shear viscous force for a fluid in uniform rotation for which the components of the gradient of velocity is related by the following condition $\frac{\partial v_{\mathrm{i}}}{\partial x_{\mathrm{j}}} = -\frac{\partial v_{\mathrm{j}}}{\partial x_{\mathrm{i}}}$.

The relativistic generalization of the shear part of the equation 1.8 is

$$\pi^{\mu\nu} = \eta \left[\Delta^{\mu}_{\alpha}\Delta^{\nu}_{\beta} + \Delta^{\mu}_{\beta}\Delta^{\nu}_{\alpha} - \frac{2}{3}\Delta^{\mu\nu}\Delta_{\alpha\beta} \right] \partial^{\alpha} u^{\beta}, \tag{1.9}$$

where $\Delta^{\mu\nu} = g^{\mu\nu} - u^{\mu}u^{\nu}$ is the projection operator, $g^{\mu\nu}$ is the metric tensor, and u^{μ} is the fluid four velocity. Equations 1.8 and 1.9 are the phenomenological definition of shear and bulk viscosity. The value of the shear, bulk viscosity, and all other transport coefficients can be calculated from the underlying kinetic theory of fluids. The molecular theory of transport phenomena in dilute gases gives the following expression for η [64],

$$\eta = \frac{1}{3} n \langle p \rangle l_{\mathrm{mfp}}, \tag{1.10}$$

where n is the density, $\langle p \rangle$ is the average momentum of the molecules, and l_{mfp} is the mean free path. The mean free path can be written as $l_{\mathrm{mfp}} = \frac{1}{n\sigma}$, where σ is the scattering cross section. Then we have $\eta = \frac{\langle p \rangle}{3\sigma}$. The mean momentum of molecules varies as $\sqrt{T}$ and consequently η for a system of dilute gas rises with increasing temperature.

The solution of Boltzmann kinetic equation in collision time approximation gives the following expression for η [65]

$$\eta = -\frac{\tau}{15}\int d\Gamma \frac{p^4}{\epsilon_{\rm p}^2}\frac{\partial f_0}{\partial \epsilon_{\rm p}} \tag{1.11}$$

where f_0 is the distribution function, $d\Gamma = g\frac{d^3p}{(2\pi)^3}$, g is the degeneracy, $\epsilon_{\rm p}$ is the energy of the particles considered.

The momentum transport in liquid is due to the motion of vacancies and has a different temperature dependence of η compared to gas [66]. In the above calculation the following assumptions are made (i) only two particle interaction are considered, (ii) distribution function vary slowly in the space time, and (iii) molecular chaos.

The shear viscosity for an strongly interacting system can be calculated by using Kubo formula [67] as given below

$$\eta = \lim_{\omega\to 0}\frac{1}{2\omega\hbar}\int dt d^3x e^{i\omega t}\left\langle [T_{\mu\nu}(t,x),\, T_{\mu\nu}(0,\mathbf{0})]\right\rangle . \tag{1.12}$$

Here $T_{\mu\nu}$ is the component of the stress-energy tensor, ω is the frequency.

Theoretical calculations based on quantum mechanics and string theory gives a lower bound $\frac{\hbar}{2\pi k_B}$ and $\frac{\hbar}{4\pi k_B}$ on η/s respectively [68]. Where $\hbar$ and k_B are Planck's constant divided by 2π and Boltzmann constant respectively. The details will be discussed in chapter-2.

In order to compare the value of η of various fluid of different mass density (ρ), it is desirable to compare the kinematic viscosity η/ρ of the fluids. For relativistic system

the corresponding quantity is η/s [66], where s is the entropy density of the fluid.

1.4.2 Bulk viscosity

In equation 1.8, we encountered the second viscosity coefficient ζ, which is also known as bulk viscosity or volume viscosity. First thing to be noted is that bulk viscosity arises for a non zero value of $\vec{\nabla}.\vec{v}$ which corresponds to a change in the fluid volume (density). If the process of compression or expansion is fast enough, the fluid ceases to be in thermodynamic equilibrium and internal processes are set up to restore the equilibrium. In the process of restoration of equilibrium, energy is dissipated as heat.

Like shear viscosity, the bulk viscosity coefficient ζ for a gas can be calculated from solution of Boltzmann kinetic equation in collision time approximation and has the following form [65]

$$\zeta = -\tau \int d\Gamma \frac{\partial f_0}{\partial \epsilon_{\rm p}} \left\{ \left(\frac{w}{c_{\rm v} T} - \frac{1}{3} \right) \epsilon_{\rm p} + \frac{m^2}{3\epsilon_{\rm p}} \right\}^2 . \tag{1.13}$$

Here $c_{\rm v}$ is the specific heat, $w = (\epsilon + p)$, ϵ is energy density, f_0 is the distribution function, $d\Gamma = g\frac{d^3p}{(2\pi)^3}$, g is the degeneracy, and $\epsilon_{\rm p}$ is the energy of the particles considered.

The bulk viscosity for an strongly interacting system can be calculated by using Kubo formula [67] given below

$$\zeta = \lim_{\omega \to 0} \frac{1}{6\omega\hbar} \int dt d^3x e^{i\omega t} \left\langle [T_{\mu\mu}(t,x),\, T_{\mu\mu}(0,\mathbf{0})] \right\rangle , . \tag{1.14}$$

Here $T_{\mu\mu}$ is the diagonal component of the stress-energy tensor, ω is the frequency. The bulk viscosity calculated in a perturbative QCD and string theoretical model based on anti de-Sitter space conformal field theory (AdS/CFT) are given by the following forms $\zeta = 15\eta\left(\frac{1}{3} - \frac{\partial p}{\partial \epsilon}\right)^2$ (PQCD) and $\zeta \propto \eta\left(\frac{1}{3} - \frac{\partial p}{\partial \epsilon}\right)$(AdS/CFT). For an ideal gas of massless particles, the speed of sound $c_s^2 = \frac{\partial p}{\partial \epsilon} = \frac{1}{3}$, consequently the bulk viscosity vanishes. It can be shown that a gas of point particles will have zero bulk viscosity in the non-relativistic limit [69]. However, a non-zero value of bulk viscosity may be obtained when the system undergoes a transition, or where the speed of sound is smaller than the Stefan-Boltzmann value $(1/\sqrt{3})$.

The shear and bulk viscosity of the strongly interacting Quark Gluon Plasma can be obtained from the first principle lQCD calculation [70, 71]. However, the present lattice calculations of transport coefficient of QCD matter has large uncertainty. Alternatively both the shear and bulk viscosity of the QGP can be estimated by comparing experimental data with the theoretical model simulations. With η and ζ as input in this thesis work such an approach has been used and discussed in chapter-5.

1.4.3 Heat conductivity

In the Navier-Stokes approximation the baryon flux can be decomposed into an ideal (nu^α) and dissipative component (ν^α) as $n^\alpha = nu^\alpha + \nu^\alpha$ [72], where u^α is the fluid four velocity. The form of the dissipative term ν^α depends on the definition of what constitutes the local rest frame of the fluid. In the Landau-Lifshitz frame (where energy

three flux T^{0i} vanishes) for first order theory with the constraint of second law of thermodynamics, the dissipative correction to the baryon number current takes the following form

$$\nu^{\alpha} = k \left[\frac{nT^2}{\epsilon + P} \right] \nabla^{\alpha} \left[\frac{\mu}{T} \right]. \tag{1.15}$$

Where k is the heat conductivity, μ is the chemical potential, and T is the temperature. For a symmetric matter (where number of baryons and anti-baryons are same) as is expected to form at the top RHIC and LHC energies, the baryon chemical potential is very small or almost zero. Hence $\nabla^{\alpha} \left[\frac{\mu}{T} \right]$ vanishes and there is no heat conduction. In view of the above argument we will neglect the dissipative contribution to the entropy generation due to the heat conductivity in our simulation of relativistic viscous hydrodynamics.

1.5 Organization of the thesis

The space-time evolution of the QCD matter can be simulated by using either relativistic hydrodynamics or relativistic transport models. QGP is a transient state of matter and it is believed that the perfect local thermal equilibrium is never achieved, rather QGP is a strongly interacting plasma with very low value of shear viscosity. This indicates that the space-time evolution of QGP should be described in a viscous hydrodynamics framework. By using viscous hydrodynamics we should be able to estimate (phenomenologically) the transport coefficients e.g., shear, bulk viscosity, and heat conductivity of the QGP. By comparing the experimental observables measured at RHIC and LHC to numerical simulations of the relativistic viscous hydrodynamics

in 2+1 dimension, we have estimated the shear viscosity to entropy density ratio of the QCD matter and studied the effect of bulk viscosity on the experimental observables. Similar works in this direction can be found in [73, 74, 75, 76, 77, 79, 80, 81, 82].

In the second chapter, we will discuss the formalism of Israel-Stewart second order theory of causal viscous hydrodynamics and the implementation of it to the numerical code of 2+1D viscous hydrodynamics AZHYDRO-KOLKATA [83, 84]. Third chapter deals with the numerical results of shear viscous evolution. Numerical solution of bulk viscous evolution and corresponding results will be discussed in the fourth chapter. In the fifth chapter, we compare the viscous hydrodynamics simulation results with experimental observables (mostly $p_{\rm T}$ spectra, differential and integrated elliptic flow of charged hadrons) measured at Relativistic Heavy Ion Collider and Large Hadron Collider experiments. We also compare our estimates of η/s to corresponding results from other groups. We summarize the work carried out in this thesis and present a brief outlook in the final chapter.

Chapter 2

Relativistic hydrodynamics

In this chapter we discuss the relativistic hydrodynamics for both ideal and viscous fluids. It has already been discussed in chapter-1 that a major portion of the space-time evolution of the QCD matter produced in high energy heavy ion collisions can be described in the frame work of relativistic hydrodynamics. One of the first application of relativistic hydrodynamics in high energy nuclear collisions is due to Landau [85]. According to Landau the motivations behind the applicability of hydrodynamics are the following:

(i) Due to high velocity, the accelerating nucleus becomes highly Lorentz contracted. After collision a large amount of energy is deposited in a small volume by the inelastic collisions between the nucleons and large number of particles are formed. The mean free path in the resulting system is small compared to the whole volume and statistical equilibrium sets up.

(ii) In the next stage, the expansion of the system is described by hydrodynamic equa-

tions. During the process of expansion, the mean free path remains small in comparison to system size, and this justify the use of hydrodynamics. Since the velocities in the system is comparable to the speed of light, we must use relativistic hydrodynamics.
(iii) As the system expands, the interaction becomes weaker and mean free paths becomes longer. The number of particles appears as a physical characteristic when the interaction becomes sufficiently weak. When the mean free path becomes comparable to the linear dimension of the system, the latter breaks up into particles. This was called as "'break-up"' stage. The break-up occurs when the temperature of the system becomes comparable to the pion mass.

At very high energy collisions J.D. Bjorken [86] proposed a modification to the existing Landau's hydrodynamic model. According to Bjorken, at very high energy collisions the colliding nucleus or nucleons becomes transparent. After collision the colliding nucleus are receding from each other with almost the speed of light. A central plateau region is formed in the particle production with rapidity variable. The fluid expansion near the collision axis occurs along the longitudinal direction and is homogeneous. The entropy per unit rapidity is conserved, as a consequence of the boost symmetry. Particle productions per unit rapidity only depends on the initial energy density (entropy density) and not on the details of the hydrodynamic evolution.

Even today these main ideas due to Landau and Bjorken remains almost unchanged. We now have stronger evidence in support of hydrodynamics to be applicable in describing the evolution of nuclear matter produced in high energy heavy ion collisions. The two main experimental evidences in this direction are the mass dependence of the

slope of the p_T spectra for identified hadrons and the mass ordering of elliptic flow v_2 in nucleus-nucleus collisions (see figure 1.9). These phenomena are not observed for the proton-proton collision at the same centre of mass energy [41].

2.1 Ideal hydrodynamics

In classical hydrodynamics a perfect or ideal fluid is defined to be a continuum system which obey Pascal's law (any exerted pressure will be transmitted isotropically throughout the fluid) and is incapable of supporting any shear force applied to it. By using the above criterion one can construct the stress-energy tensor $T^{\mu\nu}$ for a perfect fluid in the framework of special relativity. Let us consider an fluid element in the local rest frame, for which the fluid four velocity is $u^\mu = (1, \vec{0})$. In absence of any heat conduction, the energy flux of the fluid T^{0i} will be zero and T^{00} will be the energy density ϵ. On the other hand, i-th component of the force exerted on surface element dS_j is $T^{ij}dS_j$. According to the Pascal's law this force is isotropic and normal to the surface on which it acts. Thus we can write $T^{ij} = P\delta^{ij}$, where P is the pressure measured by an observer at rest with respect to the fluid. Therefore, for an element of fluid at local rest frame, the stress-energy tensor takes the following form

$$T^{\mu\nu} = \begin{pmatrix} \epsilon & 0 & 0 & 0 \\ 0 & P & 0 & 0 \\ 0 & 0 & P & 0 \\ 0 & 0 & 0 & P \end{pmatrix}. \tag{2.1}$$

Where ϵ is the energy density of the fluid. We can find an expression for a moving fluid element having four velocity $u^\mu = \gamma(1, \vec{v})$ by a Lorentz transformation of $T^{\mu\nu}$. The final form of the energy-momentum tensor obtained in this way is expressed as $T^{\mu\nu} = (\epsilon + P)u^\mu u^\nu - Pg^{\mu\nu}$. Here $g^{\mu\nu}$ is the metric tensor. Both the ϵ and P appearing in this equation are measured by an observer moving with the fluid and in general ϵ and P are function of the position four vector x^μ. The space-time evolution of the ideal fluid is governed by the equations of the conservation of energy and momentum

$$\partial_\mu T^{\mu\nu} = 0. \tag{2.2}$$

Apart from the energy-momentum conservation, a fluid may contain several conserved charges, such as total electric charge, net baryon number etc. The conserved charges obey the following continuity equation

$$\partial_\mu N_j^\mu = 0, j = 1, k. \tag{2.3}$$

Where $N_j^\mu = \gamma(n, \vec{j})$ is the particle current four vector. The zeroth component N^0 is the number density n, measured by an observer moving with the fluid element at a given space-time point. The other three components $N^i (i = 1, 2, 3)$ are the corresponding current $\vec{j}$. The subscript j denotes different conserved charges. One of the conserved charge for heavy-ion collisions is the net baryon number (the number of baryon minus the number of anti-baryon). Thus for an ideal fluid with local thermal equilibrium $T^{\mu\nu}$ and N^μ takes the following form

$$T^{\mu\nu} = [\epsilon(x) + P(x)]\, u^\mu u^\nu - P(x) g^{\mu\nu} \tag{2.4}$$

$$N^\mu = n u^\mu. \tag{2.5}$$

There are five equations, four conservation equation for energy-momentum and one for particle number, but the number of unknown is six $\epsilon(x), P(x), n(x)$ and three compo-

nents of u^μ (three because $u_\mu u^\mu = 1$). In order to close the equations an Equation of State (EoS) $P = f(\epsilon,n)$ is necessary. We will discuss more about EoS in a later section. Using the thermodynamic relationship, $Tds = Pd\left(\frac{1}{n}\right) + d\left(\frac{\epsilon}{n}\right)$, where $1/n$ denotes the volume per particle and s is the entropy per unit volume, and by taking product of u^μ with equation 2.3, the specific entropy s is found to be constant in time. Mathematically this is expressed as

$$\partial_\mu S^\mu = 0 \tag{2.6}$$

$$S^\mu = su^\mu. \tag{2.7}$$

Where S^μ is the entropy four current. The entropy density for an ideal fluid is obtained from the thermodynamic relation

$$Ts = \epsilon + P - \mu N, \tag{2.8}$$

where μ is the chemical potential. Thus the fundamental equations which completely determine the evolution of a relativistic ideal fluid are the continuity equation and the energy momentum conservation equation along with an EoS.

To gain some physical insight from the conservation equation 2.2, we consider the projector operator $\Delta^{\mu\nu} = (g^{\mu\nu} - u^\mu u^\nu)$. The corresponding covariant operator is $\Delta_{\mu\nu} = (g_{\mu\nu} - u_\mu u_\nu)$. The $\Delta^{\mu\nu}$ is orthogonal to fluid four velocity u^μ which can be understood from the following property

$$\Delta^{\mu\nu} u_\mu = 0. \tag{2.9}$$

The parallel projection of equation 2.2 in the direction of fluid four velocity gives

$$u_\nu \partial_\mu T^{\mu\nu} = 0$$

$$\Rightarrow D\epsilon + (\epsilon + P)\,\partial_\mu u^\mu = 0, \tag{2.10}$$

where $D = u^\mu \partial_\mu$. The perpendicular projection of equation 2.2 to the u^μ gives

$$\begin{aligned} \Delta^\alpha_\nu \partial_\mu T^{\mu\nu} &= 0 \\ \Rightarrow (\epsilon + P)\, u^\mu \partial_\mu u^\alpha - \Delta^{\mu\alpha} \partial_\mu P &= 0 \\ \Rightarrow (\epsilon + P)\, Du^\alpha - \nabla^\alpha P &= 0, \end{aligned} \tag{2.11}$$

where $\nabla^\alpha = \Delta^{\mu\alpha}\partial_\mu$. In the non-relativistic limit D and ∇^α essentially reduces to time and space derivative and the energy density ϵ in a very good approximation reduces to mass density (ρ) and the following relations holds $\rho >>$P. With all these approximations equation 2.10 and 2.11 reduces to the following conservation of mass and Euler equations.

$$\frac{\partial \rho}{\partial t} + \vec{\nabla}.(\rho \vec{v}) = 0, \tag{2.12}$$

$$\frac{\partial \vec{v}}{\partial t} + \vec{v}.\vec{\nabla}\vec{v} = -\frac{1}{\rho}\vec{\nabla}P. \tag{2.13}$$

2.2 Viscous hydrodynamics

Non zero shear and bulk viscosity in Heavy Ion Collision :

The shear viscosity for a strongly interacting quantum fields can be obtained by using the Kubo formula [68]

$$\eta = \lim_{\omega \to 0} \frac{1}{2\omega\hbar} \int dt dx e^{i\omega t} \left\langle [T_{\mu\nu}(t,x),\, T_{\mu\nu}(0,\mathbf{0})] \right\rangle, \tag{2.14}$$

where $T_{\mu\nu}$ is the traceless part of the stress-energy tensor, ω is angular frequency, and $\hbar$ is Planck constant divided by 2π. The right hand side can be related to the absorption

cross section of low energy graviton by branes in string theory [68].

$$\sigma_{\rm abs}(\omega) = \frac{\kappa^2}{\omega} \int dt\, dx\; e^{i\omega t}\; \langle [T_{\mu\nu}(t,x),\, T_{\mu\nu}(0,\mathbf{0})] \rangle\,, \tag{2.15}$$

where $\kappa = \sqrt{8\pi G}$ appears due to the normalization of the graviton's action. Identifying the entropy density $s = a/4G$, where a is the area of the event horizon for the calculation as given in [68] leads to the following relationship

$$\frac{\eta}{s} = \frac{\hbar}{4\pi k_B}\,. \tag{2.16}$$

Where k_B is the Boltzmann constant. The quantum mechanical calculation based on uncertainty principle also predicts a lower bound on η/s. The shear viscosity of any fluid is $\eta \sim \epsilon\tau_{\rm mft}$, where ϵ is the energy density and $\tau_{\rm mft}$ is the typical mean free time of quasi particles. The entropy density is $s \sim k_B n$, where n is the number density of quasi particles. Therefore $\eta/s \sim \frac{\tau_{\rm mft}\epsilon}{k_B n}$. Here ϵ/n is the average energy per quasi particle. According to the uncertainty principle, the product of ϵ/n and $\tau_{\rm mft}$ is greater than or equal to $\hbar$. Therefore we obtain, from the uncertainty principle alone, that $\eta/s \geq \hbar/k_B$. In addition, the calculations from lQCD and perturbative QCD (pQCD) shows that η/s is non-zero for the temperature range achieved in high energy heavy-ion collisions [70, 71]. This is shown in the left panel of figure 2.1. The η/s in hadronic phase can be calculated using a hadron resonance gas model [88]. Right panel in figure 2.1 shows the η/s for a hadron resonance gas as function of temperature. The black dashed line is the result with excluded volume correction. The solid red line is the calculation with additional Hagedorn states.

The bulk viscosity for the QGP phase has been calculated in both lQCD as well as in pQCD [70, 71]. According to the pQCD calculation, bulk viscosity satisfy the

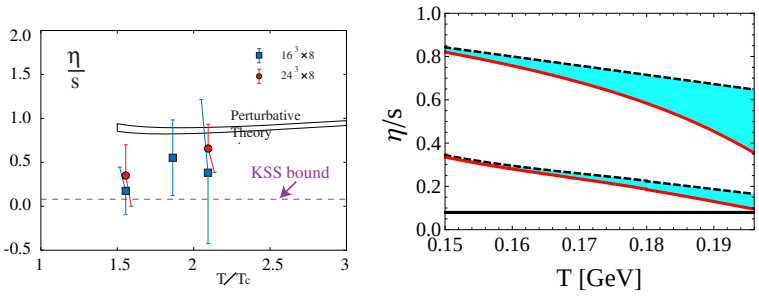

Figure 2.1: Left panel : η/s as a function of T/T_c from lattice QCD calculation for two different lattice size [71]. Also shown are the perturbative QCD calculation of η/s as well as the KSS bound [68]. Right panel : η/s as a function of T from hadron resonance gas model calculation [88]. See text for details.

following relation

$$\zeta \approx 15\eta \left(\frac{1}{3} - c_s^2\right)^2, \tag{2.17}$$

where η and c_s are the shear viscosity and the speed of sound of the medium respectively. The Anti de Sitter space Conformal Field Theoretical (AdS/CFT) calculations gives the following form [87]

$$\zeta \propto \eta \left(\frac{1}{3} - c_s^2\right). \tag{2.18}$$

The two formula differed in the dependence of ζ on $\frac{1}{3} - c_s^2$. Both of them suggest a non-zero value of ζ. As in the temperature range achieved in high energy heavy-ion collision $\eta/s \geq 1/4\pi$ and $c_s^2 < \frac{1}{3}$ from lQCD [10].

The left panel of figure 2.2 shows the lattice calculation of ζ/s by two different groups [70, 71]. In the hadronic phase ζ/s can be calculated in a hadron resonance gas (hrg) model. One such calculation by Noronha et al. [88] is shown in the right panel of figure 2.2. The dashed black line is the calculated ζ/s for hrg with the excluded volume correction due to the finite size of hadrons. For the calculation all hadrons with mass

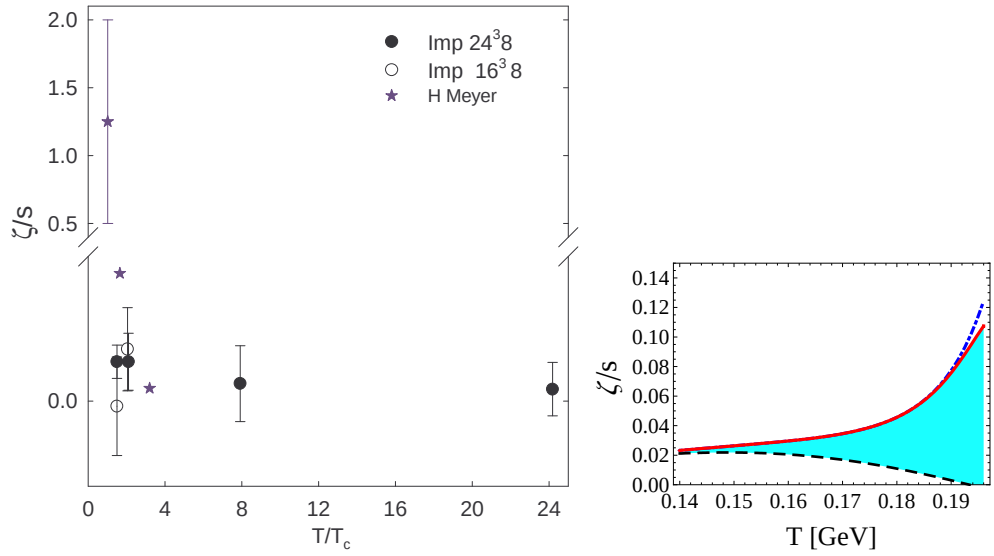

Figure 2.2: Left panel : ζ/s as a function of T/T_c from the lattice QCD calculation by Meyer (star) [70] and Nakamura et al. (filled circles) [71]. Right panel : ζ/s as a function of temperature in the hadronic phase from hadron resonance gas model calculation [88].

less than 2 GeV was considered. The red solid and blue dashed lines are calculations for hrg gas with the additional contributions from exponentially increasing Hagedorn mass states for two limiting values of Hagedorn mass $m_H = 20$ and 80 GeV respectively. Both η/s and ζ/s being nonzero in heavy ion collision emphasizes the need to include viscous effects in relativistic hydrodynamics. In the next sections we discuss the formalism for relativistic viscous hydrodynamics in detail.

2.2.1 First-Order theory for viscous hydrodynamics

The early formulation of relativistic viscous hydrodynamics can be found in the work by Eckart [89, 90] and Landau-Lifshitz [91]. These theories are known as first order theory

as the non equilibrium entropy four current S^μ contains terms which are of first order in the dissipative fluxes. The resulting equations for the dissipative fluxes are linearly proportional to the thermodynamic forces. The relativistic viscous hydrodynamics can be formulated either from kinetic theory or from a phenomenological macroscopic approach [92, 93, 94, 95]. We will discuss the phenomenological approach here. In a phenomenological macroscopic theory the non-equilibrium entropy four current can be written as

$$\begin{aligned} S^\mu &= S^\mu_{eq} + \delta S^\mu \\ &= \frac{P(\alpha,\beta)u^\mu - \mu N^\mu_{eq} + u_\nu T^{\nu\mu}_{eq}}{T} + Q^\mu\left(\delta N^\mu, \delta T^{\mu\nu}\right) \\ &= P(\alpha,\beta)\beta^\mu - \alpha N^\mu_{eq} + \beta_\nu T^{\mu\nu}_{eq} + Q^\mu\left(\delta N^\mu, \delta T^{\mu\nu}\right), \end{aligned} \tag{2.19}$$

where $\alpha = \frac{\mu}{T}, \beta = \frac{1}{T}$, and $\beta_\nu = \frac{u_\nu}{T}$. The term $Q^\mu\left(\delta N^\mu, \delta T^{\mu\nu}\right)$ contains second and higher order terms of dissipative flows δN^μ and $\delta T^{\mu\nu}$. Where δN^μ and $\delta T^{\mu\nu}$ are the dissipative corrections to the equlilibrium particle four current (N^μ_{eq}) and energy-momentum tensor $(T^{\mu\nu}_{eq})$ respectively. The non-equilibrium particle four current (N^μ) and energy-momentum tensor $(T^{\mu\nu})$ are given by,

$$N^\mu = \quad N^\mu_{eq} + \delta N^\mu = nu^\mu + V^\mu, \tag{2.20}$$

and

$$\begin{aligned} T^{\mu\nu} = \quad & T^{\mu\nu}_{eq} + \delta T^{\mu\nu} \\ = \quad & [\epsilon u^\mu u^\nu - P\Delta^{\mu\nu}] - \Pi\Delta^{\mu\nu} + \pi^{\mu\nu} \\ & + (W^\mu u^\nu + W^\nu u^\mu). \end{aligned} \tag{2.21}$$

Where $\delta N^\mu \equiv V^\mu$ is the charge diffusion current, and W^μ is the energy-momentum flow orthogonal to u^μ which be decomposed as $W^\mu = q^\mu + \frac{\epsilon+P}{n}V^\mu$, q^μ is the heat flow. The

first order theory of viscous relativistic hydrodynamics is obtained from the second law of thermodynamics $\partial_\mu S^\mu \geq 0$, by setting $Q^\mu = 0$ in the equation 2.19

$$\begin{aligned} \partial_\mu S^\mu &= \partial_\mu \left(P\beta^\mu\right) - \partial_\mu \left(\alpha N^\mu_{eq}\right) + \partial_\mu \left(\beta_\nu T^{\mu\nu}_{eq}\right) \\ &= \left(N^\mu - N^\mu_{eq}\right)\partial_\mu\alpha - \left(T^{\mu\nu} - T^{\mu\nu}_{eq}\right)\partial_\mu\beta_\nu. \end{aligned} \tag{2.22}$$

The last line was obtained by using the Gibbs-Duhem relationship, $\partial_\mu \left(P\beta^\mu\right) = N^\mu_{eq}\partial_\mu\alpha - T^{\mu\nu}_{eq}\partial_\mu\beta_\nu$. Using equations 2.20 and 2.21 into the equation 2.22, we have the following inequality,

$$\partial_\mu S^\mu = \frac{1}{T}\left(\Pi X - q^\mu X_\mu + \pi^{\mu\nu}X_{\mu\nu}\right) \geq 0. \tag{2.23}$$

Where $X \equiv -\theta = -\partial_\mu u^\mu$; $X_\mu \equiv \lambda\frac{nT^2}{\epsilon+p}\nabla^\mu\left(\frac{\mu}{T}\right)$ and $X_{\mu\nu} \equiv \nabla_{<\mu}u_{\nu>}$. The inequality in the equation 2.23 can be satisfied by assuming the following relationship between thermodynamic force to thermodynamic fluxes.

$$\begin{aligned} \Pi &= -\zeta\theta, \\ \pi^{\mu\nu} &= 2\eta\nabla^{<\mu}u^{\nu>}, \\ q^\mu &= -\lambda\frac{nT^2}{e+p}\nabla^\mu\left(\frac{\mu}{T}\right) \quad . \end{aligned} \tag{2.24}$$

The positive transport coefficients ζ, η, and λ are the bulk viscosity, shear viscosity, and heat conductivity respectively. $\theta = \partial_\mu u^\mu$ is the expansion scalar and $\nabla^{<\mu}u^{\nu>} = \frac{1}{2}(\nabla^\mu u^\nu + \nabla^\nu u^\mu) - \frac{1}{3}(\partial_\mu u^\mu)(g^{\mu\nu} - u^\mu u^\nu)$ is a symmetric traceless tensor. Using equation 2.24, the inequality in 2.23 takes the following form

$$\partial_\mu S^\mu = \frac{1}{T}\left(\Pi^2 - q^\mu q_\mu + \pi^{\mu\nu}\pi_{\mu\nu}\right) \geq 0. \tag{2.25}$$

All terms on the left side of the inequality are now positive definite (the negative sign before the q^μ makes the second term positive as q^μ is a space like vector perpendicular

to u^μ). The equations in 2.24 are known as Navier-Stokes equations and they are of parabolic in nature. It is the nature of the parabolic differential equation that it permits the undesirable effect of infinite speed of signal propagation. The relativistic Navier-Stokes theory is no exception. Consider a small perturbation in the fluid energy density and fluid velocity of a system which was initially at equilibrium and at rest [96, 97]

$$\epsilon = \epsilon_0 + \delta\epsilon(x,t), u^\mu = (1,\vec{0}) + \delta u^\mu(x,t). \tag{2.26}$$

The relativistic Navier-Stokes equation then specify the space-time evolution of the perturbed quantities, for a particular direction $\mu = y$ this is given by

$$\partial_t \delta u^y - \frac{\eta_0}{\epsilon_0 + p_0}\partial_x^2 \delta u^y = \mathcal{O}(\delta^2)\ . \tag{2.27}$$

This gives the following "dispersion-relation" of the diffusion equation

$$\omega = \frac{\eta_0}{\epsilon_0 + p_0}k^2. \tag{2.28}$$

The velocity of a particular mode with angular frequency ω can be obtained by taking the derivative of ω with respect to the wave number k

$$v_T(k) = \frac{d\omega}{dk} = 2\frac{\eta_0}{\epsilon_0 + p_0}k. \tag{2.29}$$

One finds v_T is linearly dependent on the wavenumber k, which implies that for a sufficiently large value of k, the speed of the diffusion will grow without bound and exceed the speed of light.

The widely used causal viscous hydrodynamics is due to Israel, Stewart, and Muller [92, 98]. There are other similar formalism of causal relativistic viscous hydrodynamics e.g, Ottinger and Gremla formalism [99]. These causal theories are developed with the

assumption that the entropy four current S^μ include terms quadratic in the dissipative fluxes and hence they are called second order theories of dissipative fluids. In the next sub-section we will discuss the Israel-Stewart second order theory from a phenomenological point of view.

2.2.2 Israel-Stewart theory of second order causal viscous hydrodynamics

Israel and Stewart constructed causal viscous hydrodynamics by incorporating second order terms in the entropy four current s^μ. This phenomenological construction of the second order terms incorporate five new transport coefficients in addition to the thermal conductivity and two coefficient of viscosity.

For the causal theory of second order viscous hydrodynamics the term Q^μ in equation 2.19 should be kept. Q^μ contain terms which are second order of dissipative fluxes.

$$Q^\mu = \frac{q^\mu}{T} + \frac{\beta_0}{2T} u^\mu \Pi^2 - \frac{\beta_1}{2T} u^\mu q_\mu q^\mu + \frac{\beta_2}{2T} u^\mu \pi_{\alpha\beta}\pi^{\alpha\beta} - \frac{\alpha_0 \Pi q^\mu}{T} + \frac{\alpha_1 \pi^{\mu\nu} q_\nu}{T}, \qquad (2.30)$$

where β_0, β_1, and β_2 are thermodynamic coefficients for bulk stress (Π), heat flow (q^μ), and shear viscous stress ($\pi^{\mu\nu}$) respectively, α_0, and α_1 are thermodynamic coefficients for coupling between heat flow to the viscous stresses. The divergence of the non-equilibrium entropy four current now takes the following form

$$\begin{aligned} \partial_\mu S^\mu &= \frac{1}{T}\left(\Pi X - q^\mu X_\mu + \pi^{\mu\nu} X_{\mu\nu}\right) + \partial_\mu Q^\mu \\ &= -\Pi\left[\theta + \beta_0 \dot{\Pi} + \frac{1}{2} T \partial_\mu \left(\frac{\beta_0}{T} u^\mu\right) \Pi - \alpha_0 \nabla_\mu q^\mu\right] \end{aligned}$$

$$-q^{\mu}\left[\nabla_{\mu}\ln T-\dot{u}_{\mu}-\beta_1\dot{q}_{\mu}-\frac{1}{2}T\partial_{\nu}\left(\frac{\beta_1}{T}u^{\nu}\right)q_{\mu}-\alpha_0\nabla_{\nu}\pi^{\nu}_{\mu}-\alpha_1\partial_{\mu}\Pi\right]$$
$$+\pi^{\mu\nu}\left[\sigma_{\mu\nu}-\beta_2\dot{\pi}_{\mu\nu}+\frac{1}{2}T\partial_{\lambda}\left(\frac{\beta_2}{T}u^{\lambda}\right)\pi_{\mu\nu}+\alpha_1\nabla_{\langle\mu_{u^{\nu}}\rangle}\right]. \tag{2.31}$$

The symbols such as $\dot{X}$ represent the time derivative of X. The second law of thermodynamics, $\partial_{\mu}S^{\mu}\geq 0$, will be satisfied if the right hand side of the equation 2.31 is a sum of squares. This condition leads to the following relaxation equations for dissipative fluxes

$$\tau_{\Pi}\dot{\Pi}+\Pi = -\zeta\theta-\left[\frac{1}{2}\zeta T\partial_{\mu}\left(\frac{\tau_0}{\zeta T}u^{\mu}\right)\Pi\right]+\tau_0\nabla_{\mu}q^{\mu}, \tag{2.32}$$

$$\tau_{\pi}\Delta^{\alpha}_{\mu}\Delta^{\beta}_{\nu}\dot{\pi}_{\alpha\beta}+\pi_{\mu\nu} = 2\eta\sigma_{\mu\nu}-\left[\eta T\partial_{\lambda}\left(\frac{\tau_2}{2\eta T}u^{\lambda}\right)\pi_{\mu\nu}\right]+\tau_2\nabla_{\langle\mu_{q^{\nu}}\rangle}, \tag{2.33}$$

$$\tau_q\Delta^{\nu}_{\mu}\dot{q}_{\nu}+q_{\mu} = \lambda\left(\nabla_{\mu}T-T\dot{u}_{\mu}\right)+\left[\frac{1}{2}\lambda T^2\partial_{\nu}\left(\frac{\tau_1}{\lambda T^2}u^{\nu}\right)q_{\mu}\right]. \tag{2.34}$$

Where the relaxation time for bulk, shear, and heat flow are given by

$$\tau_{\Pi}=\zeta\beta_0\,,\quad \tau_{\pi}=2\eta\beta_2,\quad \tau_q=\lambda T\beta_1. \tag{2.35}$$

The coupling coefficients are given by

$$\tau_0=\zeta\alpha_0\,,\quad \tau_1=\lambda T\alpha_1\,,\quad \tau_2=2\eta\alpha_1 \tag{2.36}$$

The relaxation times are function of thermodynamic quantities like energy and number density and can be calculated from kinetic theory. A detailed analysis from kinetic theory also leads to the same form of transport equations but with some additional terms [93]. The phenomenological approach used here relies on the fact that the system is close to the equilibrium state. In this approximation, the dissipative fluxes should be smaller compared to the equilibrium thermodynamic variables

$$|\Pi|<<p,\quad \left(\pi_{\mu\nu}\pi^{\mu\nu}\right)^{1/2}<<p,\quad \left(-q_{\mu}q^{\mu}\right)^{1/2}<<\epsilon. \tag{2.37}$$

Choice of frame

So far, the hydrodynamic four velocity u^μ is arbitrary. With a proper physical choice of u^μ, one can define relevant macroscopic quantities such as energy density, number density, heat flow, and entropy density of any fluid. There are two commonly used definition of u^μ, one due to Eckart and the other due to Landau-Lifshitz [100]. According to Eckart definition u^μ is parallel to the particle four flow N^μ

$$u^\mu_{\rm E} \equiv \frac{N^\mu}{\sqrt{N_\nu N^\nu}} \ . \tag{2.38}$$

Another way to interpret this frame is to take the product of N^μ with the projector operator defined as $\Delta_{\mu\nu} = (g^{\mu\nu} - u^\mu u^\nu)$. Since the projector operator is perpendicular to the four velocity u^μ by definition, it leads to

$$\Delta_{\mu\nu} N^\nu = 0. \tag{2.39}$$

This new definition implies that in the local rest frame of the fluid the spatial component of the N^μ vanishes.

The other choice is due to Landau-Lifshitz. Here u^μ is parallel to the energy flow

$$u^\mu_{\rm L} \equiv \frac{T^\mu_\nu u^\nu_{\rm L}}{\sqrt{u_{{\rm L}\alpha} T^{\alpha\beta} T_{\beta\gamma} u^\gamma_{\rm L}}} \ . \tag{2.40}$$

The product of $T^{\mu\nu} u_\nu$ with the projector operator vanishes,

$$\Delta_{\sigma\mu} T^{\mu\nu} u_\nu = 0. \tag{2.41}$$

This implies that the energy flow vanishes in the local rest frame of the fluid element. It is obvious that in this frame $q^\mu \equiv 0$. The use of Landau-Lifshitz frame is advantageous

in those cases where the net particle number vanishes. Similar situation occurs in the high energy heavy ion collision at mid-rapidity, where the net baryon number is small. For our study we have used the Landau-Lifshitz definition of fluid four velocity. In the next section we will discuss the details of the numerical simulation of the viscous hydrodynamics.

2.3 Numerical setup

For any relativistic theory the co-ordinate system are four dimensional, e.g. for defining an event in a relativistic system, one use space-time co-ordinate (t, x, y, z). It is convenient to use longitudinal proper time τ and space time rapidity η_s instead of time t and z co-ordinate to describe the space-time evolution of the system formed in relativistic heavy ion collisions. The τ and η_s are related to the time t and z by the following relationship,

$$\tau = \sqrt{t^2 - z^2}, \qquad \eta_s = \frac{1}{2} ln \frac{t+z}{t-z}. \tag{2.42}$$

Constant t, z and τ, η_s lines are shown in the figure 2.3.

Depending upon symmetry of the system under investigation, the hydrodynamical simulation are mainly categorize in the following categories:

- 1+1 dimension,
- 2+1 dimension,

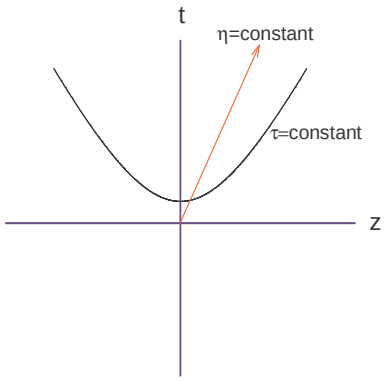

Figure 2.3: The space time diagram of co-ordinate system. Constant τ and η lines are shown.

- 3+1 dimension.

Each category can be further classified into two groups (i) ideal, and (ii) viscous. Here the convention is : dimension of space + time. The choice of using 1+1, 2+1, or 3+1D hydrodynamics simulation depends upon the symmetry of the system considered. For example, in a head on collisions between two spherically symmetric nuclei at relativistic energies, the reaction zone is azimuthally symmetric and the longitudinal boost invariance is a good approximation at midrapidity. In such cases a 1+1 dimensional hydrodynamics simulation is most effective framework to simulate the space-time evolution. For 1+1D hydrodynamics simulation the fluid variables are only function of radial distance and time. To investigate the azimuthal dependence of experimental observables, a 2+1D hydrodynamics is necessary. The table 2.1 shows the assumption and the possible observables that can be studied with hydrodynamic simulation in various dimensions. We will use (τ, x, y, η_s) co-ordinate system in our 2+1D viscous hydrodynamics code "'AZHYDRO-KOLKATA"' [83] with the assumption of longitudinal boost invariance. For a boost invariant system, the equation of motion of the fluid does

Table 2.1: Hydrodynamics simulation in various dimensions.

Dimension	Symmetry	Observables
1+1	ϕ, η	p_T spectra
2+1	η	p_T spectra and v_2
3+1	none	p_T spectra, v_2, rapidity dependence

not contain η_s explicitly. Like space-time co-ordinate, the energy-momentum four vector $p^\mu = (E, P_x, P_y, P_z)$ is relevant for a relativistic system. We will use (M_T, P_x, P_y, Y) co-ordinate system for momentum space variables. The functional relationship between the transverse mass M_T and the momentum space rapidity Y to the energy E and z component of the momentum P_z respectively, are as follows

$$M_T = \sqrt{E^2 - P_z^2}, and \quad Y = \frac{1}{2} ln \frac{E + P_z}{E - P_Z}. \tag{2.43}$$

We are using Landau-Lifshitz frame for the definition of u^μ. For this choice of frame, the non-zero transport coefficients for a relativistic imperfect fluid in a net-baryon free plasma are the shear and bulk viscosity. We will discuss here the form of $T^{\mu\nu}$ including shear and bulk viscosity along with the proper form of relaxation equations for the dissipative fluxes in detail. The metric tensor in the (τ, x, y, η_s) co-ordinate system is

$$g^{\mu\nu} = (1, -1, -1, -1/\tau^2), \quad g_{\mu\nu} = (1, -1, -1, -\tau^2). \tag{2.44}$$

The energy momentum conservation and the number conservation equation in the general curvilinear co-ordinate system takes the following forms [101]

$$T^{\mu\nu}_{;\mu} = \partial_\mu T^{\mu\nu} + \Gamma^\mu_{\mu\alpha} T^{\alpha\nu} + \Gamma^\nu_{\mu\alpha} T^{\mu\alpha} \tag{2.45}$$

$$N^\mu_{;\mu} = \partial_\mu N^\mu + \Gamma^\mu_{\mu\alpha} N^\alpha, \tag{2.46}$$

where $\Gamma^{\nu}_{\mu\alpha} = \frac{1}{2}\gamma^{\nu\rho}\left(\partial_\mu g_{\rho\alpha} + \partial_\alpha g_{\rho\mu} - \partial_\rho g_{\mu\alpha}\right)$ is the Christoffel symbol of second kind. The only non vanishing $\Gamma^{\nu}_{\mu\alpha}$'s in (τ, x, y, η_s) co-ordinate are

$$\Gamma^{\eta}_{\tau\eta} = \Gamma^{\eta}_{\eta\tau} = \frac{1}{\tau}, \tag{2.47}$$

and

$$\Gamma^{\tau}_{\eta\eta} = \tau. \tag{2.48}$$

The energy-momentum tensor including shear and bulk viscous stress is

$$\begin{aligned} T^{\mu\nu} &= T^{\mu\nu}_{eq} + \Delta T^{\mu\nu} \\ &= (\epsilon + p)u^\mu u^\nu - p g^{\mu\nu} + \Pi(u^\mu u^\nu - g^{\mu\nu}) + \pi^{\mu\nu} \\ &= (\epsilon + p + \Pi)u^\mu u^\nu - (p + \Pi)g^{\mu\nu} + \pi^{\mu\nu}. \end{aligned} \tag{2.49}$$

With the assumption of boost invariance, the energy momentum conservation equations 2.45 in (τ, x, y, η_s) co-ordinate system takes the following form (see appendix A),

$$\begin{aligned} \partial_\tau \tilde{T}^{\tau\tau} + \partial_x\left(\bar{v_x}\tilde{T}^{\tau\tau}\right) + \partial_y\left(\bar{v_y}\tilde{T}^{\tau\tau}\right) &= -\left[p + \Pi + \tau^2\pi^{\eta\eta}\right], \qquad (2.50) \\ \partial_\tau \tilde{T}^{\tau x} + \partial_x\left(v_x\tilde{T}^{\tau x}\right) + \partial_y\left(v_y\tilde{T}^{\tau x}\right) &= -\partial_x\left[\tilde{p} + \tilde{\Pi} + \tilde{\pi}^{xx} - v_x\tilde{\pi}^{\tau x}\right] - \partial_y\left[\tilde{\pi}^{yx} - v_y\tilde{\pi}^{\tau x}\right], \\ \partial_\tau \tilde{T}^{\tau y} + \partial_x\left(v_x\tilde{T}^{\tau y}\right) + \partial_y\left(v_y\tilde{T}^{\tau y}\right) &= -\partial_y\left[\tilde{p} + \tilde{\Pi} + \tilde{\pi}^{yy} - v_y\tilde{\pi}^{\tau y}\right] - \partial_x\left[\tilde{\pi}^{xy} - v_x\tilde{\pi}^{\tau y}\right], \end{aligned}$$

where $\tilde{A}^{mn} \equiv \tau A^{mn}$, $\tilde{p} \equiv \tau p$, $\bar{v}_x \equiv T^{\tau x}/T^{\tau\tau}$, and $\bar{v}_y \equiv T^{\tau y}/T^{\tau\tau}$.

The above set of coupled partial differential equations 2.50 need to be solved in order to simulate the space-time evolution of a viscous fluid. The solution of these

set of equations require initial and freeze-out condition, which are discussed in the subsequent sections. It is almost impossible to find analytical solution for these coupled partial differential equations for arbitrary initial conditions. One of the effective way to solve these coupled partial differential equations is to use numerical methods. Numerical solution is done by replacing the differential operator with difference equation and solve them on a space-time grid by using a proper algorithm. The numerical algorithm used to solve the hydrodynamics equations are discussed later. Before that let us discuss the relaxation equations for shear and bulk viscosity obtained from the Israel-Stewart theory of causal viscous hydrodynamics used in this study.

Relaxation equations for viscous stresses

For a net baryon free matter q^{μ}=0. The relaxation equation 2.32 for the bulk viscosity can be written as

$$D\Pi = -\frac{1}{\tau_{\Pi}}\left[\Pi + \zeta\nabla_{\mu}u^{\mu} + \frac{1}{2}\zeta T\Pi\partial_{\mu}(\frac{\tau_{\Pi}u^{\mu}}{\zeta T})\right], \tag{2.51}$$

where $D = u^{\mu}\partial_{\mu}$ is the convective time derivative and $\theta = \partial_{\mu}u^{\mu}$ is the expansion scalar. The above equation in (τ, x, y, η_s) co-ordinate system, with the assumption of boost invarinace becomes

$$\frac{\partial\Pi}{\partial\tau} + v_x\frac{\partial\Pi}{\partial x} + v_y\frac{\partial\Pi}{\partial y} = -\frac{1}{\tau_{\Pi}\gamma_{\tau}}\left[\Pi + \zeta\theta + \frac{1}{2}\Pi\tau_{\Pi}\partial_{\mu}u^{\mu} + \zeta T\Pi D\left(\frac{\tau_{\Pi}}{\zeta T}\right)\right]. \tag{2.52}$$

The relaxation equation 2.33 for shear stress is rearranged in the following form (by

setting $q^\mu = 0$)

$$D\pi^{\mu\nu} = \frac{1}{\tau_\pi}\left[2\eta\nabla^{<\mu}u^{\nu>} - \pi^{\mu\nu} - \eta T\partial_\lambda\left(\frac{\tau_2}{2\eta T}u^\lambda\right)\pi_{\mu\nu}\right]. \tag{2.53}$$

The equation 2.53 with the absence of last term on the right hand side is known as simplified Israel-Stewart equation. Recent calculations [93, 102] of dissipative fluid dynamics equations from kinetic theory and in conformal field theories at finite temperature shows that the relaxation equations for shear and bulk viscosity contains several new second order terms and co-efficients. The full relaxation equations for bulk and shear stresses in the kinetic theory has the following form

$$D\Pi = -\frac{1}{\tau_\Pi}\left[\Pi + \zeta\nabla_\mu u^\mu\right] - I_0, \tag{2.54}$$

$$D\pi^{\mu\nu} = \frac{1}{\tau_\pi}\left[2\eta\nabla^{<\mu}u^{\nu>} - \pi^{\mu\nu}\right] - I_1^{\mu\nu} - I_2^{\mu\nu} - I_3^{\mu\nu}. \tag{2.55}$$

Where

$$I_0 \equiv \frac{1}{2}\Pi\left(\nabla_\lambda u^\lambda + D\ln\frac{\beta_0}{T}\right), \tag{2.56}$$

$$I_1^{\mu\nu} \equiv (\pi^{\lambda\mu}u^\nu + \pi^{\lambda\nu}u^\mu)Du_\lambda, \tag{2.57}$$

$$I_2^{\mu\nu} \equiv \frac{1}{2}\pi^{\mu\nu}\left(\nabla_\lambda u^\lambda + D\ln\frac{\beta_2}{T}\right), \tag{2.58}$$

$$I_3^{\mu\nu} \equiv 2\pi_\lambda^{\langle\mu}\omega^{\nu\rangle\lambda} = \pi^{\mu\lambda}\omega^\nu{}_\lambda + \pi^{\nu\lambda}\omega^\mu{}_\lambda. \tag{2.59}$$

The term $I_1^{\mu\nu}$ is necessary for satisfying the condition of transversality and tracelessness of $\pi^{\mu\nu}$. We have incorporated $I_1^{\mu\nu}$ in our viscous hydro code, but omitted the $I_2^{\mu\nu}$ for computational simplicity in all of our calculations unless specified. The $I_3^{\mu\nu}$ term is for vorticity, which is presently neglected in our calculations. But the initial angular momentum of the two colliding nuclei for non-zero impact parameter is $\sim$1000 unit of $\hbar$. The conservation of angular momentum suggests a large angular momentum of

the reaction zone. The effect of non-zero angular momentum should be studied in details by incorporating $I_3^{\mu\nu}$ in the simulation. It is a current topic of interest and needs further study to fully understand the implication of vorticity in the fluid evolution. The condition of

(i) boost invariant velocity profile ,

(ii) tracelessness of $\pi^{\mu\nu}$ i.e. $\pi^{\mu\nu}g_{\mu\nu} = 0$, and

(iii) the orthogonality of $\pi^{\mu\nu}$ to u_μ i.e, $u_\mu\pi^{\mu\nu}$=0.

leave us with three independent components of the $\pi^{\mu\nu}$. For example, the boost invariant condition implies: $\sigma^{\eta\tau} = \sigma^{\eta x} = \sigma^{\eta y} = 0$, which gives: $\pi^{\eta\tau} = \pi^{\eta x} = \pi^{\eta y} = 0$. The zero trace condition gives: $\pi^{\tau\tau} = \pi^{xx} + \pi^{yy} + \tau^2\pi^{\eta\eta}$. The orthogonality condition leads to

$$\pi^{\tau\tau} = v_x\pi^{x\tau} + v_y\pi^{y\tau}, \tag{2.60}$$

$$\pi^{x\tau} = v_x\pi^{xx} + v_y\pi^{yx}, \tag{2.61}$$

$$\pi^{y\tau} = v_x\pi^{xy} + v_y\pi^{yy}. \tag{2.62}$$

We choose π^{xx}, π^{xy}, and π^{yy} as the three independent components of the shear stress tensor. Any other possible choice is equally good. The relaxation equations for the independent component of shear viscous stress is expressed in the following way

$$\partial_\tau\pi^{xx} + v_x\partial_x\pi^{xx} + v_y\partial_y\pi^{xx} = -\frac{1}{\tau_\pi\gamma}\left(\pi^{xx} - 2\eta\sigma^{xx}\right) - \frac{1}{\gamma}I_1^{xx}, \tag{2.63}$$

$$\partial_\tau\pi^{yy} + v_x\partial_x\pi^{yy} + v_y\partial_y\pi^{yy} = -\frac{1}{\tau_\pi\gamma}\left(\pi^{yy} - 2\eta\sigma^{yy}\right) - \frac{1}{\gamma}I_1^{yy}, \tag{2.64}$$

$$\partial_\tau\pi^{xy} + v_x\partial_x\pi^{xy} + v_y\partial_y\pi^{xy} = -\frac{1}{\tau_\pi\gamma}\left(\pi^{xy} - 2\eta\sigma^{xy}\right) - \frac{1}{\gamma}I_1^{xy}. \tag{2.65}$$

Where the components of $\sigma^{\mu\nu}$ are

$$\sigma^{xx} = -\partial_x u^x - u^x Du^x - \frac{1}{3}\Delta^{xx}\theta, \tag{2.66}$$

$$\sigma^{yy} = -\partial_y u^y - u^y Du^y - \frac{1}{3}\Delta^{yy}\theta, \tag{2.67}$$

$$\sigma^{xy} = -\frac{1}{2}[\partial_x u^y - \partial_y u^x - u^x Du^y - u^y Du^x] - \frac{1}{3}\Delta^{xy}\theta. \tag{2.68}$$

The components of the kinetic theory term $I_1^{\mu\nu}$ are

$$I_1^{xx} = 2u^x \left[\pi^{0x} Du_0 - \pi^{xx} Du_x - \pi^{yx} Du_y\right],$$

$$I_1^{yy} = 2u^y \left[\pi^{0y} Du_0 - \pi^{xy} Du_x - \pi^{yy} Du_y\right], \tag{2.69}$$

$$I_1^{xy} = \left(u^x \pi^{0y} + u^y \pi^{0x}\right) Du_0 - \left(u^x \pi^{xy} + u^y \pi^{xx}\right) Du_x - \left(u^x \pi^{yy} + u^y \pi^{yx}\right) Du_y. \tag{2.70}$$

The dependent shear stress tensor components can be obtained from the independent ones from the following relations,

$$\pi^{\tau x} = v_x \pi^{xx} + v_y \pi^{xy}, \tag{2.71}$$

$$\pi^{\tau y} = v_x \pi^{xy} + v_y \pi^{yy}, \tag{2.72}$$

$$\pi^{\tau\tau} = v_x^2 \pi^{xx} + v_y^2 \pi^{yy} + 2v_x v_y \pi^{xy}, \tag{2.73}$$

$$\tau^2 \pi^{\eta\eta} = -(1 - v_x^2)\pi^{xx} - (1 - v_y^2)\pi^{yy} + 2v_x v_y \pi^{xy}. \tag{2.74}$$

Numerical Algorithm

The numerical solution of the conservation equations 2.50 and the relaxation equations 2.63-2.65 are done with the help of a multi-dimensional flux corrected transport algorithm called Smooth And Sharp Transport Algorithm (SHASTA) [103]. Flux Corrected Transport (FCT) is known to be an accurate and effective algorithm to solve non-linear generalized continuity equation of the type which occurs in fluid dynamics [103, 104]. For example we solve the following form of equation.

$$\frac{\partial R}{\partial t} = -\frac{\partial \left(R v_x\right)}{\partial x} - \frac{\partial \left(R v_y\right)}{\partial y} - \frac{\partial \wp}{\partial x} - \frac{\partial \Phi}{\partial y}, \tag{2.75}$$

where R is the quantity to be transported, $\wp$, Φ are source terms and v is the fluid velocity. We are not going to discuss the technical details of the algorithm but will only outline the procedure, interested readers can see [103, 104] for details.

- First the physical space is divided into lattice of finite size with a fixed grid spacing. The SHASTA algorithm is Eulerian i.e, the calculation is done on a fixed grid. The quantities such as energy density, pressure, fluid velocity etc, involved in the simulation are specified on the grid points at the starting time.

- The time is divided into discrete steps. The quantities at the n+1-th step are evolved from the corresponding quantities at the n-th step.

- The differential equations are replaced by their corresponding difference equations. For example the continuity equation $\frac{\partial \rho}{\partial t} + \frac{\partial (v\rho)}{\partial x} = 0$ can be written as a difference

equation in the following form

$$\rho_i^{n+1} = \rho_i^n - \frac{v\Delta t}{\Delta x}\left[\rho_i^n - \rho_{i-1}^n\right], \tag{2.76}$$

where n denotes the time step and i is the discrete spatial step.

- To enhance the accuracy of the numerical simulation the time evolution is done in two steps. The velocities of the fluid and the source term are first calculated at half time steps $n+\frac{1}{2}$. Then using this new velocity and the new source term in the n-th step one calculates the quantities at the $n+1$-th step.

- After transporting the quantity in the next time step, one has to remove the numerical diffusion inherent to the transport scheme. This is done by calculating an anti-diffusive flux, which should be subtracted from the time-advanced quantities at the $n+1$-th step to get the final result at the $n+1$th step. The calculation of the anti-diffusion is carried out by a method called "'flux correction"'.

2.4 Initial conditions

To solve the hydrodynamics conservation equations 2.50 and the relaxation equations 2.51 and 2.53 for dissipative fluxes we need to define the values of the variables T^{xx}, T^{xy}, π^{xx} etc. at the initial time τ_0 at each grid points. To define the components of $T^{\mu\nu}$, one has to specify the values of energy density ($\epsilon(x,y)$), pressure ($P(x,y)$), initial fluid velocity ($v_x(x,y), v_y(x,y)$) and also the bulk ($\Pi(x,y)$), and shear stress ($\pi^{\mu\nu}(x,y)$). The values of these parameters are obtained from either theoretical calculations or are constrained by confronting the simulated result with the experimental data. For example,

the typical thermalization time for heavy ion collision, ranges between τ_0 ∼0.2-1.0 fm. The estimation of τ_0 value can be understood from the argument that typical time taken by two colliding nuclei to cross each other with high velocities ($\gamma \sim 10$ for RHIC), is of the order of 1 fm. In most of our calculations we will use $\tau_0 = 0.6$ fm. The effect of different choice of τ_0 on measured p_T spectra and v_2 of charged hadrons has been studied by the present author in reference [105]. The initial energy density profile is fixed in our simulation by reproducing the experimentally measured charged particle pseudorapidity density. In the next few paragraphs we will discuss about the different initial parameters and their values.

Initial energy density profile

At very high energies ($\sqrt{s_{NN}} > 10GeV$) the colliding nucleons loose most of their energy through inelastic collisions. To calculate the initial energy deposited in the reaction zone formed by the colliding nuclei, two widely used theoretical approaches are,

- Glauber Model [31], and
- Color Glass Condensate (CGC) Model [106, 107].

In general the energy density profile in the reaction zone of nucleus-nucleus collision fluctuates from event to event. This fluctuation is attributed to the fluctuation of the position of participating nucleons or to the fluctuating gluon density profile in the colliding nucleus. So far most of the hydrodynamic simulations were done for smooth

initial condition, which corresponds to an average over a large number of ensembles of identical events. In the event by event simulation of hydrodynamics, the fluctuating initial energy density profile can be calculated from either Monte-Carlo Glauber (MC-Glauber)/CGC (MC-CGC) model [76]. The fluctuating initial condition is necessary to explain the experimentally observed odd harmonics (v_3, v_5 etc.) of the particle azimuthal distribution [108].

We will use two component smoothed Glauber model initialization for all subsequent calculations unless stated otherwise. For the smooth Glauber model, the initial $\epsilon(x, y)$ is obtained in the following manner,

- for a collision with impact parameter $\vec{b}$, the transverse distribution of wounded nucleons $N_{WN}(x, y, \vec{b})$ and number of nucleon-nucleon binary collisions $N_{BC}(x, y, \vec{b})$ are calculated in a Glauber model. We will denote N_{BC} by simply number of collisions N_{coll} and the number of wounded nucleons by N_{part},
- the energy density profile $\epsilon(x, y, \vec{b})$ is assumed to have two contributions, one proportional to the $N_{coll}(x, y, \vec{b})$ and the other proportional to the $N_{part}(x, y, \vec{b})$,

$$\epsilon(x, y, b) = \epsilon_0 \left[x N_{coll} + (1 - x) \frac{N_{part}}{2} \right], \tag{2.77}$$

where ϵ_0 is a parameter which represent the central energy density for $\vec{b} = 0$ collision and x is the fraction of hard scattering. The fraction of hard scattering x is fixed by reproducing the experimentally measured charged particle pseudorapidity density per

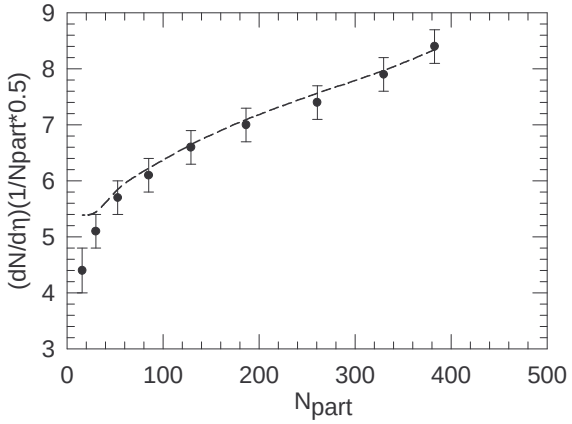

Figure 2.4: Solid circles are ALICE [110] measurement of charged particle pseudorapidity density per participating nucleon pair for different centrality at midrapidity. The dashed line is the ideal hydrodynamics simulation for the two component Glauber model initialization (equation 2.77) with hard scattering fraction x=0.9.

participant pair ($\frac{1}{0.5N_{part}}\frac{dN_{ch}}{d\eta}$) as a function of centrality (N_{part}) as shown in figure 2.4 for Pb-Pb collisions at $\sqrt{s_{NN}}$ =2.76 TeV. The typical value of x obtained for LHC and RHIC energy is x=0.9. Taking the two extreme values of $x = 0$ and 1, we have studied the effect of different initial energy density profile on the charged hadron p_T spectra and elliptic flow v_2 for RHIC energy in reference [109]. The study shows that for central collision (0-10%) the energy density initialization with $x = 1$ is preferred compared to initialization with $x = 0$. Whereas, for other collision centralities the initialization with $x = 0$ is preffered over $x = 1$. The details are discussed in appendix B. The value of the ϵ_0 is fixed by reproducing the experimentally measured charged hadron multiplicity in the most central collisions as shown in the left panel of figure 2.5 for LHC energy.

The typical energy density profile in transverse plane $(X - Y)$ for mid-central Au-Au collisions is shown in the right panel of figure 2.5. The solid blue points represents the fluid energy density at grid points and the peak height is proportional to ϵ_0. To

calculate the $N_{coll}(x,y,\vec{b})$ and $N_{part}(x,y,\vec{b})$ from Glauber model, we choose the X axis lies along the impact parameter vector $\vec{b}$ and hence we will omit the vector sign from now onwards. A non zero impact parameter 'b' collision of two spherical nuclei with different mass number 'A' and 'B' will produce the following transverse density of binary collision and wounded nucleon profile.

$$N_{coll}(x,y;b) = \sigma_{in} T_A\left(x+\frac{b}{2},y\right) T_B\left(x-\frac{b}{2},y\right) \tag{2.78}$$

$$N_{part}(x,y;b) = T_A\left(x+\tfrac{b}{2},y\right)\left(1-\left(1-\frac{1-\sigma_{in}T_B\left(x-\frac{b}{2},y\right)}{B}\right)^B\right) + T_B\left(x-\tfrac{b}{2},y\right)\left(1-\left(1-\frac{1-\sigma_{in}T_A\left(x+\frac{b}{2},y\right)}{A}\right)^A\right). \tag{2.79}$$

Where σ_{in} is the inelastic nucleon-nucleon cross section. Its value depends on the $\sqrt{s_{NN}}$ and is obtained from the experimental data. For $\sqrt{s_{NN}}$=200 and 2760 GeV collisions $\sigma_{in} \sim 40$ and 70 mb respectively. $T_{A,B}$ is the thickness function of the two colliding nuclei and is defined as $T_A(x,y)=\int_{-\infty}^{\infty} dz \rho_A(x,y,z)$; $\rho_A(x,y,z)$ is the nuclear density given by a Wood-Saxon profile: $\rho_A(\mathbf{r})=\frac{\rho_0}{1+\exp[(r-R_A)/\xi]}$. ξ and R_A are diffuseness parameter and nuclear radius respectively. The typical values of these parameter for Au and Pb nucleus which we will use in our calculation are as follows

Parameters	Au	Pb
A	197	208
ρ_0 (fm^{-3})	0.17	0.17
R_A (fm)	6.370	6.624
ξ (fm)	0.540	0.549

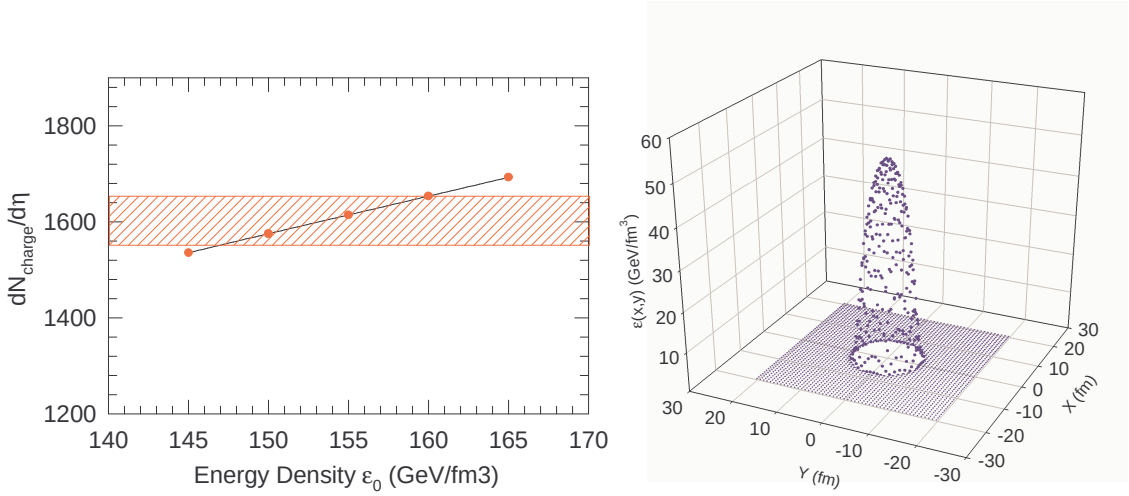

Figure 2.5: Left panel: Estimation of ϵ_0 in equation 2.77. The shaded red band is the experimentally measured charged particle multiplicity ($dN_{charge}/d\eta$) for central (0-5%) Pb-Pb collision at midrapidity for $\sqrt{s_{NN}}$=2.76 TeV [110]. The line with red circles is the ideal hydrodynamics simulation of the Pb-Pb collision with varying ϵ_0. Right panel: Typical energy density profile in transverse (X-Y) plane for mid-central Au-Au collision.

The total number of participating nucleons for a collision with impact parameter b is calculated from equation 2.79 as $N_{part}(b) = \int N_{part}(x, y; b)dxdy$. The $N_{part}(b)$ is a measure of the centrality class of nuclear collision. For most central collisions $N_{part}(b)$ is larger compared to that in the peripheral collisions. This is shown in figure 2.6 for Pb-Pb collision with inelastic nucleon-nucleon cross section σ_{in}= 70 mb which corresponds to collision at $\sqrt{s_{NN}}$=2.76 TeV.

The other choice to calculate initial energy density profile is based on CGC model which relies on the physical argument of gluon saturation at high energies. Romatschke et al. [78] have used a modified version of Kharzeev-Levin-Nardi (KLN) k_T factorization originally due to Drescher et al. [111] for initialization of energy density. Implementation and results with CGC initial condition in our relativistic viscous hydrodynamics

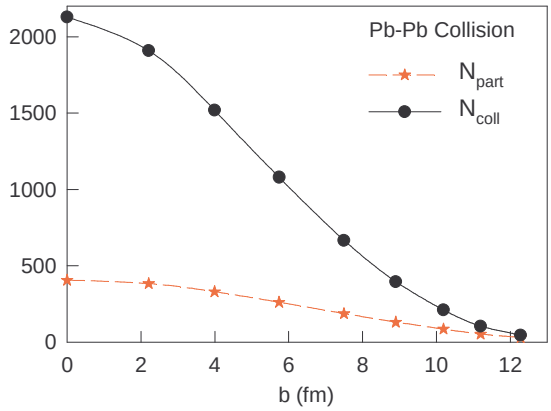

Figure 2.6: The N_{part} (red star) and N_{coll} (black circles) calculated from Glauber model are shown as a function of impact parameter b for Pb-Pb collision with $\sigma_{in} = 70$ mb.

code is discusses in the appendix C.

Initial transverse velocity

In our calculation we will use a zero initial transverse velocity $v_x(x, y) = v_y(x, y) = 0$. This choice is justified, because at the very early time, fluid expansion takes place dominantly in the longitudinal direction.

Initial shear and bulk stresses

The inadequate knowledge of the initial non-equilibrium stage of the heavy ion collision leads us to assume the initial values of the viscous stresses $\pi^{\mu\nu}$ and Π. Generally one has two options. (i) Assume the viscous effects to be vanishing at the initial time $\pi^{\mu\nu} = \Pi = 0$. Or (ii) set the quantities to their corresponding Navier-Stokes (NS)

values $\pi^{\mu\nu} = 2\eta\sigma^{\mu\nu}$ and $\Pi = -\zeta\theta$. By considering the highly non-equilibrium dynamics involved in the initial stages of the heavy-ion collision, the second choice seems to be more appropriate. For most of the simulation results discussed in this thesis we will use the NS initialization unless stated otherwise. The boost invariance flow profile for the fluid then corresponds to the following initial forms of the $\pi^{\mu\nu}$ and Π.

$$\pi^{xx}(x,y) = \pi^{yy}(x,y) = \frac{2\eta}{s(x,y)}\frac{s(x,y)}{3\tau_0}, \tag{2.80}$$

$$\pi^{xy}(x,y) = 0, \tag{2.81}$$

$$\Pi(x,y) = -\frac{\zeta}{s(x,y)}\frac{s(x,y)}{\tau_0}. \tag{2.82}$$

Relaxation time for viscous stresses

Another important input to viscous hydrodynamics simulation is the relaxation time for bulk stress (τ_Π) and shear (τ_π) stress appears in the equation 2.51 and 2.53, respectively. In principle, relaxation times τ_Π and τ_π could be calculated from the underlying kinetic theory, which for strongly coupled QCD plasma, is a complex problem. Relaxation times τ_Π and τ_π was calculated in reference [92] for simple relativistic Boltzmann, Bose, and Fermi gases with mass m using Grad 14 moment approximation in relativistic kinetic theory. For a Boltzmann gas, in the non-relativistic limit ($\beta = \frac{m}{T} \to \infty$), $\tau_\Pi = \zeta\beta_0 \approx \frac{6}{5}\frac{m^2}{T^2}\frac{\zeta}{P}$ and $\tau_\pi = 2\eta\beta_2 \approx \eta/P$, In the relativistic limit ($\beta \to 0$), $\tau_\Pi = \zeta\beta_0 = \zeta\frac{216}{P}(\frac{kT}{m})^4$ and $\tau_\pi = 2\eta\beta_2 = \frac{3\eta}{2P}$. Note that in the relativistic limit, the mass term appears in the the denominator with a quartic power. Two phases in heavy ion collision i,e. QGP and hadronic phase consist of quasiparticles of different masses, the dependence of this mass with temperature as well as the ambiguity around the crossover makes it difficult to use

τ_Π as given here. In our simulation the τ_Π is either taken as a constant or kept same as τ_π. The dependence of p_T spectra and elliptic flow on τ_π and τ_Π will be discussed in chapter-3 and 4.

2.5 Equation of State

Equation of State (EoS) is the functional relationship between thermodynamic variables pressure (P) and number density (n) to the energy density (ϵ). The conservation equations, $\partial_\mu T^{\mu\nu} = 0$, contains one additional variable than the number of equations. EoS closes the system of equations by providing another functional relationship and it is one of the important input to hydrodynamics. The speed of sound of the medium $c_s = \sqrt{\frac{\partial p}{\partial \epsilon}}$ is obtained from the EoS. In ideal hydrodynamics, c_s controls the expansion rate of the fluid under a given pressure gradient ∇P through the following relationship

$$Du^\mu = \frac{1}{\epsilon + P}\nabla^\mu P, \tag{2.83}$$

$$\frac{\partial u^\mu}{\partial \tau} = -\frac{c_s^2}{s}\partial_\mu s. \tag{2.84}$$

Where the last equation 2.84 is obtained for a special case of a baryon less fluid in its local rest frame. From equations 2.83 and 2.84, it is evident that for a larger c_s the fluid acceleration is larger for a given pressure gradient. Thus EoS influences the fluid expansion and observables like slope of the p_T spectra, anisotropic flow coefficient v_2 etc. It is then important to use an realistic EoS which is the connection between the microscopic world to the macroscopic world in hydrodynamics calculation. The effect

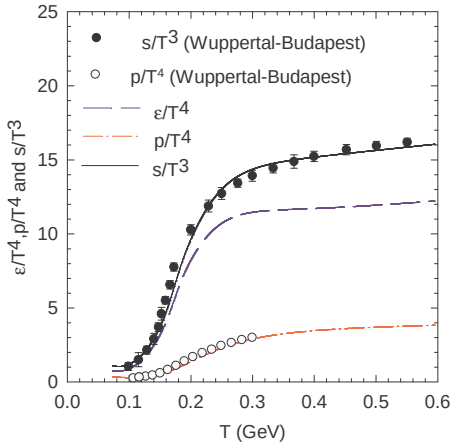

Figure 2.7: The filled circles are the lattice calculation [10] of entropy density divided by the cube of temperature. Solid black curve is the parametric fit (equation 2.85) to the lattice data. The pressure divided by the fourth power of temperature from lattice calculation is shown by the open circles. The pressure and energy density calculated from the equation 2.86, 2.87 are shown by red dashed dot and black dashed curve respectively.

of phase transition on observables like v_2 and p_T spectra of hadrons can be studied by changing EoS in hydrodynamic simulations.

The most reliable calculation of QCD equation of state is obtained from the lQCD simulation. The recent lattice calculation with 2+1 flavors and physical quark mass shows that the hadron to quark-gluon transition is a crossover at temperature T_{co} ∼175 MeV for vanishing net baryon density [10, 112]. However, the lattice simulation is not reliable at low temperature where the lattice spacing is large [113]. The thermodynamics of the nuclear matter at temperature below T_{co} can be described by assuming a system of non-interacting hadrons and their resonances. This model is known as hadron resonance gas model (hrg). For our calculation, we construct a combined lattice+hadron resonance gas EoS. Where the lattice calculation is used to obtain the EoS for the high

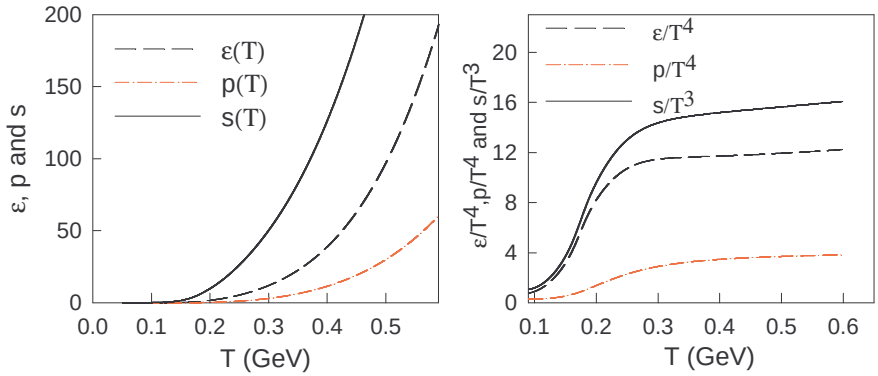

Figure 2.8: The left panel shows the energy density (dashed line), pressure (red dashed dot line) and entropy density (solid black line) as a function of temperature for the lattice+hrg equation of state. In the right panel the energy density and pressure divided by fourth power of temperature and entropy density by cube of temperature is plotted.

temperature phase (QGP), which is then smoothly joined at the crossover temperature to the hadronic EoS calculated from hadron resonance gas model. This is done in two steps: first the entropy density s_{lat}(T) of the QGP phase is obtained by parameterizing the lattice data (black solid curve in figure 2.7) [10] using the equation 2.85.

$$\frac{s_{lat}}{T^3} = \alpha + [\beta + \gamma T][1 + tanh\frac{T - T_{co}}{\Delta T}], \tag{2.85}$$

The best fit is obtained for the following values of the fit parameters $\alpha = 0.64, \beta = 6.93, \gamma = 0.55, T_{co} = 170$ MeV, and $\Delta T = 0.1 T_{co}$. The corresponding pressure and energy density (shown in figure 2.7) are calculated by the following thermodynamic relations

$$P(T) = \int_0^T s_{lat}(T')dT', \tag{2.86}$$

$$\varepsilon(T) = Ts_{lat} - P. \tag{2.87}$$

The entropy density for the hadronic phase s_{hrg}(T) is calculated from the thermodynamic relation $Ts = \epsilon + P$. Where ϵ and P for the hadronic phase are calculated in

a hadron resonance gas model by the following formulas [114]

$$\epsilon = \sum_i \frac{g_i}{(2\pi)^3} \int f_i(\vec{p}) \sqrt{\vec{p_i}^2 + m_i^2} d^3p, \tag{2.88}$$

$$P = \sum_i \frac{g_i}{(2\pi)^3} \int f_i \frac{\vec{p_i}^2}{3\sqrt{\vec{p_i}^2 + m_i^2}} d^3p. \tag{2.89}$$

Where g_i is the spin-isospin degrees of freedom for the i-th hadron species, $\vec{p_i}$ and m_i are the corresponding momentum and mass of the hadrons. The equilibrium distribution function $f_i(p)$ for bosons and fermions are given by the familiar Bose-Einstein and Fermi-Dirac distribution

$$f_i(\vec{p}) = \frac{1}{exp\left(\left(E_i - \mu_i\right)/T\right) \mp 1}, \tag{2.90}$$

where μ_i is the chemical potential for the i-th species and the temperature of the system is denoted by T. The $\mp$ in the denominator is for boson and fermion respectively. The summation over hadronic states $\sum_i$ is carried out for hadrons and resonances below mass $m_{res} < 2.5$ GeV. Figure 2.8 left panel shows the variation of ϵ, P, and s as a function of temperature from the hrg model. In the second step, the calculation of the final EoS (lattice+hrg) is done by smoothly joining the s_{lat} and s_{hrg} by the following functional form to obtain the total entropy density for the combined hadronic and QGP phases,

$$s_{combined} = \left[\frac{1 + tanh(x)}{2}\right] s_{hrg} + \left[\frac{1 - tanh(x)}{2}\right] s_{lat}. \tag{2.91}$$

Where, $x = \frac{T - T_{co}}{\Delta T}$ and $\Delta T = 0.1 T_{co}$. The pressure and energy density for the complete system is obtained from the thermodynamic relations in the equations 2.86 and 2.87 respectively, by replacing s_{lat} with the combined entropy density $s_{combined}$. Figure 2.8 right panel shows the variation of ϵ, P, and s as a function of temperature for the complete EoS. Corresponding speed of sound is shown in figure 2.9.

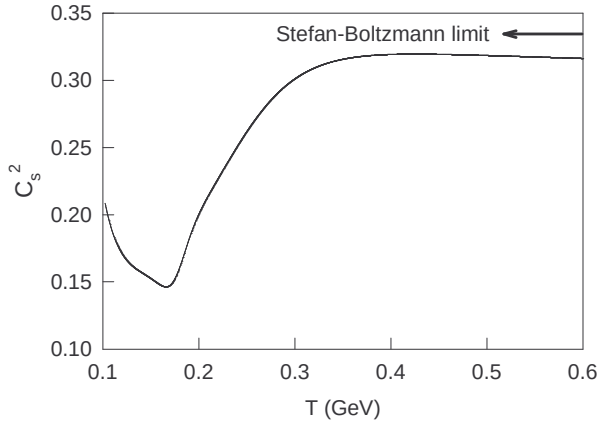

Figure 2.9: The squared speed of sound c_s^2, calculated from the complete EoS (lattice+hrg) is plotted as a function of temperature. The arrow in the top right shows the Stefan-Boltzmann limit $c_s^2 = 1/3$.

2.6 Freezeout

According to the statistical and hydrodynamics motivated models, there are two freeze-out temperature in the evolution phase of the nuclear matter formed in high energy heavy-ion collision. For a particular beam energy collision the chemical freezeout corresponds to the temperature (T_{ch}) at which the inelastic collisions stops. T_{ch} is extracted by fitting the statistical-thermal model calculation to the experimentally measured particle ratios for hadrons. Below T_{ch} the ratios of the number of observed particles are fixed. The other freezeout temperature corresponding at which elastic collision stops is known as thermal or kinetic freezeout temperature (T_{fo}). T_{fo} is generally extracted from the experimentally measured slopes of the transverse momentum distribution of hadrons by assuming a radial flow profile generated due to hydrodynamic expansion. Below T_{fo} there are no more interactions and particles energy and momenta are unchanged afterwards. Typical values of these parameter for Au-Au collision at RHIC

energy are $T_{ch} \sim 165MeV$ and $T_{fo} \sim 130MeV$[41].

First we will discuss the kinetic freezeout scenario for our hydrodynamic simulation. We have not considered the chemical freezeout scenario in our calculation. Some general arguments in support of this will be presented at the end of this section.

The hydrodynamics equations, once initialized, will give the subsequent space time evolution of the thermodynamic variables and conserved charges. The hydrodynamics equation itself does not know when to start and when to stop. The inputs necessary for starting the hydrodynamics evolution has already been discussed in the previous section. To stop the simulation we have to provide some conditions externally. One way to fix the final condition (also termed as freezeout condition) is to use the following physical argument. As the matter expands and cools, the mean free path ($\lambda_{mfp} = \frac{1}{n\sigma}$; n and σ are the number density and cross section respectively) of the constituents of the matter grows. At some later time the mean free path becomes larger compared to the system size. The local thermal equilibrium is then no longer applicable and the hydrodynamic picture breaks down. The n in the denominator of λ_{mfp} is a steep function of temperature, this leads to a freeze-out at nearly constant temperature [115]. We will use constant freezeout temperature, T_{fo} =130 MeV, for our simulation unless stated otherwise. The invariant yield EdN/d^3p of the hadrons are calculated on the freezeout hypersurface by using the Cooper-Frey algorithm [116]. This is done in the following way. The particle four current N^μ for a system of non-interacting gas is calculated from the kinetic theory definition as

$$N^\mu = \int f(x,p) p^\mu \frac{d^3p}{E}. \tag{2.92}$$

The number of particles dN crossing the freezeout surface element $d\sigma_\mu$ is

$$dN = N^\mu d\sigma_\mu. \tag{2.93}$$

By putting the kinetic theory definition of N^μ into the above equation and rearranging few terms we have

$$E\frac{dN}{d^3p} = \int f(x,p)p^\mu d\sigma_\mu, \tag{2.94}$$

which is the well known Cooper-Frey formula for calculating the invariant yield.

The single particle distribution function for a system in local thermal equilibrium is given by the following form

$$f_{eq}(x,p) = \frac{g}{(2\pi)^3}\frac{1}{exp\left(\frac{p^\mu u_\mu - \mu}{T_{fo}}\right) \mp 1}, \tag{2.95}$$

with freezeout temperature T_{fo} and chemical potential μ. g is the degeneracy factor. The $(\mp)$ are respectively for bosons and fermions. For dissipative fluids, the system is not in local thermal equilibrium. In a highly non-equilibrium system, the distribution function $f(x,p)$ is unknown. If the system is slightly off-equilibrium, then it is possible to calculate the correction to the equilibrium distribution function due to (small) non-equilibrium effects. Slightly off-equilibrium distribution function can be approximated as,

$$f(x,p) = f_{eq}(x,p) + \delta f. \tag{2.96}$$

Where $\delta f = \delta f_{bulk} + \delta f_{shear} << f_{eq}$ represents the dissipative correction to the equilibrium distribution function f_{eq}, due to bulk viscosity and shear viscosity. The form of δf_{bulk} and δf_{shear} used in our simulation will be discussed in chapters 3 and 4 .

Resonance decay contribution to pion yield

In high energy nuclear collisions various hadronic resonances are formed. The life time of most of the resonance particles are of the order of the expansion life time of the nuclear matter. The end product for the most of the decay channels involve pions. The decay of hadron resonances to pion enhances the pion yield specially at low p_T. We have used the formalism given in [117] to calculate the relative contribution of the resonance decay to thermal pion spectra. The relative contribution of the resonance decay to pion spectra is a function of both the freezeout temperature (T_{fo}) and p_T. Thus the final p_T spectra of π^- are obtained by adding the contribution from resonance decay to the thermal p_T spectra calculated from Cooper-Frey formula. For our calculation we have considered the following hadronic decay channels; $\rho^{0,-} \rightarrow \pi^-\pi^{+,0}, K^{*-,0} \rightarrow \pi^- K^{0,+}, \Delta \rightarrow \pi^- N, \omega \rightarrow \pi^+\pi^-\pi^0, \eta \rightarrow \pi^+\pi^-\pi^0$ with their corresponding branching ratios [117]. Our calculation of the π^- spectra from these decay channels and the thermal spectra for $T_{fo} = 130MeV$ are shown in figure 2.10. The p_T spectra of total π^- is shown by the red line. According to the formalism given in [117], to calculate the pion contribution form resonances we need to provide the source temperature (we have considered zero baryon chemical potential). The ratio of the total pion to the thermal pion for the calculation at two different freezeout temperature $T_{fo} = 130$ and 150 MeV are shown in figure 2.11. The parametric fit to the ratio for T_{fo}=130 and 150 MeV are

$$ratio_{(T_{fo}=130MeV)} = 1.0121 + \left(1.4028/\left(1 + \left(\frac{(p_T - 0.0134)}{0.5096}\right)^2\right)\right) \tag{2.97}$$

$$ratio_{(T_{fo}=150MeV)} = 1.0252 + \left(3.0495/\left(1 + \left(\frac{(p_T - 0.032)}{0.3881}\right)^2\right)\right). \tag{2.98}$$

About $\sim$ 50% of the total pion yield are coming from resonance decay at LHC en-

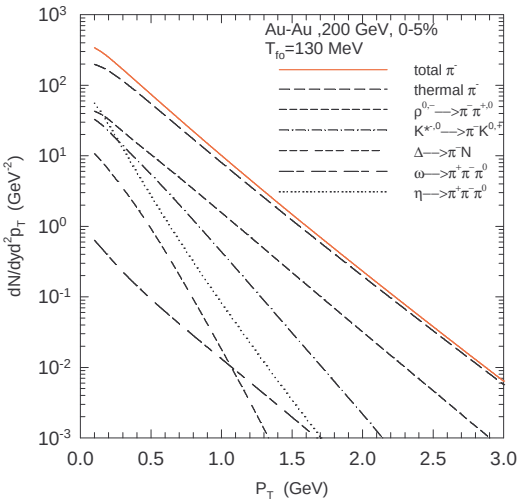

Figure 2.10: The invariant yield of π^- as a function of p_T from different decay channels. The thermal pion is from hydrodynamics simulation for Au-Au collisions. Calculation carried out for $T_{fo} = 130$ MeV. The total invariant yield of π^- is shown by the red line.

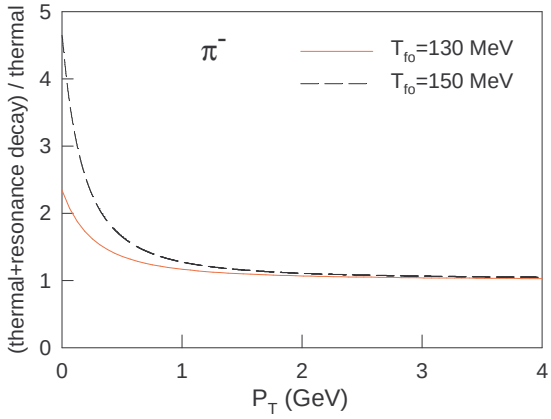

Figure 2.11: The ratio of total π^-(combination of thermal and resonance decay) to thermal π^- yields as a function of p_T for two different freezeout temperature T_{fo}=130 (red solid curve) and 150 MeV (black dashed curve). The resonance decay contribution is calculated using the framework given in [117].

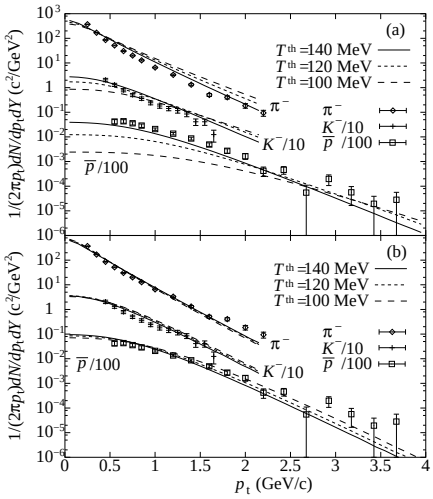

Figure 2.12: The transverse momentum spectra for negative pions, negative kaons, and antiprotons for (a) the model CE and (b) the model PCE. To see these results clearly, the yield of kaons (antiprotons) is scaled by 10^{-1} (10^{-2}). The dashed, dotted, solid lines represent results for $T^{\rm th}$ = 100, 120, and 140 MeV, respectively [118].

ergy ($\sqrt{s_{NN}}$=2.76 TeV), whereas for RHIC energy ($\sqrt{s_{NN}}$=200 GeV) the resonance contribution to total pion yield is $\sim 30\%$ for T_{fo}=130 MeV.

Notes on Chemical freezeout

In our calculation of hadron resonance gas EoS, we have considered zero chemical potential for mesons and baryons, which implies chemical equilibrium is maintained in the system. For this scenario, the ratios of particles to antiparticles are 1, and this ratio is maintained throughout the temperature range from chemical freezeout temperature T_{ch} to thermal freezeout temperature T_{fo}. To investigate the effect of early chemical freezeout on the charged hadron p_T spectra and elliptic flow Hirano et al. have done a comparative study [118]. The simulation was done for three different EoS. We will

consider two of them which are relevant for the present discussion. In reference [118] the QGP phase was considered as a gas of massless u, d, s quarks and gluons which was common for the two cases. For the hadronic phase, the two choices were (i) EoS with chemical equilibrium (CE). (ii) EoS with partial chemical equilibrium (PCE). The QGP and hadronic phases were joined with a first order phase transition. Their EoS-CE in the hadronic phase is same as ours with the only difference in the number of resonances included. We consider resonances having mass upto 2.5 GeV, they consider resonances upto $\Delta(1232)$. The other choice EoS-PCE is constructed by considering the chemical freezeout. Their simulated results for identified hadron p_T spectra for Au-Au collision at $\sqrt{s_{NN}}$=130 GeV are shown in figure 2.12. The slope and the yield of the p_T spectra of π^- and K^- for kinetic freezeout temperature 140 MeV (solid curve) remains almost same for two scenario. The anti-proton spectra on the other hand is largely modified due to the incorporation of partial chemical equilibrium in the EoS. The neglect of partial chemical equilibration in hadronic phase of the EoS used in our hydrodynamics simulation will thus introduce a negligible error in the process to extract η/s from experimental data. Because the bulk of the particles produced in a high energy nucleus collisions at RHIC and LHC are pions and kaons. They contributes $\sim 93\%$ of the total yield at top RHIC energy. Our simulation with chemical equlibriated EoS can explain both the pion and kaon spectra well (discussed in appendix D). The v_2 of inclusive charged hadrons are calculated from identified hadrons v_2 by taking the corresponding invariant yields as weight factors. Hence the main contribution to the v_2 of charged hadrons are from pions and kaons only. In summary we expect non-inclusion of chemical freeze-out in our simulation to have negligible effect on the observables discussed.

Chapter 3

Shear viscous evolution

In this chapter we will discuss the effect of shear viscosity on evolution of fluid, p_T spectra, and elliptic flow (v_2) of pions using a 2+1D relativistic viscous hydrodynamics simulation (details of which are given in chapter-2). To study the shear viscous evolution we have to solve the evolution equation for the energy-momentum tensor and the relaxation equations for shear stress tensor. In particular, the energy momentum conservation equation in presence of only shear viscosity has the following form [83, 101],

$$\begin{aligned}
\partial_\tau \tilde{T}^{\tau\tau} + \partial_x \left(\bar{v_x}\tilde{T}^{\tau\tau}\right) + \partial_y \left(\bar{v_y}\tilde{T}^{\tau\tau}\right) &= -\left[P + \tau^2\pi^{\eta\eta}\right], \\
\partial_\tau \widetilde{T}^{\tau x} + \partial_x \left(v_x\widetilde{T}^{\tau x}\right) + \partial_y \left(v_y\widetilde{T}^{\tau x}\right) &= -\partial_x\left[\widetilde{P} + \widetilde{\pi}^{xx} - v_x\widetilde{\pi}^{\tau x}\right] - \partial_y\left[\widetilde{\pi}^{yx} - v_y\widetilde{\pi}^{\tau x}\right], \\
\partial_\tau \widetilde{T}^{\tau y} + \partial_x \left(v_x\widetilde{T}^{\tau y}\right) + \partial_y \left(v_y\widetilde{T}^{\tau y}\right) &= -\partial_y\left[\widetilde{P} + \widetilde{\pi}^{yy} - v_y\widetilde{\pi}^{\tau y}\right] - \partial_x\left[\widetilde{\pi}^{xy} - v_x\widetilde{\pi}^{\tau y}\right] \quad (3.1)
\end{aligned}$$

Where $\tilde{A}^{mn} \equiv \tau A^{mn}$, $\tilde{P} \equiv \tau P$, $\overline{v}_x \equiv T^{\tau x}/T^{\tau\tau}$, and $\overline{v}_y \equiv T^{\tau y}/T^{\tau\tau}$. The relaxation equation for the component π^{xx} of the shear stress $\pi^{\mu\nu}$ is

$$\partial_\tau \pi^{xx} + v_x\partial_x\pi^{xx} + v_y\partial_y\pi^{xx} = -\frac{1}{\tau_\pi\gamma}\left(\pi^{xx} - 2\eta\sigma^{xx}\right) - \frac{1}{\gamma}I_1^{xx}. \quad (3.2)$$

The evolution equations for π^{yy} and π^{xy} are of similar form (see chapter-2). We will denote the term $I_1^{\mu\nu} \equiv (\pi^{\lambda\mu}u^{\nu}+\pi^{\lambda\nu}u^{\mu})Du_{\lambda}$ as the R-term. The effect of inclusion of this term on the fluid evolution as well as on the spectra and v_2 of pions will be discussed. It has been pointed out in [74] that the inclusion of R-term is important. The R-term ensures that throughout the evolution $\pi^{\mu\nu}$ remains traceless and it also ensures that $\pi^{\mu\nu}u_{\mu}$=0. Shear viscous evolution without the R-term is named as simplified Israel-Stewart equation in this chapter.

Initial conditions : The simulations have been done for Au-Au collisions with initial central energy density ϵ_0= 30 GeV/fm^3 and for Pb-Pb collisions with ϵ_0= 100 GeV/fm^3. These values of ϵ_0 approximately corresponds to the energy densities achieved at top RHIC energy ($\sqrt{s_{NN}}$=200 GeV) and LHC energy ($\sqrt{s_{NN}}$=2.76 TeV) respectively. The two component Glauber model initialization is used for calculating the transverse energy density profile. The impact parameter for simulating the heavy ion collisions is taken as b=7.4 fm. Initial time is 0.6 fm for both RHIC and LHC. The initial transverse velocity of the fluid is assumed to be zero ($v_x(x,y) = v_y(x,y) = 0$). At the initial time τ_0, the values of the independent component of shear stresses π^{xx}, π^{yy}, and π^{xy} are set to the corresponding Navier-Stokes values for a boost invariant expansion as,

$$\pi^{xx} = 2\eta\sigma^{xx} = \frac{2\eta}{3\tau_0},$$
$$\pi^{yy} = 2\eta\sigma^{yy} = \frac{2\eta}{3\tau_0},$$
$$\pi^{xy} = 2\eta\sigma^{xy} = 0.$$

The $\sigma^{\mu\nu}$'s are already defined in chapter-2.

Equation of State : We have used lattice+hrg equation of state with crossover transition at T_{co}=175 MeV as discussed in the previous chapter. The low temperature phase of the EoS is modeled by hadronic resonance gas, containing all the resonances with mass M_{res} $\leq$2.5 GeV. The high temperature phase is a parametrization of the recent lattice QCD calculation [10]. Entropy density of the two phases were smoothly joined at $T = T_{co}$=175 MeV by a smooth step like function.

Shear viscous coefficient : The simulations have been carried out for four different input values of η/s=0.0 (ideal) ,0.08 (KSS bound [68]), 0.12, and 0.16. They are considered to be independent of temperature.

Shear relaxation time : The default value of the shear relaxation time τ_π for the simulation results presented in this chapter is $0.5 \times (3\eta/2p)$. The effect of varying τ_π will be discussed later in this chapter.

Freezeout : The freezeout temperature is set to T_{fo}=130 MeV. The effect of a higher freezeout temperature T_{fo}=160 MeV has also been studied. The implementation of the shear viscous correction to the freezeout distribution function will be discussed in the last subsection of this chapter.

3.1 Temporal evolution of fluid

In presence of shear viscosity, the thermodynamic pressure is modified. The tracelessness of shear stress tensor $\pi^{\mu\nu}$, along with the assumption of longitudinal boost invariance ensures that the π^{xx} and π^{yy} components are positive at the initial time of the fluid evolution. Consequently, for the same thermodynamic conditions, the effective pressure is larger (see equation 3.1) in the transverse direction compared to the ideal fluid. It is then important to have some idea how various components of shear viscous stress $\pi^{\mu\nu}$ evolves in space-time. In the next section, we will first discuss the evolution of the independent components of $\pi^{\mu\nu}$ which are π^{xx}, π^{yy}, and π^{xy} according to our convention. We will also show in detail the evolution of average values of all the seven components of $\pi^{\mu\nu}$ as a function of time.

3.1.1 Evolution of shear-stress

The temporal evolution of $\pi^{xx}(x,y)$, $\pi^{yy}(x,y)$, and $\pi^{xy}(x,y)$ for two different relaxation time $\tau_\pi = 0.5 \times (3\eta/2p)$ and $\tau_\pi = 0.1 \times (3\eta/2p)$ are shown in figures 3.1 and 3.2 respectively. Results are shown in one quadrant only, values in the other quadrants can be obtained by using refelction symmetry. For impact parameter b=7.4 fm collision, the reaction zone is elliptical, the $\pi^{xx}(x,y)$, $\pi^{yy}(x,y)$ and $\pi^{xy}(x,y)$ also reflects this elliptical shape. The magnitude of π^{xx} and π^{yy} is observed to decrease with the increase in distance from the center of the reaction zone. The values also decrease with increase in τ. The value of π^{xx} and π^{yy} reduces by almost two orders of magnitude of their

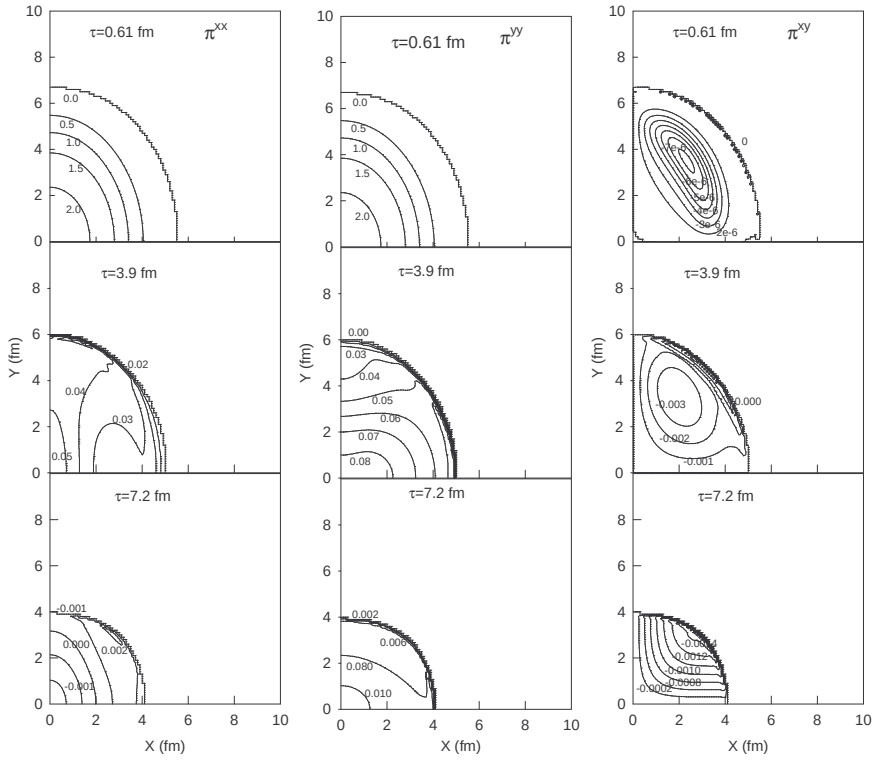

Figure 3.1: The contour plot of shear stress components in XY plane at three different times. left panel is the evolution of π^{xx}, the middle panel is for π^{yy}, and $\pi^{x,y}$ is shown in the right panel. The simulation was done for $\tau_\pi = 0.5 \times (3\eta/2p)$.

initial values at $\tau \sim 7$ fm. The $\pi^{xy}(x, y)$ however shows a non-monotonic variation with τ. Starting from zero it reaches a minimum value around $\tau \sim 3$ fm and finally goes to zero around $\tau = 8$ fm. Simulation with smaller relaxation time for shear stress shows a faster decrease in the magnitude of π^{xx}, π^{yy}, and π^{xy} with time. This is shown in figure 3.2.

The temporal evolution of the spatial average value of the various shear viscous stress components are shown in the figure 3.3. The solid red line is the simulation for $\tau_\pi = 0.5 \times (3\eta/2p)$, and the blue dashed curve is the simulation results for $\tau_\pi =$

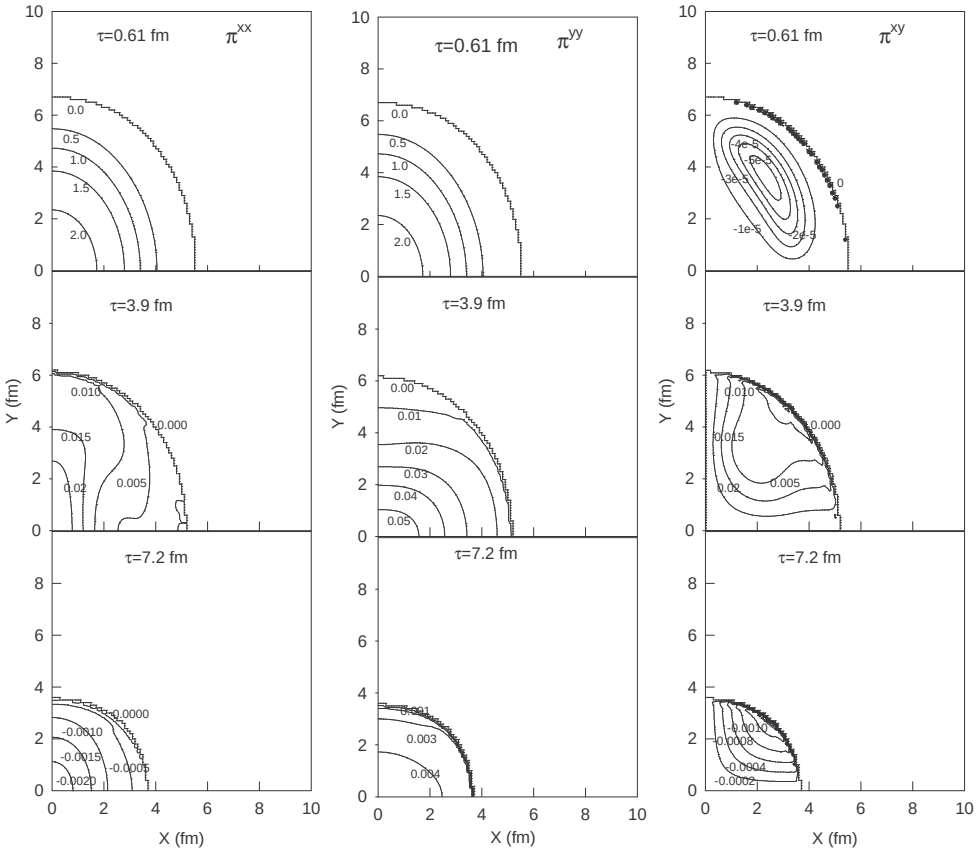

Figure 3.2: Same as figure 3.1 but for $\tau_\pi = 0.1 \times (3\eta/2p)$.

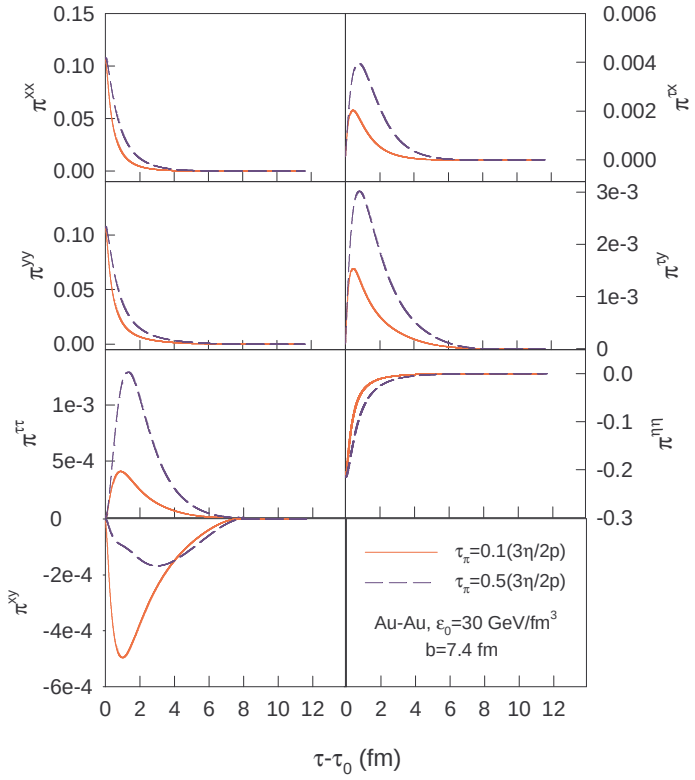

Figure 3.3: The temporal evolution of spatially averaged components of $\pi^{\mu\nu}$. The solid red and dashed black curves corresponds to the simulations with $\tau_\pi = 0.1 \times (3\eta/2p)$ and $0.5 \times (3\eta/2p)$ respectively.

$0.1 \times (3\eta/2p)$. All the shear stress components except π^{xy} and $\pi^{\eta\eta}$ remains positive during the whole evolution. Magnitude of all the components rapidly decreases with time and reaches very small value after $\sim$ 7 fm. The rate of decrease is faster for a smaller value of τ_π.

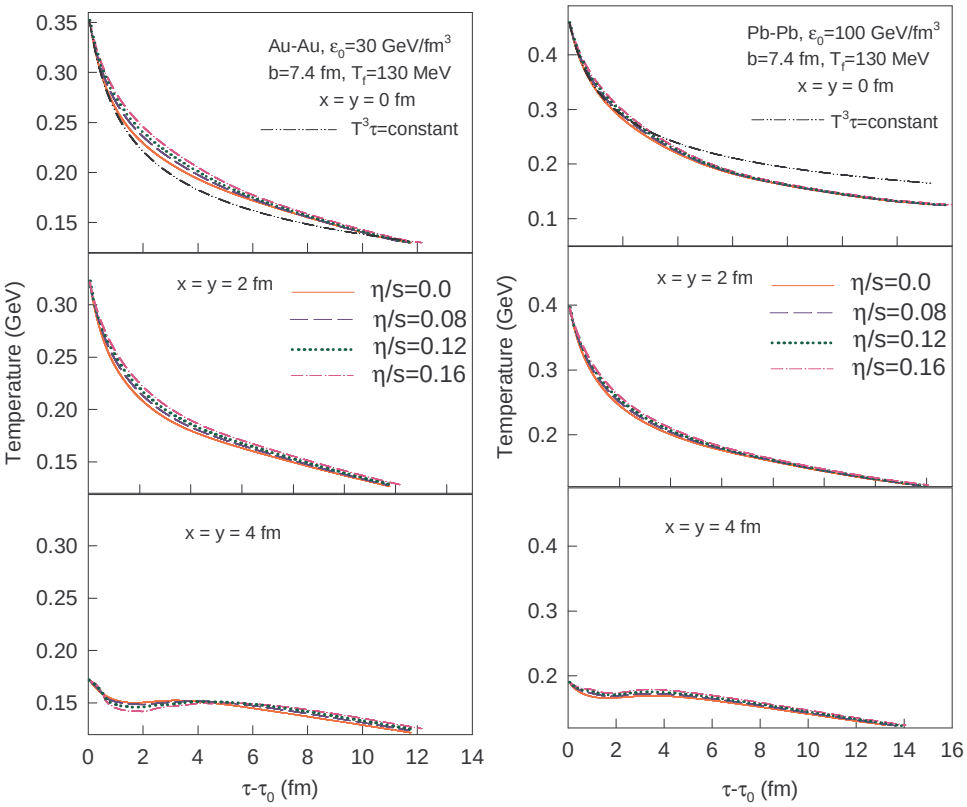

Figure 3.4: The temporal evolution of temperature at three different positions for ideal (red solid), viscous evolution with η/s=0.08 (blue dashed), 0.12 (green dotted), and 0.16 (pink dash dotted curve). For comparison the cooling according to the one dimensional Bjorken expansion is also shown (black dashed dot dot curve)for $x = y$= 0 fm. Left Panel: Simulations for Au-Au collision at b=7.4 fm with ϵ_0=30 GeV/fm^3. Right panel: Simulations for Pb-Pb collision at b=7.4 fm with ϵ_0=100 GeV/fm^3.

3.1.2 Temperature evolution

The temporal evolution of temperature of the fluid at three different spatial positions are shown in figure 3.4 for Au-Au (left panel) and Pb-Pb (right panel) collisions. The central initial energy density for Au-Au and Pb-Pb collisions are 30 GeV/fm^3 [84] and 100 GeV/fm^3 [119] respectively. The solid red, blue dashed, green dotted, and pink dash dotted curves corresponds to η/s=0 (ideal), 0.08, 0.12, and 0.16 respectively. For all the cases, the decrease in temperature with time (τ) suggests that the system cools down with time. At early times ($\sim$ 1fm) the rate of cooling is similar for one dimensional Bjorken expansion (black dashed dot dot curve) and 2+1D hydrodynamic expansion. However, after that, the rate of cooling for 2+1D expansion is slower compared to the one dimensional Bjorken expansion [86] for Au-Au collision with ϵ_0=30 GeV/fm^3. For Pb-Pb collision with a higher ϵ_0=100 GeV/fm^3, the system cools down faster with transverse expansion compared to Bjorken expansion at later times ($>$ 4 fm). In 2+1D hydrodynamics the rate of cooling is slower for a larger η/s for both of the systems considered here. Although the general features as described above remains same at other locations ($x = y$=2 fm and $x = y$=4 fm) considered here, the magnitude of the initial temperatures decreases with increasing distance from the centre. The rate of cooling also decreases as one goes from central (small x, y) to peripheral (large x, y) regions.

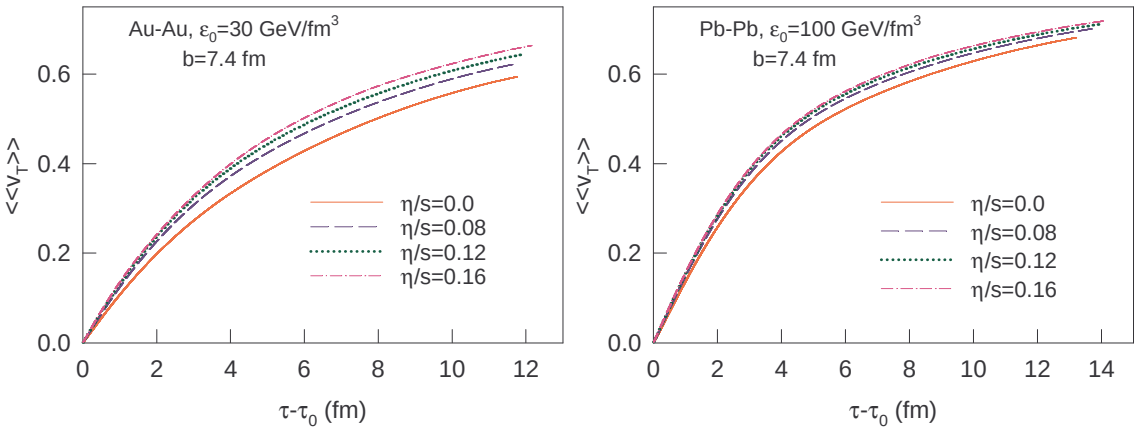

Figure 3.5: The temporal evolution of average transverse velocity $\langle\langle v_T\rangle\rangle$ of the fluid for ideal (red solid), viscous evolution with η/s=0.08 (blue dashed), 0.12 (green dotted), and 0.16 (pink dashed doted curve). Left Panel: Simulations for Au-Au collision at b=7.4 fm with ϵ_0=30 GeV/fm^3. Right panel: Simulations for Pb-Pb collision at b=7.4 fm with ϵ_0=100 GeV/fm^3.

3.1.3 Transverse flow and eccentricity

We assume the transverse velocity of the fluid at the initial time is zero for our simulation. Because of the pressure gradients, the fluid velocity in the transverse direction gradually builds up with time. The rate of increase in the transverse velocity depends on the speed of sound which in turn depends on the EoS. Figure 3.5 shows the temporal evolution of spatially averaged value of the transverse velocity $\langle\langle v_T\rangle\rangle$ for Au-Au (left panel) and Pb-Pb (right panel) collision with four different values of η/s. The spatially averaged transverse velocity is defined as $\langle\langle v_T\rangle\rangle = \frac{\langle\langle \gamma_T \sqrt{v_x^2+v_y^2}\ \rangle\rangle}{\langle\langle \gamma_T\rangle\rangle}$. Here the angular bracket$\langle\langle ...\rangle\rangle$ denotes average with respect to the energy density, and $\gamma_T = 1/\sqrt{1-v_x^2-v_y^2}$. The red solid , blue dashed, green dotted, and pink dash dotted curves are the simulated $\langle\langle v_T\rangle\rangle$ for η/s=0 (ideal), 0.08, 0.12, and 0.16 respectively. Because of the enhanced pressure in the transverse direction in the viscous fluid, the

fluid acceleration is more for shear viscous evolution than in the ideal fluid evolution. This leads to a larger $\langle\langle v_T \rangle\rangle$ for shear evolution compared to the ideal fluid evolution. The increase in $\langle\langle v_T \rangle\rangle$ is more for larger η/s. The $\langle\langle v_T \rangle\rangle$ increases faster with time for simulation with ϵ_0=100 GeV/fm^3 compared to ϵ_0=30 GeV/fm^3. In lattice+HRG EoS the speed of sound is larger in the QGP phase than in the hadronic phase. The QGP phase life time is extended for a higher initial temperature or ϵ_0. This leads to a rapid increase in the velocity for a larger ϵ_0 compared to a fluid evolution with a smaller value of ϵ_0. The pressure gradient is larger for a higher value of initial ϵ_0, correspondingly the $\langle\langle v_T \rangle\rangle$ at freezeout is larger for Pb-Pb collision with ϵ_0=100 GeV/fm^3 compared to Au-Au collision with ϵ_0=30 GeV/fm^3. The higher values of $\langle\langle v_T \rangle\rangle$ leads to a flatter p_T spectra.

A non-zero impact parameter collision between two identical nuclei leads to an elliptical collision zone. The spatial eccentricity ε_x of the collision zone is defined as

$$\varepsilon_x = \frac{\langle\langle y^2 - x^2 \rangle\rangle}{\langle\langle y^2 + x^2 \rangle\rangle}. \tag{3.3}$$

ε_x is a measure of spatial deformation of the fireball from spherical shape. A zero value of ε_x means the system is spherical, $0 < \varepsilon_x < 1$ indicates an elliptic shape with major axis along Y direction, and $\varepsilon_x < 0$ means the major axis along X direction. The angular bracket $\langle\langle ... \rangle\rangle$ implies an energy density weighted average. For b=7.4 fm collision, the evolution of ε_x with time (τ) is depicted in figure 3.6 for (a) Au-Au collision with ϵ_0=30 GeV/fm^3 and (b) Pb-Pb collision with ϵ_0=100 GeV/fm^3. Also shown in the same figure are the corresponding momentum anisotropy ε_p. Similar to the spatial anisotropy, one can define the asymmetry of fireball in momentum space.

The momentum space anisotropy ε_p is defined as

$$\varepsilon_p = \frac{\int dxdy(T^{xx} - T^{yy})}{\int dxdy(T^{xx} + T^{yy})}. \tag{3.4}$$

The solid red curve corresponds to the temporal evolution of both ε_x and ε_p for ideal fluid, the dashed, green dotted, and pink dash dotted curves are for shear viscous fluid evolution with η/s =0.08, 0.12, and 0.16 respectively. Because of the enhanced pressure gradient in shear viscous evolution, the initial spatial deformation ($\varepsilon_x \approx 0.28$ for Au-Au and ≈ 0.30 for Pb-Pb) takes a smaller time to change its shape for the shear viscous evolution compared to the ideal fluid evolution. Because of the higher initial energy density in Pb-Pb collision, the lifetime of the fireball is larger, as well as the pressure gradients, compared to Au-Au collision. Evolution for a longer time with a higher fluid velocity leads to a negative values of ε_x at the late stage $\tau \geq 9$ fm for Pb-Pb collision.

However, the rate of increase of ε_p for a viscous fluid evolution is larger compared to ideal fluid evolution at the early time. ε_p saturates at $\tau \sim 4$ fm for shear viscous evolution but continues to grow until the freezeout for ideal evolution. The trend is similar for Au-Au and Pb-Pb collisions except that the rate of increase of ε_p is faster for the later case. After $\tau \sim$4 fm, the ε_p becomes smaller for higher values of η/s. The simulated elliptic flow v_2 in hydrodynamic model is directly related to the temporal evolution of the momentum anisotropy. Hence, one should expect the values of v_2 is decreased with increase in η/s.

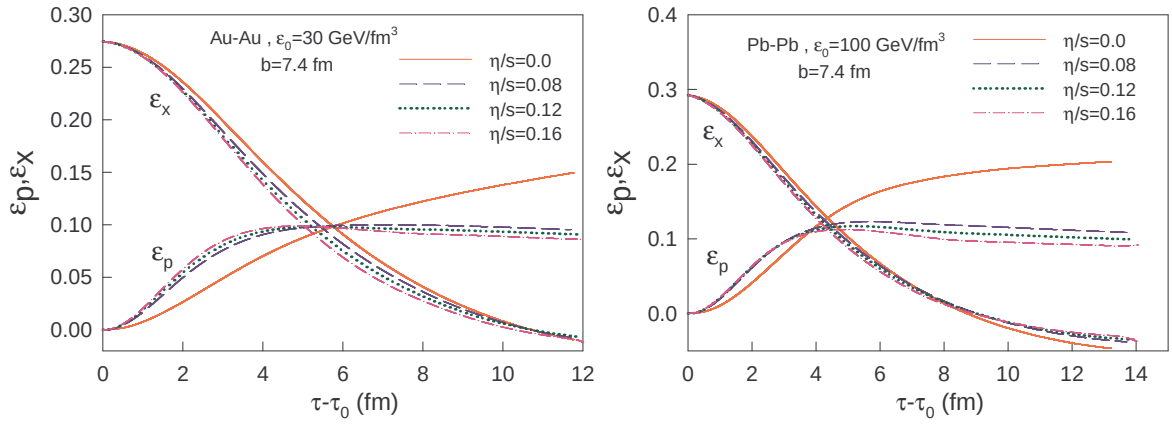

Figure 3.6: The temporal evolution of spatial eccentricity (ε_x) and momentum anisotropy (ε_p) for ideal (red solid), and viscous fluid with η/s=0.08 (blue dashed), 0.12 (green dotted), and 0.16 (pink dashed doted curve). Left Panel: Simulations for Au-Au collision at b=7.4 fm with ϵ_0=30 GeV/fm^3. Right panel: Simulations for Pb-Pb collision at b=7.4 fm with ϵ_0=100 GeV/fm^3.

3.2 Spectra and Elliptic flow

As discussed in chapter-2, there are two-fold corrections to the ideal fluid due to shear viscosity. The energy momentum tensor changes due to the dissipative fluxes, and the freezeout distribution function is also modified. If the system is in a state of near local thermal equilibrium then one can calculate the corresponding non-equilibrium correction $\delta f(x,p)$ to the equilibrium distribution function $f_{eq}(x,p)$ by making a Taylor series expansion of $f_{eq}(x,p)$ [83]. This method will break down for a system which is far away from the state of local thermal equilibrium. In this section we will concentrate on the p_T spectra and v_2 of π^- only for Au-Au collisions (a) with only shear viscous correction in $T^{\mu\nu}$ and (b) with both the shear viscous correction to $T^{\mu\nu}$ and freezeout distribution function $f_{neq}(x,p) = f_{eq}(x,p) + \delta f_{shear}$. We will also investigate about the relative correction to the invariant yield of π^- due to shear viscosity compared to

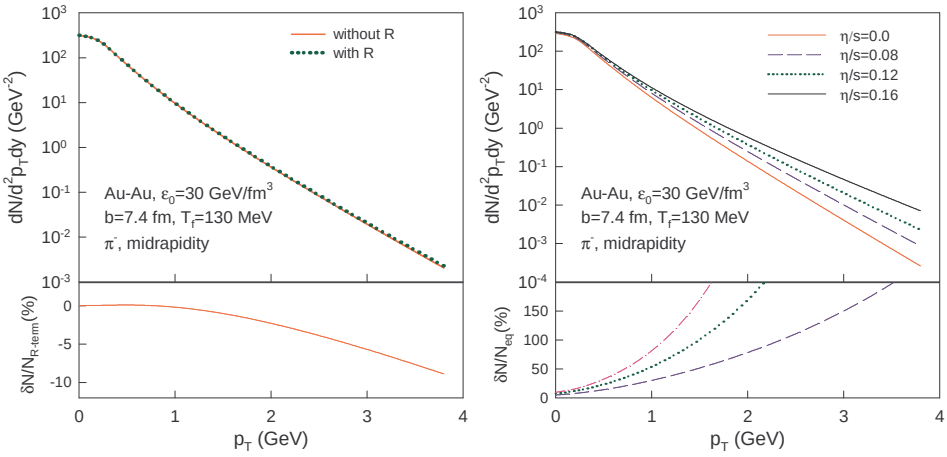

Figure 3.7: Left panel: The p_T spectra of π^- for shear viscous evolution ($\eta/s = 0.12$) with (green dot) and without (solid red curve) the R-term. The bottom panel shows the relative change in p_T spectra due to the R-term, where $\delta N = N_{R-term} - N_{withoutR-term}$. Right panel: The p_T spectra of π^- for four different values of η/s=0 (red line), 0.08 (blue dahsed line), 0.12 (green dotted line), and 0.16 (black solid line). The bottom panel shows the relative correction to the p_T spectra for shear viscosity compared to the ideal fluid. δN is the difference between shear (N_{neq}) and ideal (N_{eq}) p_T spectra.

the ideal fluid evolution. In addition, we will also discuss the contribution of R-term to shear viscous evolution. The effect of dissipative correction to the freezeout distribution function on the p_T spectra and v_2 of π^- will be presented for two values of T_{fo}=130 and 160 MeV.

3.3 Without correction to the freezeout distribution function

Figure 3.7 shows the p_T spectra of π^- in Au-Au collisions with b=7.4 fm, ϵ_0=30 GeV/fm^3, and for temperature independent η/s=0.12. The top left panel shows the

results with (green dotted line) and without (solid red line) R-term in the shear viscous evolution. The R-term ensures that throughout the evolution shear stress tensor remains traceless and transverse to the fluid velocity. The relative correction $\delta N = N_{R-term} - N_{withoutR-term}$ due to the presence of R-term in simplified Israel-Stewart equation to the p_T spectra is shown in the bottom left panel of figure 3.7. For $p_T < 3$ GeV the relative correction due to the R-term is <10%.

The top right panel of the figure 3.7 shows the p_T spectra of π^- for four different values of η/s=0, 0.08, 0.12, and 0.16. The spectra becomes flatter with increasing values of η/s. The shear viscous correction to the ideal p_T spectra is also p_T dependent, the relative correction to the invariant yield ($\delta N/N_{eq}$) for shear viscosity with respect to ideal fluid should be <1. For the current configuration we find that the relative correction remains under 50% for p_T values of 1.5, 1.0, and 0.8 GeV for η/s = 0.08, 0.12, and 0.16 respectively (shown in the bottom right panel of figure 3.7).

The corresponding results for v_2 of π^- is shown in the figure 3.8. We find the effect of R-term in shear evolution on v_2 is negligible (< 2%). The shear viscosity opposes any anisotropy in the fluid velocity arising due to the pressure gradient. Hence in presence of shear viscosity the momentum eccentricity ε_p is reduced (as seen in the left panel of figure 3.6) which leads to a reduction in value of $v_2(p_T)$ (as seen in top right panel of figure 3.8). The reduction in v_2 is more for a larger η/s. The relative correction to v_2 due to shear viscosity compared to ideal fluid is within 50% for η/s=0.16 for the p_T range studied. This is shown in the bottom right panel of figure 3.8.

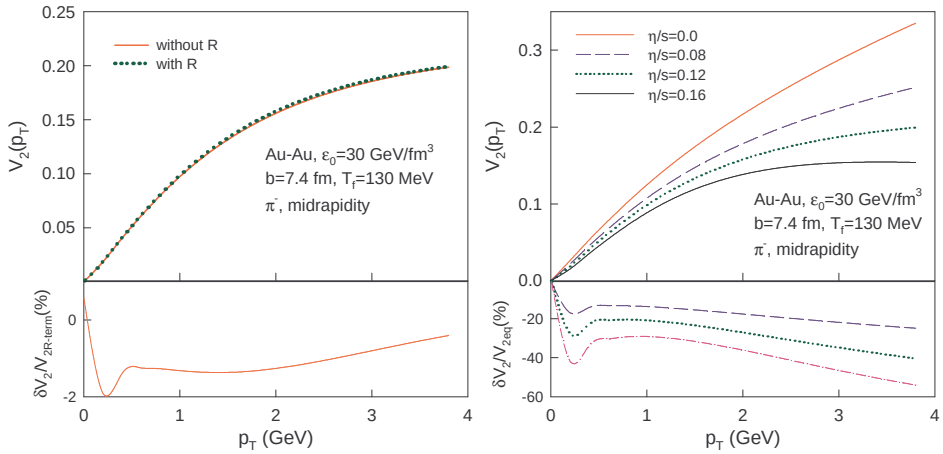

Figure 3.8: Left panel: Same as left panel of figure 3.7 but for v_2. Right panel: Same as right panel of figure 3.7 but for v_2 .

3.4 Correction to the freezeout distribution function

As discussed earlier, there are two-fold corrections to the ideal hydrodynamics due to the dissipative processes. So far all the simulated results shown in the previous sections are for shear viscous evolution with the viscous correction in $T^{\mu\nu}$ only. Here we will discuss the effect of shear viscous correction to the freezeout distribution function on p_T spectra and v_2 of π^-. The non-equilibrium correction due to shear viscosity δf_{shear} to the equilibrium freezeout distribution function f_{eq} is calculated from kinetic theory [94, 121]. The distribution function for a system slightly away from local thermal equilibrium can be approximated as [83]

$$f_{neq}(x,p) = f_{eq}(x,p)[1+\phi(x,p)], \tag{3.5}$$

where $\phi(x,p) << 1$ is the corresponding deviation from the equilibrium distribution function $f_{eq}(x,p)$. The non-equilibrium correction $\phi(x,p)$ can be approximated in

Grad's 14 moment method by a quadratic function of the four momentum p^μ in the following way [121]

$$\phi(x,p) = \varepsilon - \varepsilon_\mu p^\mu + \varepsilon_{\mu\nu} p^\mu p^\nu, \tag{3.6}$$

where ε, ε_μ, and $\varepsilon_{\mu\nu}$ are functions of p^μ, metric tensor $g^{\mu\nu}$, and thermodynamic variables. For a system where only the shear stresses exists, one can identify

$$\phi(x,p) = \varepsilon_{\mu\nu} p^\mu p^\nu, \tag{3.7}$$

where

$$\varepsilon_{\mu\nu} = \frac{1}{2(\epsilon+p)T^2}\pi_{\mu\nu}. \tag{3.8}$$

As expected the correction factor increases with increasing values of shear stress $\pi_{\mu\nu}$. The correction term also depends on the particle momentum. The Cooper-Frey formula [120] for a non equilibrium system is [94, 121]

$$\begin{aligned} \frac{dN}{d^2p_T dy} &= \frac{g}{(2\pi)^3}\int d\Sigma_\mu p^\mu f_{neq}(p^\mu u_\mu, T) \\ or, \frac{dN}{d^2p_T dy}|_{eq} + \frac{dN}{d^2p_T dy}|_{neq} &= \frac{g}{(2\pi)^3}\int d\Sigma_\mu p^\mu f_{eq}(p^\mu u_\mu, T) \\ + \frac{g}{(2\pi)^3}\int d\Sigma_\mu p^\mu \delta f_{shear}(p^\mu u_\mu, T). \end{aligned} \tag{3.9}$$

For our case, the product of particle four momentum $p^\mu = (m_T cosh y, p_x, p_y, m_T sinh y)$ and the freezeout hypersurface $d\Sigma_\mu = \left(m_T cosh\eta, -\frac{\partial\tau_f}{\partial x}, -\frac{\partial\tau_f}{\partial y} m_T sinh\eta\right)\tau_f dx dy d\eta$ is expressed as

$$p^\mu . d\Sigma_\mu = \left(m_T cosh(\eta - y) - \vec{p}_T . \vec{\nabla}_T \tau_f\right)\tau_f dx dy d\eta.$$

Using these relationships into equation 3.9 we have the correction to the invariant yield due to the shear viscosity as

$$\frac{dN}{d^2p_T dy}|_{neq} = \frac{g}{(2\pi)^3}\int_\Sigma d\Sigma_\mu p^\mu f(x,p)\phi(x,p). \tag{3.10}$$

After some algebra (see Appendix E) we have the final form of the shear viscous correction to the invariant yield of ideal fluid as

$$\frac{dN_{neq}}{dyd^2p_T} = \frac{g}{(\epsilon+p)T^2\,(2\pi)^3}\int \tau_f dxdy \sum_{n=1}^{\infty}(\mp 1)^{n+1}e^{n\beta[\gamma\vec{p}_T\vec{v}_T+\mu]}$$
$$[m_T\left[\frac{a_1}{4}k_3(n\beta_T)+\frac{3a_1}{4}k_1(n\beta_T)+\frac{a_2}{2}k_2(n\beta_T)+\frac{a_2}{2}k_0(n\beta_T)\right]$$
$$-\vec{p}_T.(\vec{\nabla}_T\tau_f)\left[\frac{a_1}{2}k_2(n\beta_T)+a_2k_1(n\beta_T)+(\frac{a_1}{2}+a_3)k_0(n\beta_T)\right]]. \tag{3.11}$$

Where

$$a_1 = m_T^2(\pi^{\tau\tau}+\tau^2\pi^{\eta\eta}),$$
$$a_2 = -2m_T(p_x\pi^{\tau x}+p_y\pi^{\tau y}), \tag{3.12}$$
$$a_3 = p_x^2\pi^{xx}+p_y^2\pi^{yy}+2p_xp_y\pi^{xy}-m_T^2\tau^2\pi^{\eta\eta}. \tag{3.13}$$

.

The top left panel of figure 3.9 shows the p_T spectra of π^- with (blue dashed and black solid curve) and without (red solid and green dotted curve) the shear viscous correction to the equilibrium freezeout distribution function for two different freeze-out temperatures T_{fo}=130 and 160 MeV respectively. The shear viscous evolution is carried out for $\eta/s = 0.12$. For a lower value of freezeout temperature (T_{fo}=130 MeV), the system evolves for a longer time compared to a higher freezeout temperature (T_{fo}=160 MeV). The shear stresses $\pi^{\mu\nu}$ decrease with time, and for a fluid evolution for longer time, their values on the freezeout hypersurface become vanishingly small (see figure 3.3). Thus depending on the values of the freezeout temperature, one would get different shear viscous correction to the freezeout distribution function. The relative shear viscous correction $\delta N/N_{wo}$ to the invariant yield of π^- for T_{fo}=130 MeV and

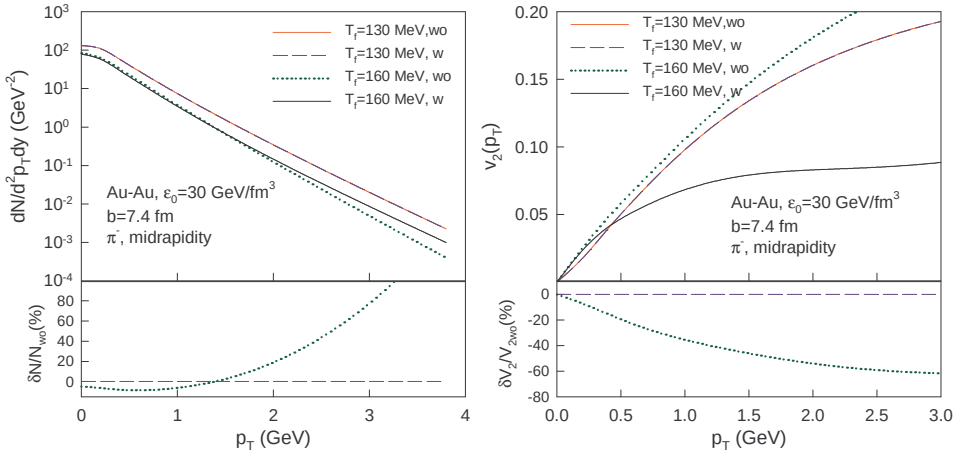

Figure 3.9: Left panel: The p_T spectra of π^- for Au-Au collision at b=7.4 fm with ϵ_0=30 GeV/fm^3 with and without the shear viscous correction to the equilibrium freezeout distribution function for two different freezeout temperature T_f=130 and 160 MeV. The left bottom panel shows the relative correction $\delta N/N_{wo}$ (see text for details) for T_f=130 (black dashed line) and T_f=160 (green dotted curve). Right panel: Same as left panel but for v_2 of π^-.

T_{fo}=160 MeV are shown in the bottom left panel of figure 3.9. Where $\delta N = N_w - N_{wo}$; N_w is the invariant yield of π^- obtained for shear viscous evolution by considering the viscous correction to both $T^{\mu\nu}$ and $f(x,p)$, and N_{wo} is the corresponding yield calculated without the viscous correction to the freezeout distribution function but only considering the corresponding viscous correction to $T^{\mu\nu}$.

We observe that for freezeout temperature T_{fo}=130 MeV, the non-equilibrium correction $\frac{dN}{d^2p_T dy}|_{neq}$ to the p_T spectra of π^- due to the δf_{shear} is zero in the p_T range considered here. This can be seen from the left bottom panel of figure 3.9, where the relative corrections $\delta N/N_{wo}$ are shown for T_{fo}=130 MeV (black-dashed line) and T_{fo}=160 MeV (green dotted curve). For T_{fo}=160 MeV, the freezeout correction is non-zero. At low p_T the correction is negative and at high p_T ($>$ 1.5 GeV) it has a positive

value. The corresponding effect of the δf_{shear} on $v_2(p_T)$ of π^- is shown in the right panel of figure 3.9. The different lines bear the same meaning as used in the left panel. Similar to the p_T spectra, the relative correction $\delta v_2/v_{2wo}$ is close to zero for T_{fo}=130 MeV. However, for the freezeout temperature T_{fo}=160 MeV, this correction is large and is of the order of 40% at $p_T \sim 1$ GeV.

Chapter 4

Bulk viscous evolution

To study the bulk viscous evolution for a relativistic fluid, we need to solve the corresponding energy-momentum conservation equations and the relaxation equations for the bulk stress (Π) of the system. The energy momentum conservation equation in presence of only bulk viscosity has the following form,

$$\begin{aligned}
\partial_\tau \tilde{T}^{\tau\tau} + \partial_x \left(\bar{v_x}\tilde{T}^{\tau\tau}\right) + \partial_y \left(\bar{v_y}\tilde{T}^{\tau\tau}\right) &= -\left[P + \Pi\right], \\
\partial_\tau \widetilde{T}^{\tau x} + \partial_x \left(v_x \widetilde{T}^{\tau x}\right) + \partial_y \left(v_y \widetilde{T}^{\tau x}\right) &= -\partial_x \left[\widetilde{P} + \widetilde{\Pi}\right], \\
\partial_\tau \widetilde{T}^{\tau y} + \partial_x \left(v_x \widetilde{T}^{\tau y}\right) + \partial_y \left(v_y \widetilde{T}^{\tau y}\right) &= -\partial_y \left[\widetilde{P} + \widetilde{\Pi}\right].
\end{aligned} \tag{4.1}$$

Where $\tilde{A}^{mn} \equiv \tau A^{mn}$, $\tilde{P} \equiv \tau P$, and $\overline{v}_x \equiv T^{\tau x}/T^{\tau\tau}$, $\overline{v}_y \equiv T^{\tau y}/T^{\tau\tau}$.

The relaxation equation for bulk stress is

$$\frac{\partial \Pi}{\partial \tau} + v_x \frac{\partial \Pi}{\partial x} + v_y \frac{\partial \Pi}{\partial y} = -\frac{1}{\tau_\Pi \gamma_T}[\Pi + \zeta\theta + \frac{1}{2}\Pi\tau_\Pi \partial_\mu u^\mu + \zeta T \Pi D\left(\frac{\tau_\Pi}{\zeta T}\right)]. \tag{4.2}$$

Where $D = u^\mu \partial_\mu$ is the convective time derivative and $\theta = \partial_\mu u^\mu$ is the expansion

scalar. $\tau_\Pi = \zeta\beta_0$ is the relaxation time for bulk viscous stress, β_0 is a constant that appears in the second order viscous hydrodynamics as discussed in chapter-2, T is the temperature, ζ is the coefficient of bulk viscosity and $\gamma_T = \frac{1}{\sqrt{1-v_x^2-v_y^2}}$.

Equation of state: In the present simulations for Au-Au collision at center of mass energy 200 GeV per nucleon, we have used an EoS with cross-over transition at T_{co}=175 MeV, as discussed in chapter-2 [119]. The low temperature phase of the EoS is modeled by the hadronic resonance gas, containing all the resonances with mass M_{res} $\leq$2.5 GeV. The high temperature phase is a parametrization of the recent lQCD calculation [10]. Entropy density of the two phases were joined at $T = T_{co}$=175 MeV by a smoothed step like function.

Bulk Viscous Coefficient: As discussed in chapter-2, the exact form of the ζ/s(T) is quite uncertain. In this thesis we choose two different temperature-dependent forms. Form-1 is shown in figure 4.1(a). It is constructed in the following way: for the QGP phase we use the formula derived in pQCD calculations, $\zeta/s = 15\frac{\eta}{s}(T)\left(1/3 - c_s^2(T)\right)^2$. The squared speed of sound $c_s^2(T)$ is calculated using the relation $c_s^2(T) = \partial P(T)/\partial\epsilon(T)\mid_s$, where the pressure $P(T)$ and the energy density $\epsilon(T)$ are obtained form the lQCD calculation [10]. The η/s(T) used in this calculation is same as given in [74] which was obtained using the lattice data [71]. The ζ/s for the hadronic phase used in form-1 is the same as calculated in [88]. The calculation was done by using a hadron resonance gas model, including all known hadrons and their resonances up to mass 2 GeV with finite volume correction to the thermodynamic quantities. It also includes an exponentially

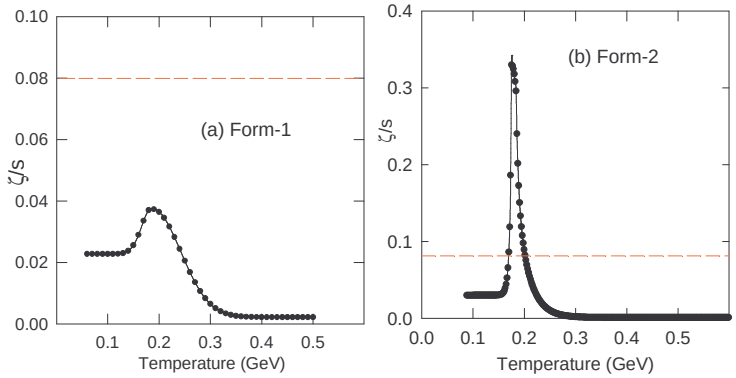

Figure 4.1: Two different forms of temperature dependence of ζ/s. (a)Form-1: ζ/s in the QGP phase (T >175 MeV) is calculated by using pQCD formula $\zeta/s = 15\frac{\eta}{s}(T)(1/3 - c_s^2(T))^2$, where c_s^2 was calculated from recent lattice data [10]. In the hadronic phase (T < 175 MeV) ζ/s is parametrized from [88]. (b)Form-2: This form is taken from [139], where in the QGP phase ζ/s was obtained from a different lattice calculation [127] and ζ/s in hadronic phase is from [88]. Red dashed line is the KSS bound [68] of the shear viscosity to entropy density ratio $\eta/s \sim 1/4\pi$.

increasing density of Hagedorn states in the mass range of 2-80 GeV.

Form-2 is shown in figure 4.1(b). This form was taken from the reference [139]. For the QGP phase the ζ/s was taken from a different lattice calculation [127]. For the hadronic phase the ζ/s was taken from [88]. The peak value of form-2 is ∼10 times larger than the peak value in form-1. Though both form of ζ/s shows a peak near the crossover temperature (T_{co} ∼175 MeV), their dependency on temperature is slightly different in the QGP phase. The red dashed line in both figures 4.1(a) and (b) shows the KSS bound of shear viscosity to entropy density ratio [68].

For comparison purposes, we will also show some simulation results with only shear viscosity. However, in this simulation, we have neglected the temperature dependence of shear viscosity to entropy density ratio. We have performed the simulations with the

AdS/CFT minimal value, $\eta/s = 1/4\pi$.

Bulk relaxation time : A brief discussion on the form and the value of bulk relaxation time τ_Π was given in chapter-2. For the simulation results presented in this chapter, the default value of τ_Π has been set to τ_π , where $\tau_\pi = \frac{3\eta}{2P}$ is the relaxation time for the shear viscous stress. To study the effect of varying relaxation time we have also carried out simulation for $\tau_\Pi = 0.1\tau_\pi$ and $5.0\tau_\pi$.

Initial conditions : The initial conditions for the 2+1D bulk viscous hydrodynamics simulations presented in this chapter are given in table 4.1. The initial energy density

Table 4.1: Initial conditions for 2+1D viscous hydrodynamics calculation.

Parameters	Values
ϵ_0	30 (GeV/fm^3)
τ_0	0.6 fm
$v_x(x,y), v_y(x,y)$	0.0
$\pi^{xx}(x,y) = \pi^{yy}(x,y), \pi^{xy}(x,y)$	$2\eta/3\tau_0$, 0
$\Pi(x,y)$	0 and $-\zeta\theta$(default)

profile in the transverse plane is obtained from a two component Glauber model, with ϵ_0 being the central energy density. In this study, we will use Navier-Stokes (NS) initialization of bulk stress, $\Pi(x,y) = -\zeta\theta$, unless stated otherwise. One can also initialize $\Pi(x,y)$ by assuming a zero value at the initial time τ_0.

Freezeout : The freezeout temperature is set to T_{fo}=130 MeV. The effect of a higher freezeout temperature T_{fo}=160 MeV has also been studied. The implementation of the

bulk viscous correction to the freezeout distribution function using Grad's 14 moment methods will be discussed in the last subsection of this chapter.

4.1 Temporal evolution of fluid

4.1.1 Evolution of bulk stress

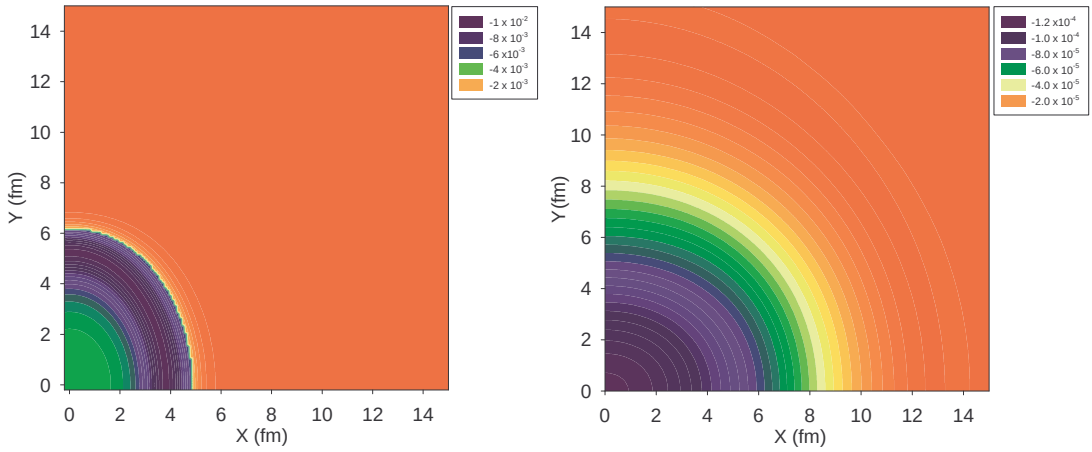

Figure 4.2: Left panel: The transverse profile of bulk stress $\Pi(x, y)$ at the initial time τ_0=0.6 fm/c. Right panel: $\Pi(x, y)$ at a later time $\tau = 11.7fm$.

The space-time evolution of $\Pi(x, y)$ is governed by the relaxation equation 4.2. The relaxation time τ_Π in equation 4.2 controls how fast the stress $\Pi(x, y)$ relaxes to its instantaneous equilibrium value. The left panel of figure 4.2 shows the initial $\Pi(x, y)$ with Navier-Stokes initialization in b=7.4 fm Au-Au collisions for form-1 of bulk viscosity. For b=7.4 fm collision, the collision zone is asymmetric. The right panel of the same figure shows the $\Pi(x, y)$ at a later time τ=11.7 fm. Within a span of ∼10 fm, bulk stress is decreased by a factor of 100. Anisotropicity of the bulk stress is also

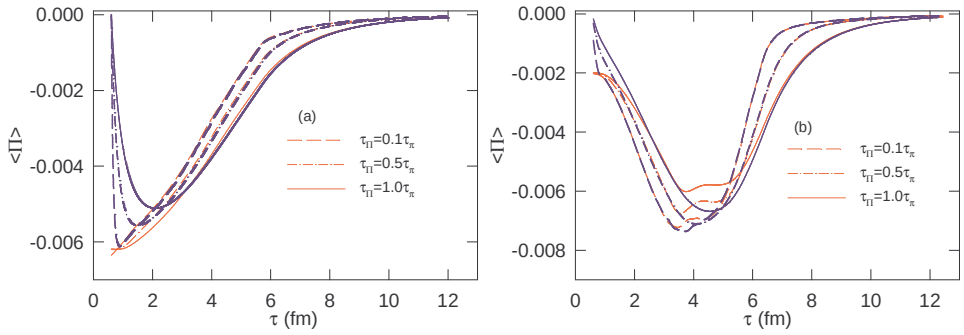

Figure 4.3: The spatially averaged bulk viscous stress $\langle\Pi\rangle$ in the transverse plane as a function of evolution time for two different initialization of $\Pi(x, y)$. (a) for ζ/s(T) form-1 and (b)ζ/s(T) form-2. The simulation with zero initial bulk stress $\Pi(x, y) = 0$ is marked as blue. Simulation for NS initialization $\Pi(x, y) = -\zeta\theta$ is marked as red. The solid, dashed dotted, and dashed lines represent the simulation with different relaxation time for $\Pi(x, y)$.

decreased. Pressure gradient is more along the minor axis (x-direction in figure 4.2), and fluid expands rapidly in that direction and hence reducing the spatial anisotropicity. Form-II of ζ/s also gives similar results. In figure 4.3(a) we show the temporal evolution of spatially averaged bulk stress, $\langle\Pi\rangle$, for two different initializations: (i) $\Pi(x, y)$=0 at the initial time τ_0 (blue lines) and (ii) Navier-Stokes (NS) initialization $\Pi(x, y) = -\zeta\theta$ (red lines) at τ_0. Results are shown for three different relaxation times: τ_Π=1.0 (solid line), 0.5 (dashed dot line), and 0.1 (dashed lines) times τ_π. $\tau_\pi = 3\eta/2P$ is the relaxation time for shear viscous stress estimated for a relativistic Boltzman gas [92].

We observe that the late time evolution of bulk stress hardly depends on the initialization of Π. Even when the Π is initialized to zero value, it quickly reaches the Navier-Stokes value. The time by which the bulk stress reaches the Navier-Stokes value depends on the relaxation time. The shorter relaxation time τ_Π drives the system to reach the equilibrium Navier-Stokes value faster, and in the limit of $\tau_\Pi \to 0$ equation 4.2

transforms to the relativistic Navier-Stokes equation. From figure 4.3 one can see that $\langle\Pi\rangle$ with zero initialization takes the least time to attain its instantaneous equilibrium value (red line) for the smallest value of τ_Π. In figure 4.3(b), same results are shown for the form-2 of ζ/s. Results are similar to that obtained for form-1 of ζ/s except the minimum of $\langle\Pi\rangle$ is shifted in time for form-2 by 2 fm .

4.1.2 Temporal evolution of temperature

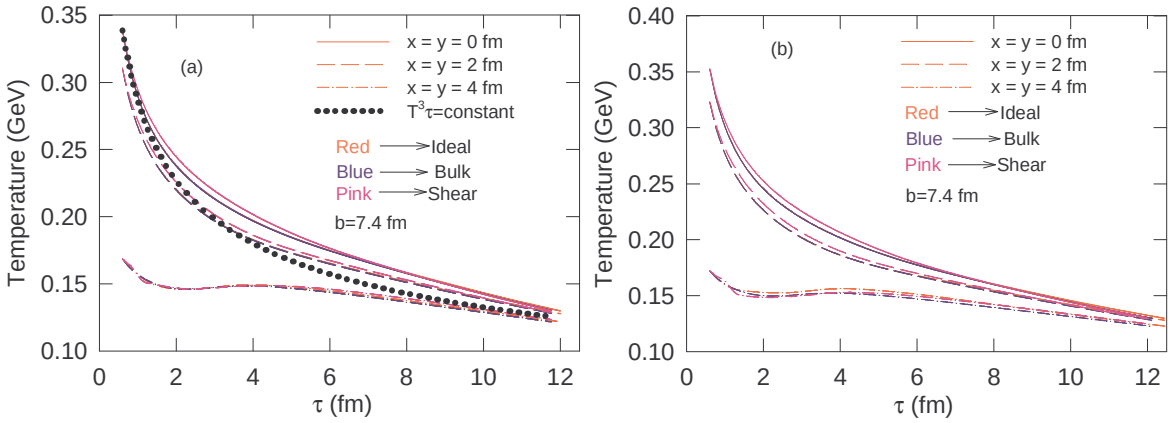

Figure 4.4: The rate of cooling for ideal, shear, and bulk viscous evolution are shown in three different locations, $x = y$=0 fm (solid line), $x = y$=2 fm (dashed line), and $x = y$=4 fm (dashed dotted line). Red line corresponds to the ideal fluid evolution, blue and pink lines are for bulk and shear viscous evolution respectively. Left panel: (a) the calculation with ζ/s form-1. Right panel: (b) with ζ/s form-2.

The rate of cooling of the fluid element for two different forms of ζ/s at three different locations in the reaction zone for ideal (red line), bulk (blue line), and shear (pink line) viscous evolution are shown in figures 4.4(a) and (b). Figure 4.4(a) is the simulation for ζ/s form-1 and 4.4(b) is for ζ/s form-2. The rate of cooling is different at various points in the reaction zone. There is no noticeable change in the rate of cooling due to bulk

viscosity compared to the ideal fluid evolution. For evolution with η/s=0.08, there is a decreases in the rate of cooling at the early time for the central region. The difference between the effects of bulk and shear stress on rate of cooling is due to the difference in magnitude of Π and $\pi^{\mu\nu}$. In the peripheral region the temperature variation is almost same for the ideal, shear, and bulk viscous evolution. Early in the evolution (∼2-3 fm), the fluid expansion is mainly in the longitudinal direction and follows Bjorken cooling law $T^3\tau = constant$. The cooling rate at the central region ($x = y$=0) for fluid expansion according to the Bjorken expansion is shown by the dotted lines in the left panel of figure 4.4 for comparison. At later time (τ >5 fm) the transverse expansion leads to a different slope for the cooling rate compared to the one dimensional Bjorken expansion.

4.1.3 Transverse velocity and eccentricity

Transverse velocity : Figures 4.5(a) and (b) show the temporal evolution of the spatially averaged transverse velocity ($\langle\langle v_T\rangle\rangle$) of the fluid with form-1 and form-2 of ζ/s respectively. The space averaged transverse velocity is defined as $\langle\langle v_T\rangle\rangle = \frac{\langle\langle \gamma\sqrt{v_x^2+v_y^2}\ \rangle\rangle}{\langle\langle\gamma\rangle\rangle}$. $\langle\langle ...\rangle\rangle$ symbol corresponds to the energy density weightage at each space points. The solid red line is for the ideal fluid and the dash-dotted and dotted lines are for bulk and shear viscous evolution respectively. Because of the reduced pressure gradient for the bulk viscous evolution compared to the ideal fluid, the corresponding $\langle\langle v_T\rangle\rangle$ is reduced for bulk viscous evolution. The reduction in $\langle\langle v_T\rangle\rangle$ at later times (after ∼ 8 fm) is greater for ζ/s form-2 than for form-1. The shear viscosity on the other hand increases

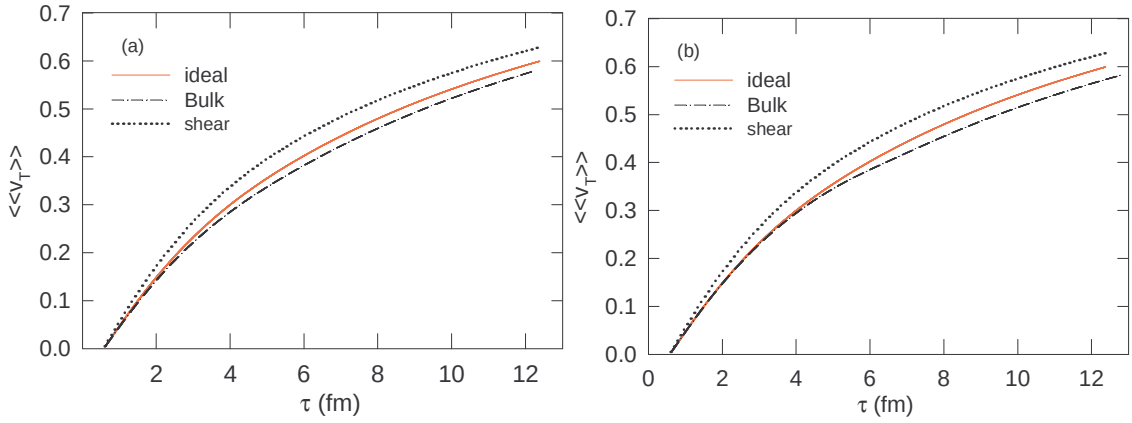

Figure 4.5: Temporal evolution of spatially averaged transverse velocity $\langle\langle v_T \rangle\rangle$ for ideal and viscous simulation. The red solid line is for the ideal fluid evolution and the dashed dot and dotted lines are for the bulk and shear viscous evolution respectively. Left panel: (a) ζ/s form-1. Right panel: (b) ζ/s form-2.

the pressure gradient in the transverse direction and reduces the longitudinal pressure at the early times of evolution. Because of the enhanced pressure gradient, $\langle\langle v_T \rangle\rangle$ for shear viscous evolution is increased compared to the ideal fluid.

Spatial and momentum eccentricity: As discussed in the previous chapter, the spatial eccentricity ε_x, defined as

$$\varepsilon_x = \frac{\langle\langle y^2 - x^2 \rangle\rangle}{\langle\langle y^2 + x^2 \rangle\rangle}, \tag{4.3}$$

is a measure of the spatial deformation of the fireball from the spherical shape. For the b=7.4 fm collision, the evolution of ε_x with time (τ) is depicted in figures 4.6(a) and (b). The solid red line corresponds to the temporal evolution of ε_x for ideal fluid, the dash-dotted, and dashed lines are for bulk and shear viscous fluid evolution respectively. Because of the reduced pressure gradient in the bulk viscous evolution compared to the

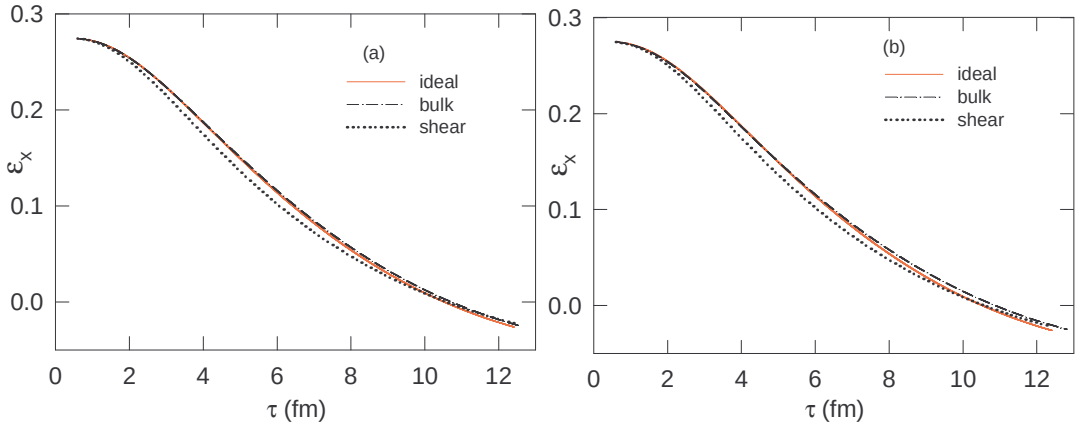

Figure 4.6: The evolution of spatial anisotropy with time. The solid red line, the dash-dotted line and the dashed lines are respectively for ideal fluid, fluid with only bulk viscosity, and fluid with only shear viscosity. Left panel: (a) ζ/s form-1. Right panel: (b) ζ/s form-2.

ideal fluid, the initial spatial deformation ($\varepsilon_x \approx 0.28$) takes a longer time to change its shape for the bulk viscous evolution compared to the ideal fluid evolution. At later time in the evolution, change in the ε_x is more pronounced for form-2 of ζ/s compared to form-1. Shear viscosity does the opposite to the transverse expansion: initially it enhances the transverse velocity and the spatial deformation ε_x reduces at a much higher rate compared to the ideal fluid evolution.

As discussed in the previous chapter, the momentum space anisotropy ε_p is defined as

$$\varepsilon_p = \frac{\int dxdy(T^{xx} - T^{yy})}{\int dxdy(T^{xx} + T^{yy})}. \tag{4.4}$$

The simulated elliptic flow v_2 in the hydrodynamic model is directly related to the temporal evolution of the momentum anisotropy. In fact in ideal hydrodynamics

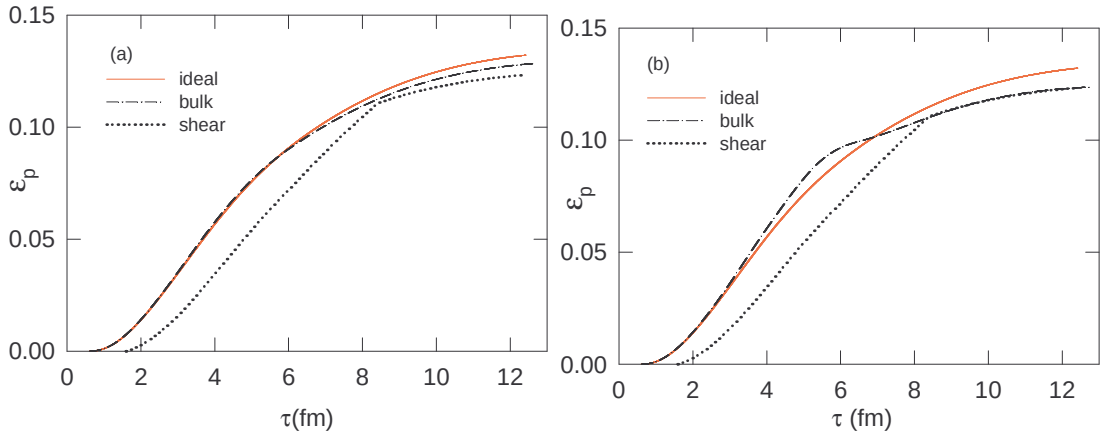

Figure 4.7: The temporal evolution of the momentum anisotropy. The lines shown here have same meaning as explained in figure 4.6. Left panel: (a) for form-1 of ζ/s and Right panel: (b) for form-2 of ζ/s.

$v_2 \propto \varepsilon_p$. The evolution of ε_p as a function of time is shown in figures 4.7(a) and (b) for ζ/s form-1 and ζ/s form-2 respectively. Compared to the ideal fluid evolution (solid red line), the bulk viscous evolution (dash-dotted line) results in a reduced value of momentum anisotropy around the freezeout time($\sim$ 12 fm) [1]. The change in ϵ_p for the bulk viscous evolution compared to the ideal fluid is prominent after $\tau \sim$ 3-4 fm of the fluid evolution. Around this time most regions of the fluid elements reaches the temperature range $\sim$ 175 MeV where ζ/s has its maximum value.

[1] Actually the freezeout happens across the whole lifetime of the fluid evolution. Here the freezeout time $\sim$ 12 fm corresponds to the time when there is no fluid element left above the specified freezeout temperature.

4.2 Effect of bulk viscosity on spectra and elliptic flow

4.2.1 Without correction to the freezeout distribution

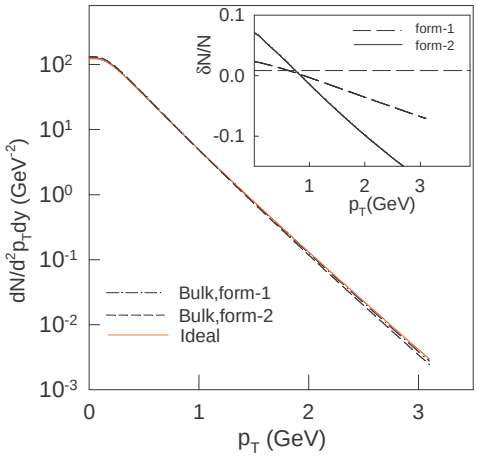

Figure 4.8: Negative charged pion's p_T spectra for Au-Au collision at impact parameter b=7.4 fm.The solid red line is the spectra from ideal fluid evolution. The dashed dot and dotted lines are for bulk viscous evolution with form-1 and form-2. The inset figure shows the ratio of correction to the p_T spectra due to bulk viscosity to ideal evolution.

We first discuss the change in particle spectra and elliptic flow due to bulk viscosity. The non-equilibrium correction to the equilibrium distribution function is neglected. The simulated charged pion p_T spectra is shown in the figure 4.8. The red solid line is the result obtained for ideal fluid simulation, the dash-dotted and dotted lines are obtained for form-1 and form-2 of bulk viscosity respectively. Due to the smaller transverse flow in presence of the bulk viscosity, we get a steeper p_T spectra compared to the ideal fluid evolution. However, the change is small. The inset of figure 4.8 shows the relative correction $\delta N/N_{eq}$ to the p_T spectra for ideal fluid (N_{eq}) due to the bulk viscosity. Where $\delta N = N_{bulk} - N_{eq}$. The correction to the p_T spectra is small: at $p_T \sim$2 GeV the

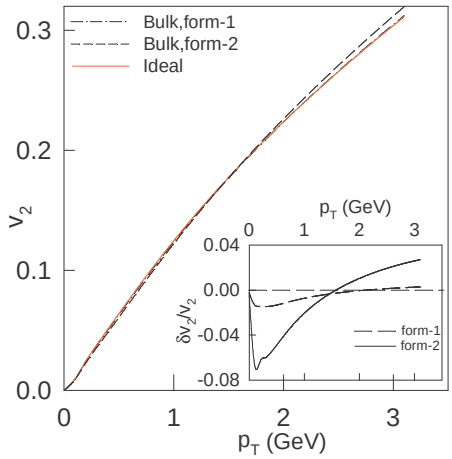

Figure 4.9: Negative charged pion's v_2 for Au-Au collision at impact parameter b=7.4 fm.The solid red line is v_2 from ideal fluid evolution. The dashed dot and dotted lines are for bulk viscous evolution with form-1 and form-2. The inset figure shows the relative correction to the v_2 due to bulk viscosity.

correction is $\sim 10\%$ with the form-2 of ζ/s. It is even less ($< 5\%$) for form-1.

The simulated elliptic flow v_2 of π^- produced in Au-Au collisions at impact parameter b=7.4 fm are shown in figure 4.9. The red solid line is the result for ideal hydrodynamics. The dash-dotted and dotted lines are v_2 with bulk viscosity of form-1 and form-2 respectively. We have not included the non-equilibrium correction to the distribution function. The inset of figure 4.9 shows the relative change in v_2 with bulk viscosity compared to the ideal fluid evolution. The relative correction in v_2 for form-1 of ζ/s is within $\sim 4\%$ for the p_T range 0-3 GeV, and for form-2 the relative correction is within $\sim 8\%$. It appears that if the non-equilibrium correction to the equilibrium distribution function is neglected, both forms of the bulk viscosity introduce relatively small corrections to the particle spectra and elliptic flow.

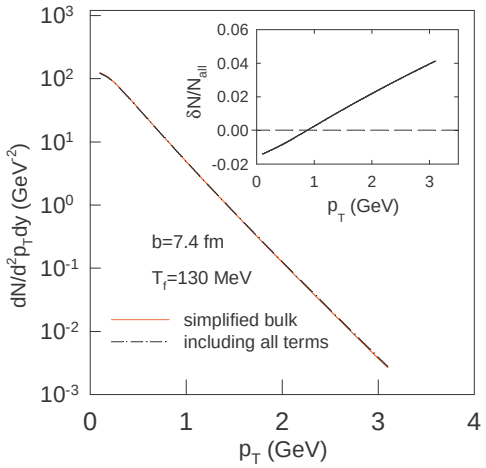

Figure 4.10: Negative charged pion's p_T spectra for Au-Au collision at impact parameter b=7.4 fm.The solid red line is for the simplified Israel-Stewart equation. The dashed dot line is the simulated result for fluid evolution with all the terms in bulk viscous relaxation equation. The inset figure shows the ratio of the relative contribution to the p_T spectra coming from the terms $\frac{1}{2}\Pi\tau_\Pi\partial_\mu u^\mu$ and $\zeta T\Pi D\left(\frac{\tau_\Pi}{\zeta T}\right)$.

Relative contribution of various terms in relaxation equation : The relaxation equation for bulk stress is given in equation 4.2. Here we discuss the contribution to the p_T spectra and elliptic flow v_2 of negative pions coming from the terms $\frac{1}{2}\Pi\tau_\Pi\partial_\mu u^\mu$ and $\zeta T\Pi D\left(\frac{\tau_\Pi}{\zeta T}\right)$ in the right hand side of the equation 4.2. The relaxation equation with only the terms $[\Pi + \zeta\theta]$ will be referred here as the simplified Israel-Stewart equation.

Figure 4.10 shows the invariant yield vs. p_T of π^- for bulk viscous evolution with (a) simplified Israel-Stewart equation (red solid line) and (b) full Israel-Stewart equation (black dashed dot line). The relative contribution to the p_T spectra due to the terms $\frac{1}{2}\Pi\tau_\Pi\partial_\mu u^\mu$ and $\zeta T\Pi D\left(\frac{\tau_\Pi}{\zeta T}\right)$ in the relaxation equation is found to be less than 4%.

Figure 4.11 shows the v_2 vs. p_T of π^- for bulk viscous evolution with (a) simpli-

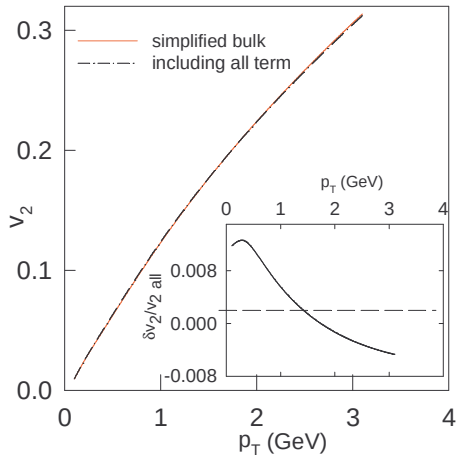

Figure 4.11: Negative charged pion's v_2 for Au-Au collision at impact parameter b=7.4 fm.The lines and the inset is the same as described in figure 4.10 but for v_2.

fied Israel-Stewart equation (red solid line) and (b) full Israel-Stewart equation (black dashed dot line). The relative contribution to the v_2 due to the terms $\frac{1}{2}\Pi\tau_\Pi\partial_\mu u^\mu$ and $\zeta T\Pi D\left(\frac{\tau_\Pi}{\zeta T}\right)$ in the relaxation equation is found to be less than 1%.

4.2.2 With correction to the freezeout distribution function

It has already been discussed a few times that there are two kinds of dissipative corrections to the ideal fluid simulation. First the energy-momentum tensor contains a viscous correction and the freezeout distribution function is also modified in presence of the dissipative processes. So far in this chapter all the bulk viscous simulation results were obtained for dissipative correction to the energy-momentum tensor only. In this section we discuss the correction to the freezeout distribution function. We have employed Grad's 14-moment methods for freezeout dissipative correction as described in reference [134]. The implementation of this method to our 2+1D viscous hydrodynamic

code "'AZHYDRO-KOLKATA"' is briefly discussed below.

Grad's 14 moment method for dissipative correction to the freezeout distribution function : We have already discussed in chapter-3 that the non-equilibrium distribution function for a system which is slightly away from equilibrium can be approximated as,

$$f(x,p) = f_{eq}(x,p) + \delta f. \tag{4.5}$$

Where $\delta f = \delta f_{bulk} + \delta f_{shear} << f$ represents the dissipative correction to the equilibrium distribution function, f_{eq}, due to bulk and shear viscosity respectively.

There are different methods available to calculate the dissipative correction to the distribution function [82, 134, 135, 139, 144, 148]. In order to maintain the continuity of the energy-momentum tensor across the freezeout surface, the functional form of the δf must fulfill the Landau matching condition; $u_\mu \Delta T^{\mu\nu} u_\nu = 0$ [148]. For bulk viscosity, the dissipative correction for a multicomponent system was calculated by using Grad's 14-moment methods in reference [134]. Following reference [134], the dissipative correction for bulk viscosity δf_{bulk} can be written in the following form,

$$\delta f_{bulk} = -f_{eq}(1 + \epsilon f_{eq}) \times \left[D_0 p^\mu u_\mu + B_0 p^\mu p^\nu \Delta_{\mu\nu} + \tilde{B}_0 p^\mu p^\nu u_\mu u_\nu \right] \Pi.$$

Where the prefactors $D_0, B_0,$ and $\tilde{B}_0$ are temperature dependent constants. For

simplicity we have dropped the index $'i'$ which was used in reference [134] to denote different types of particles. The Landau matching condition is satisfied with the present form of bulk viscous correction to the ideal distribution function. In reference [134], the prefactors D_0, B_0, and $\tilde{B}_0$ was calculated for a multicomponent hadron gas. We will use their estimated values (given in the table 4.2) in this calculation for two different freezeout temperatures T_{fo} =130 MeV and T_{fo}=160 MeV.

Table 4.2: Prefactors for two different temperatures

T_{fo}	$D_0(GeV^{-5})$	$B_0(GeV^{-6})$	$\tilde{B}_0(GeV^{-6})$
130 MeV	9.10×10^4	1.12×10^5	-3.27×10^4
160 MeV	2.01×10^4	1.66×10^4	-7.84×10^3

The bulk viscous correction $\frac{dN_{bulk}}{d^2p_Tdy}$ to the ideal spectra $\frac{dN_{eq}}{d^2p_Tdy}$ according to the Cooper-Frey formula is

$$\frac{dN_{bulk}}{d^2p_Tdy} = \frac{g}{(2\pi)^3}\int_\Sigma d\Sigma_\mu p^\mu \delta f_{bulk}(p^\mu u_\mu, T). \tag{4.6}$$

Where $p^\mu = (m_T cosh y, p_x, p_y, m_T sinh y)$ is the four momentum of the fluid. The final form of the bulk viscous correction to the invariant yield is given by [84]

$$\frac{dN_{bulk}}{d^2p_Tdy} = A[m_T\left\{\frac{b_1}{4}k_3(n\beta_\perp) + \frac{3b_1}{4}k_1(n\beta_\perp) + \frac{b_2}{2}k_0(n\beta_\perp) + \frac{b_2}{2}k_0(n\beta_\perp) + b_3k_1(n\beta_\perp)\right\}$$
$$-\vec{p}_T.\vec{\nabla}_T\tau_f\left\{\frac{b_1}{2}k_0(n\beta_\perp) + \frac{b_1}{2}k_2(n\beta_\perp) + b_2k_1(n\beta_\perp) + b_3k_0(n\beta_\perp)\right\}] \tag{4.7}$$

where $\beta_\perp = m_T\gamma\beta$, and

$$A = 2\sum_1^\infty(\mp1)^{n+1}e^{n\beta(\gamma\vec{v}_T\vec{p}_T)}\frac{g}{(2\pi)^3}\int\tau_f dxdy,$$

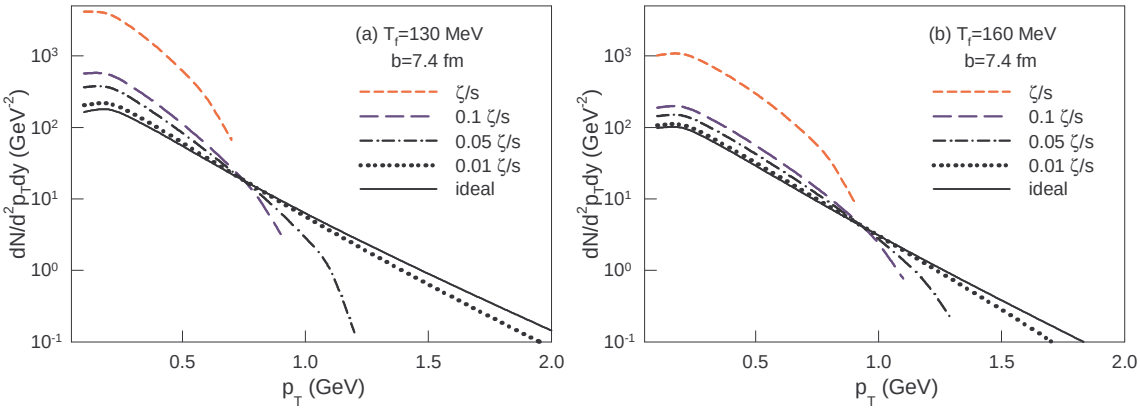

Figure 4.12: The charged pion p_T spectra for impact parameter b=7.4fm Au-Au collision. Ideal fluid evolution (black solid line) and various values of ζ/s form-1. (a) Freezeout temperature T_{fo}=130 MeV (b) T_{fo}=160 MeV.

$$
\begin{aligned}
b_1 &= m_T^2 \left(\tilde{B}_0 - B_0\right) \gamma^2, \\
b_2 &= m_T \left\{ D_0 \gamma + 2\gamma^2 \left(p^x v_x + p^y v_y\right) B_0 - 2\tilde{B}_0 \gamma^2 \left(p^x v_x + p^y v_y\right) \right\}, \\
b_3 &= B_0 m_T^2 - D_0 \gamma \left(p^x v_x + p^y v_y\right) - B_0 p_x^2 \left(1 + \gamma^2 v_x^2\right) - B_0 p_y^2 \left(1 + \gamma^2 v_y^2\right) \\
&- 2B_0 p^x v_x p^y v_y \gamma^2 + \tilde{B}_0 \gamma^2 \left(p^x v_x\right)^2 + 2\tilde{B}_0 \gamma^2 p^x v_x p^y v_y + \tilde{B}_0 \gamma^2 \left(p^y v_y\right)^2 .
\end{aligned}
$$

We will now discuss the effect of the bulk viscous correction to the freezeout distribution function on the p_T spectra and v_2 of π^- in the following paragraphs.

Figure 4.12 (a) and (b) shows the p_T spectra of pions for freezeout temperature T_{fo}=130 and 160 MeV for four different values of ζ/s form-1. The black solid line in figure 4.12 is the p_T spectra for ideal fluid evolution for b=7.4 fm Au-Au collision. The other lines are for bulk viscous evolution with varying values of form-1 ζ/s. The red dashed line is the simulated spectra with form-1 ζ/s, whereas long-dashed, dash-dotted, and dotted lines are results for 0.1, 0.05, and 0.01 times the form-1 ζ/s. It appears

that for QCD motivated bulk viscosity over entropy ratio, $(\frac{\zeta}{s})_{QCD} = 15\frac{\eta}{s}(\frac{1}{3} - c_s^2)^2$, Grad's 14-moment method introduces a very large correction to the spectra. At low p_T, compared to the ideal fluid, π^- yield is increased by a factor of 10 or more. Corrections are comparatively less if bulk viscosity is reduced. For very small bulk viscosity, e.g. for 0.01 times form-1 ζ/s, the spectra is very close to the ideal fluid evolution in the p_T range $0 < p_T < 1$ GeV.

To put things in perspective for the present calculations relative to the existing calculations in reference [134], we should compare the relative change in invariant yield of negative pions versus p_T between ideal simulation and bulk viscous simulation for both cases. In order to do that, we have to compare with the corresponding calculations done in the present work with input bulk viscosity to entropy density of $0.01 \times \zeta/s$ at T_{fo} = 160 MeV. Such a value of ζ/s is chosen so as to have a similar magnitude of Π over the freeze-out surface as used in reference [134]. We find that the relative corrections are similar.

The specific form of the dissipative correction to the ideal freezeout distribution function considered here leads to a large negative correction to the p_T spectra for higher values of p_T. Depending on the value of ζ/s, the dissipative correction due to the bulk viscosity results in a negative invariant yield above a certain value of p_T. A negative value of particle number is unphysical, we will omit the p_T range in the subsequent plots from where the particle number becomes negative. As discussed earlier, freeze-out correction is obtained under the assumption that the non-equilibrium correction to the distribution function is smaller than the equilibrium distribution function, $\delta f_{bulk} <<$

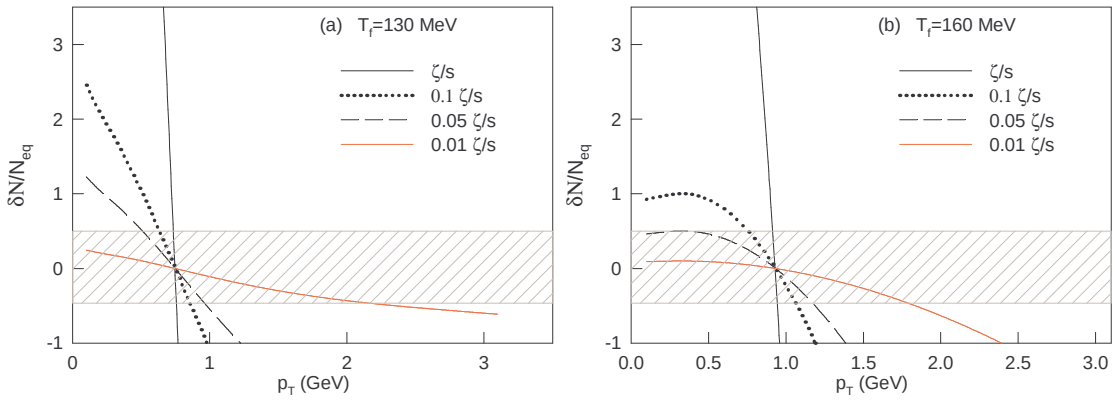

Figure 4.13: The relative correction to the p_T spectra due to the bulk viscosity compared to ideal fluid evolution. Dissipative correction in the fluid evolution as well in the freezeout distribution function has been included. Shaded region shows the relative correction of 50%.(a) Freezeout temperature T_{fo}=130 MeV (b) T_{fo}=160 MeV.

f_{eq}. It is then implied that the relative correction ($\delta N/N_{eq}$) has to be small for Israel-Stewart's hydrodynamics to be applicable. Figures 4.13 (a) and (b) show the relative correction ($\delta N/N_{eq}$) to the p_T spectra due to the bulk viscosity for T_{fo}=130 and 160 MeV respectively. The shaded bands in the figures correspond to the relative correction of 50%. We consider here a correction of magnitude greater than 50% to indicate the breakdown of the the freezeout correction procedure. From figure 4.13 one can see that the p_T spectra changes drastically in the bulk viscous evolution (solid black line) with ζ/s form-1. Only for the viscous simulation with bulk viscosity to entropy density ratio less than 0.01 times ζ/s the relative correction is less than 50%. Within the present prescription for bulk viscous correction to the freezeout distribution function, these results imposes a severe constraint on the bulk viscosity, $\frac{\zeta}{s} \leq 0.01(\frac{\zeta}{s})_{QCD}$.

We find from figures. 4.12 and 4.13 that the value of δf_{bulk} is greater for the simulations with $T_{fo} = 130$ MeV than for those with $T_{fo} = 160$ MeV. This can be understood

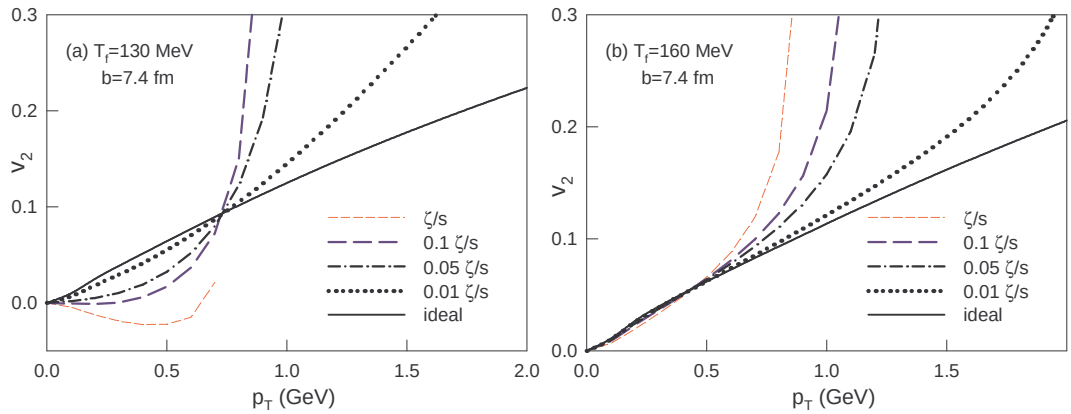

Figure 4.14: Same as figure 4.12 but for elliptic flow v_2.

in the following manner. As shown in equation 4.7, the values of Π on the freezeout surface as well as the values of the prefactors D_0, B_0, and $\tilde{B}_0$ at a given value of T_{fo} determine the magnitude of δf_{bulk}. The average magnitude of Π decreases from about -5×10^{-6} GeV/fm^3 at $T_{fo} = 160$ MeV to -2×10^{-5} GeV/fm^3 at $T_{fo} = 130$ MeV. However, the prefactor values as given in Table 4.2 increases with decrease in temperature. So the observed T_{fo} dependence of δf_{bulk} is due to the interplay of both the temperature dependence of Π and prefactors.

Figure 4.14 shows the elliptic flow of pions for b=7.4 fm Au-Au collision as a function of p_T for ideal and bulk viscous evolution. The lines represents the same conditions as described in figure 4.12. The relative correction to v_2 is defined in the same way as for the p_T spectra and is shown in figures 4.15 (a) and (b) for T_{fo}=130 MeV and 160 MeV respectively.

In all the above calculations, we have used the Boltzmann estimate for the relaxation time for shear viscosity $\tau_\Pi = \tau_\pi$. We have investigated the effect of relaxation time on

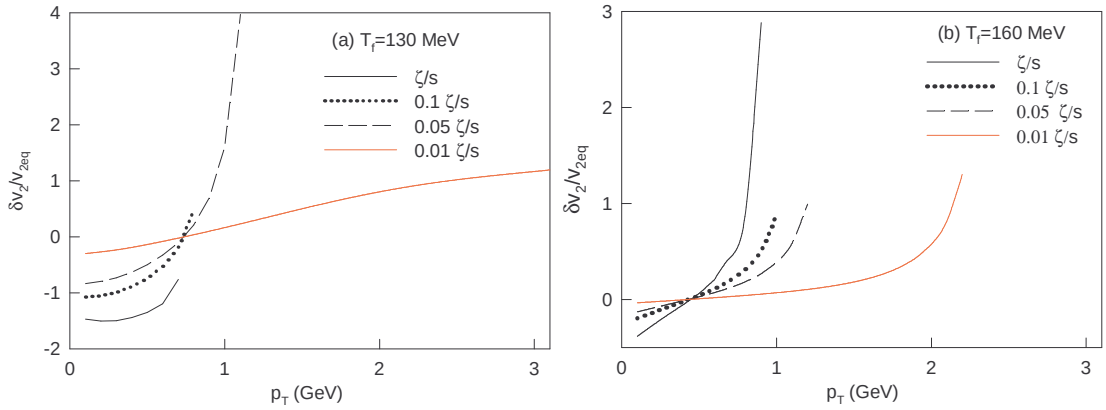

Figure 4.15: Same as figure 4.13 but for elliptic flow v_2.

the p_T spectra and elliptic flow. For relaxation times τ_Π=0.1, 1, and 5 times τ_π, we have solved the hydrodynamic evolution and computed π^- p_T spectra and elliptic flow. Results are shown in figure 4.16. If relaxation time is decreased by a factor of 10 from $\tau_\Pi = \tau_\pi$ to $\tau_\Pi = 0.1\tau_\pi$, p_T spectra or elliptic flow hardly changes. If relaxation time is increased by a factor of 5, at large p_T yield is reduced marginally. The effect is more pronounced on elliptic flow: v_2 is increased. Increased flow with increasing relaxation time can be understood as follows: bulk stress evolve comparatively slowly with increased τ_Π and the non-equilibrium correction at the freeze-out is increased. This will lead to larger v_2.

Conclusions : The effect of bulk viscosity on pion p_T spectra and elliptic flow was studied by numerically solving 2+1D relativistic viscous hydrodynamics equations. Two different parametrize form of ζ/s(T) was used along with constant η/s. To construct ζ/s in the partonic phase we use lattice data. ζ/s in the hadronic phase is calculated using a hadron resonance gas model including Hagedorn states with limiting mass of

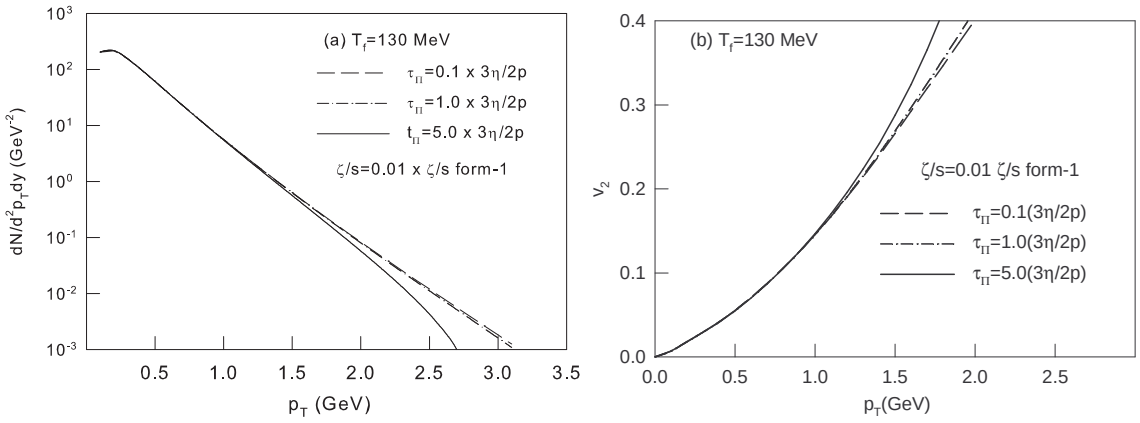

Figure 4.16: Effect of relaxation time on p_T spectra and elliptic flow.

80 GeV.

A comparative study of ideal, shear, and bulk viscous evolution is also done. We observe that the time variation of the temperature of the fluid remains similar for ideal and bulk viscous evolution. However, in the presence of shear viscosity the cooling rate is reduced. Because of the reduced pressure due to bulk viscosity, the transverse velocity slightly decreases compared to the ideal fluid around freezeout time. The shear viscosity on the other hand increases the transverse pressure, which results in a higher transverse velocity compared to the ideal evolution. The observable consequence of the above fact is reflected in the slope of the p_T spectra of pion. The time evolution of spatial eccentricity is almost unchanged in ideal and bulk viscous evolution. Due to the larger transverse velocity in shear viscous evolution, the spatial deformation shows a rapid change compared to the ideal fluid. The momentum anisotropy in the shear viscous evolution grows at a much slower rate compared to the ideal evolution. The change in the time variation of momentum anisotropy in the bulk viscous fluid with respect to ideal case is observed at a late time of the evolution. This will have consequences on

the observed elliptic flow of the hadrons.

The bulk viscous modification of the freezeout distribution function according to Grad's moment method has been considered. The change in p_T spectra and v_2 in bulk viscous evolution with respect to the ideal simulation with no correction to the freezeout distribution is within 5-10% depending on the form of ζ/s(T). However, a large correction to both the p_T spectra and elliptic flow was observed for bulk viscous simulation with dissipative correction to the freezeout distribution function. Combined study of p_T spectra and v_2 of pion in b=7.4 fm Au-Au collision with full bulk viscous evolution puts a constraint on the applicability of Grad's 14-moment methods. We find the relative correction remains within 50% for bulk viscosity to entropy density ratio less than 0.01 times ζ/s form-1. In absence of a reliable method for bulk viscous correction to the freezeout distribution function, we do not include bulk viscosity in 2+1D viscous hydrodynamic simulations while extracting η/s from experimental heavy ion collision data as will be discussed in the next chapter.

Chapter 5

Shear Viscosity at RHIC and LHC

5.1 Introduction

In the previous two chapters we have discussed the effect of shear and bulk viscosity on the fluid evolution and on the charged hadron's p_T spectra and v_2. In this chapter we are going to discuss the application of viscous hydrodynamics simulations to explain the experimental observables and extract the η/s of the fluid produced at top RHIC and LHC energies. In chapter-4 we have mentioned that the bulk viscous correction to the invariant yield of pions is large due to the specific method used to calculate the dissipative correction to the freezeout distribution function. Hence, in this chapter we will only consider the shear viscosity. In the next subsection we will discuss the experimental observables which have been used in our study. This is followed by a very brief discussion on application of relativistic transport model calculations to the heavy

ion data. Finally we will compare our shear viscous hydrodynamic simulation results to the available data at RHIC and LHC.

5.1.1 Experiments at RHIC and LHC

We have considered the experimental measurements of Au-Au $\sqrt{s_{NN}}$=200 GeV collisions at RHIC and Pb-Pb $\sqrt{s_{NN}}$=2.76 TeV collisions at LHC to extract η/s of the QCD matter by using the relativistic viscous hydrodynamics model. Specifically we have taken the data from PHENIX and STAR experiments at RHIC and from ALICE experiment at LHC.

5.1.2 Observables

Charged hadron pseudorapidity density per participating nucleon pair : PHENIX collaboration has measured charged particle multiplicity per participating nucleon pair at midrapidity ($\frac{1}{0.5N_{part}}\frac{dN_{charge}}{d\eta}$) in Au-Au collisions at $\sqrt{s_{NN}}$= 200 GeV as a function of centrality [150]. The experimental finding shows that the number of produced charged hadrons per participating pair decreases by $\sim 35\%$ from central to peripheral collisions (discussed later in figure 5.3). Centrality dependence of $\frac{1}{0.5N_{part}}\frac{dN_{charge}}{d\eta}$ is an important observable to understand the collision dynamics and geometry. In reference [150], a systematic comparison of experimentally measured $\frac{1}{0.5N_{part}}\frac{dN_{charge}}{d\eta}$ as a function of centrality to various theoretical model calculations are given.

In Large Hadron Collider experiment, ALICE collaboration has measured the $\frac{1}{0.5N_{part}}\frac{dN_{charge}}{d\eta}$ at midrapidity for Pb-Pb collision at $\sqrt{s_{NN}}$=2.76 TeV [110]. The trend for the centrality dependence of $\frac{1}{0.5N_{part}}\frac{dN_{charge}}{d\eta}$ is observed to be same as was measured for Au-Au collisions at $\sqrt{s_{NN}}$=200 GeV. However, the number of produced charged hadron is increased by a factor of about 2 in Pb-Pb collisions at $\sqrt{s_{NN}}$=2.76 TeV compared to Au-Au collisions at $\sqrt{s_{NN}}$=200 GeV. Measured value of $dN_{charge}/d\eta$ at midrapidity for 0-5% Au-Au collision at $\sqrt{s_{NN}}$=200 GeV is 687±37 [150]. The corresponding value for Pb-Pb collision at $\sqrt{s_{NN}}$=2.76 TeV is 1601±60 [110].

In our simulation we have used experimentally measured $\frac{1}{0.5N_{part}}\frac{dN_{charge}}{d\eta}$ to fix the x fraction used in the two component Glauber model calculation of initial transverse energy density profile.

Centrality dependence of charged hadron invariant yield : We have compared our viscous hydrodynamics simulation with the experimentally measured charged hadron invariant yield ($dN/d^2p_Td\eta$) as a function of p_T for both Au-Au [151] and Pb-Pb [152] collision at $\sqrt{s_{NN}}$=200 GeV and 2.76 TeV respectively. The slope of the $dN/d^2p_Td\eta$ vs. p_T is related to the effective temperature of the thermalized system at the time of freezeout. The PHENIX measurement of charged hadron $dN/d^2p_Td\eta$ in Au-Au collisions at $\sqrt{s_{NN}}$=200 GeV [151] has been done for p_T range from 0.5-9.5 GeV for $\mid \eta \mid < 0.35$ (η is the pseudorapidity). We will compare our simulation to the experimental data for p_T range 0.5-3.0 GeV and for 0-50% collision centralities. The ALICE measurement of charged hadron $dN/d^2p_Td\eta$ in Pb-Pb collisions at $\sqrt{s_{NN}}$=2.76

TeV [152] has been done for the p_T range 0.3-20 GeV for $\mid \eta \mid < 0.8$ for 0-5% and 70-80% centrality. We will compare viscous hydrodynamics simulation results for $p_T < 3$ GeV, and for 0-5% centrality.

Centrality dependence of charged hadron elliptic flow : It has already been stated that the elliptic flow coefficient (v_2) is one of the important observables measured in high energy heavy-ion collisions at RHIC and LHC. Elliptic flow is defined as $v_2 = \langle cos2(\phi - \Psi) \rangle$, where ϕ is the azimuthal angle of an emitted particle with respect to the x axis, Ψ is the angle between the reaction plane (which contains impact parameter vector and beam direction which is taken along the z axis) to the x axis, and the angular bracket denotes the averaging over particles and events. Elliptic flow, v_2, and other higher harmonics of the flow are treated as a definitive signature of collectivity of the medium (discussed in chapter-2). For our comparative study between the viscous hydrodynamics simulations and experimental data presented in this chapter, we have used the v_2 and v_4 of charged hadrons measured by the PHENIX collaboration [153] for $\sqrt{s_{NN}}$=200 GeV Au-Au collisions. The elliptic flow coefficient v_2 is measured experimentally by various methods like event plane method, two particle correlations, four particle correlations etc. In reference [153], the PHENIX collaboration has used event plane method to measure the charged hadrons v_2, v_3, and v_4 for Au-Au $\sqrt{s_{NN}}$=200 GeV collisions. The main difficulty to measure v_2 or any other higher order flow harmonics in experiment is due to the uncertainty in the estimation of the reaction plane angle Ψ, which is not a direct experimental observable. The PHENIX collaboration has used three different detector system (a) Beam Beam Counter (BBC), (b) reaction

plane detector (RXN) of BBC, and (c) Muon-Piston Calorimeter (MPC) to estimate the event plane angle. The BBC detector was used to estimate the centrality of the collisions, RXN and MPC were used to estimate the reaction plane angle (Ψ) for a particular event. The event plane measurement detectors and flow measurement detector are separated by 2-3 unit of rapidity which helps to reduce the effect of non-flow in the measurement. The pad and drift chamber were used to reconstruct the momentum and azimuthal distribution of the produced particles at mid-rapidity with azimuthal angle coverage of $\phi = \pi$ radian. The experimental data shows that v_2 increases with p_T for a particular centrality collision and it increases in the semi peripheral collisions compared to the central collisions (the PHENIX estimation of v_2 for Au-Au $\sqrt{s_{NN}}$=200 GeV collisions are shown later in figure 5.5). Experimentally measured v_4 by the PHENIX collaboration [153] shows similar behavior (as discussed later in figure 5.7). The p_T integrated elliptic flow data was taken from STAR experiment [161]. Where the time projection chamber detector was used to measure v_2 in the pseudo rapidity range $\mid \eta \mid <$ 1.0.

We have also compared our viscous hydrodynamics simulation to the experimentally measured v_2 at LHC for Pb-Pb $\sqrt{s_{NN}}$=2.76 TeV collision. The experimental measurement of v_2 was done by the central detectors of the ALICE experiment [154] for 10-50% collision centrality at midrapidity by using 4 particle correlation method. The 4 particle correlation method does not need the information about the event plane angle. The experimental finding shows that the measured value of v_2 as a function of p_T for the 10-50% Pb-Pb $\sqrt{s_{NN}}$=2.76 TeV collision is similar in magnitude to that of the v_2 measured for Au-Au $\sqrt{s_{NN}}$=200 GeV collision. However, a more flatter p_T spectra at

LHC compared to RHIC, results in a increase in the p_T integrated elliptic flow value by about 30% at LHC compared to RHIC.

5.1.3 Theoretical models

The space-time evolution of the matter produced in high energy heavy-ion collisions can be described by using either a relativistic viscous hydrodynamic model or a relativistic transport model simulation like A Multi Phase Transport model (AMPT) [21] and Ultra Relativistic Quantum Molecular Dynamics (URQMD) [22] etc. For physically reasonable values of initial parameter set, both the hydrodynamics and transport model gives satisfactory description of various experimental observables. One can also estimate the values of transport coefficients of the QCD matter by using these dynamical models. One of the two model, relativistic viscous hydrodynamics is the main topic of this dissertation and the detail comparison of viscous hydrodynamic simulation result to the experimental observables measured at RHIC and LHC will be presented in the subsequent sections. Like all the other models, relativistic viscous hydrodynamics has its own limitation. For example, it is known from kinetic theory calculations [131, 155, 156] that the value of specific shear viscosity (η/s) is quite large in the hadronic phase. In a relativistic viscous hydrodynamics model, a large value of shear or bulk viscosity introduce a large dissipative correction to the energy-momentum tensor. This large dissipative correction to the $T^{\mu\nu}$ ultimately leads to the breakdown of the assumption of near local thermal equilibrium and the viscous hydrodynamics will no longer be a valid model without that assumption. On the other hand, transport models does not

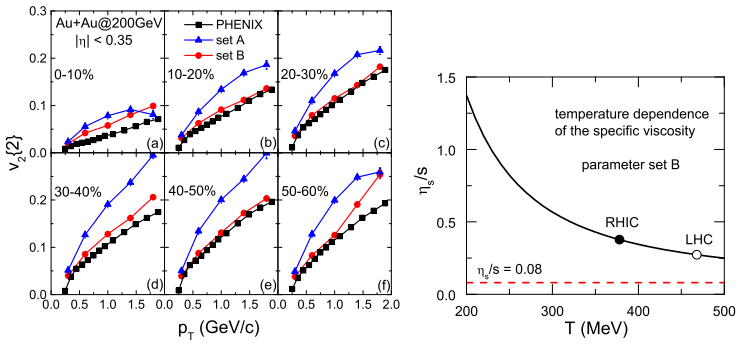

Figure 5.1: Left Panel : Transverse momentum dependence of charged hadron elliptic flow at midrapidity. The experimental data for Au-Au $\sqrt{s_{NN}}$=200 GeV collision measured by the PHENIX collaboration are shown by filled square [158]. The simulated v_2 from AMPT for two different sets of parameter are shown by red circles and blue triangles. Right Panel : Temperature dependence of specific shear viscosity (η_s/s) in the partonic matter calculated in [157]. A specific set of parameter was used for the calculation.

rely upon the assumption of near local thermal equilibrium and will work for a non-equilibrated system. In the following we will discuss a few results obtained from a transport model calculation AMPT. The details of the model and the parameters used for the study can be found in reference [157].

Transport model : The left panel of figure 5.1 compares the simulated results of elliptic flow v_2 obtained from the AMPT model calculation [157] with the experimental data for Au-Au $\sqrt{s_{NN}}$=200 GeV collision [158]. The v_2 calculation from AMPT model for Au-Au collision at RHIC has been done for two set of input parameters (shown by red and blue lines in the left panel of figure 5.1). The details of selecting the values of parameters can be found in the original work by Xu et. al [157]. Reasonable agreement between the data and transport simulation is observed.

In reference [157], the specific shear viscosity (η/s) of the quark gluon plasma produced in heavy ion collision at RHIC and LHC was also estimated. The calculated values of η/s as a function of temperature is shown in the right panel of figure 5.1. We will discuss about the formula used to estimate η/s in such a transport approach [157] in a later paragraph of this chapter.

With this brief discussion on transport model calculation in heavy-ion collision, now we present our study of the application of relativistic viscous hydrodynamics in heavy-ion collision. In the following sections we will compare viscous hydrodynamics simulation to various experimental observables measured at RHIC and LHC and will try to estimate the approximate value of η/s.

5.2 η/s at RHIC

5.2.1 Input to viscous hydrodynamics

We have already discussed about the inputs necessary for 2+1D viscous hydrodynamics simulation in chapters 2 and 3. These inputs are free parameter in a viscous hydrodynamics simulation and their values are adjusted to explain the experimental data. In the following we have written the values of the input parameters used in our simulation for Au-Au $\sqrt{s_{NN}}$=200 GeV collision.

- **Initial time :** 0.6 fm,

- **Initial energy density profile :** $\varepsilon(\mathbf{b}, x, y) = \varepsilon_0[(1-x)\frac{N_{part}(\mathbf{b},x,y)}{2} + xN_{coll}(\mathbf{b}, x, y)]$,
- **Fraction of hard scattering :** x=0.9,
- **Initial energy density and temperature :** See table 5.1.

Table 5.1: ε_0 and T_i values for various η/s.

η/s	0	0.08	0.12	0.16	0.18
ε_0 (GeV/fm^3)	43.4 ± 3.5	36.5 ± 2.5	32.5 ± 2.2	27.7 ± 2.0	25.4 ± 2.0
T_i (MeV)	410 ± 7	392 ± 7	382 ± 6	367 ± 6	360 ± 6

- **Initial transverse velocity :** $v_x(x, y) = v_y(x, y) = 0$,
- **Initial shear stresses :**$\pi^{xx} = \pi^{yy} = 2\eta/3\tau_0$, π^{xy}=0,
- **Relaxation time for shear stress :** $\tau_\pi = 3\eta/2p$
- **Freezeout temperature :** $T_{fo} = 130$ MeV.

In figure 5.2 we show the estimate of the initial central energy density ε_0 for various values of η/s. This is done by matching the experimentally measured charged hadron multiplicity-density at midrapidity for 0-5% Au-Au collision at $\sqrt{s_{NN}} = 200$ GeV measured by the PHENIX collaboration [150]. Their values along with the uncertainty and the corresponding initial temperature are given in table 5.1. The uncertainties are due to the errors associated with the experimental measurement of charged hadron multiplicity density which is shown as a red shaded band in figure 5.2. Viscous fluid evolution is associated with entropy generation, to produce a fixed multiplicity, lower value of ε_0 is required compared to the ideal fluid.

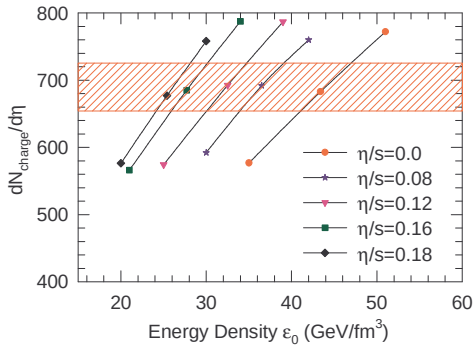

Figure 5.2: The experimental measurement of charged hadron multiplicity-density at midrapidity (687 ± 37) for 0-5% Au-Au collision at $\sqrt{s_{NN}} = 200$ GeV by the PHENIX collaboration [150] is shown by the red shaded region with the corresponding error. Charged hadron multiplicity obtained from ideal and viscous hydrodynamics simulation for varying ε_0 are shown by the lines and symbols.

5.2.2 Results

With all the model parameters fixed we present below a study of the centrality dependence of simulated charged particles multiplicity, p_T spectra, v_2, and v_4 in $\sqrt{s}_{NN}$=200 GeV Au-Au collisions.

Charged hadron multiplicity per participant pair : In the left panel of figure 5.3 shows the simulated $(\frac{1}{0.5N_{part}}\frac{dN_{ch}}{d\eta})$ results for ideal fluid (curves) with different x fraction compared with the corresponding PHENIX measurements (open circles)[150]. In all the simulations, the central energy density ε_0 is fixed to reproduce the experimental multiplicity of charged hadron in central (0-5%) collision. We find that the simulations with x fraction of 0.9 reproduces the experimental measured charged particle-density as a function of number of participating nucleons. The ideal hydrodynamics simulation

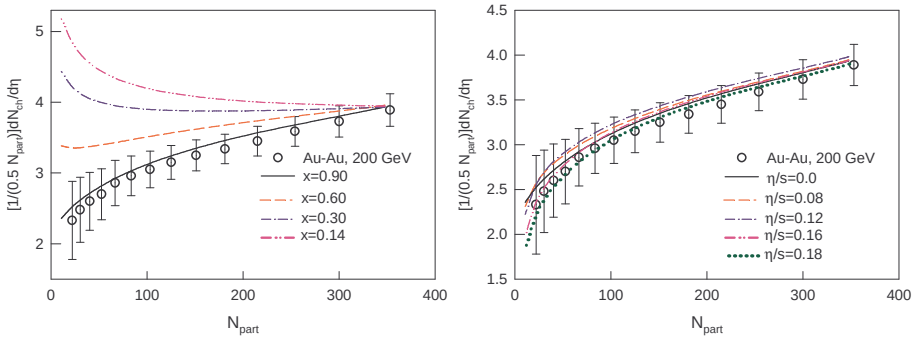

Figure 5.3: Left panel : PHENIX measurements for the centrality dependence of charged particles multiplicity per participating nucleon pair (open circles) [150] are compared with ideal hydrodynamical simulations for hard scattering fraction (x) 0.14 (pink dash dot-dot), 0.3 (blue dash dot), 0.6 (red dashed), and 0.9 (solid black). Right panel : Same as left panel but for x fraction 0.9 and η/s=0 (black solid curve), 0.08 (red dashed curve), 0.12 (blue dash dotted curve), 0.16 (pink dash-dot-dot curve), and 0.18 (green dotted curve).

with $x < 0.9$ overpredict the experimental data for peripheral collisions. There is an alternate procedure for initializing the energy density. In such an approach the initial entropy density profile is parametrized using a two component model as discussed in [159, 160] from which the initial energy density profile is obtained. In such an entropy density parametrization the optimum value of the x fraction is ~ 0.1. In subsequent results we have used the value of x fraction equals to 0.9, which best describe the centrality dependence of charged hadron pseudorapidity density at midrapidity (as seen in figure 5.3).

The right panel of figure 5.3 shows the comparison of experimentally measured $\frac{1}{0.5N_{part}}\frac{dN_{ch}}{d\eta}$ to the ideal (black solid curve) and viscous hydrodynamics simulation with η/s= 0.08 (red dashed curve), 0.12 (blue dash dotted curve), 0.16 (pink dash-dot-dot curve), and 0.18 (green dotted curve) for x=0.9. The simulations are carried out by fix-

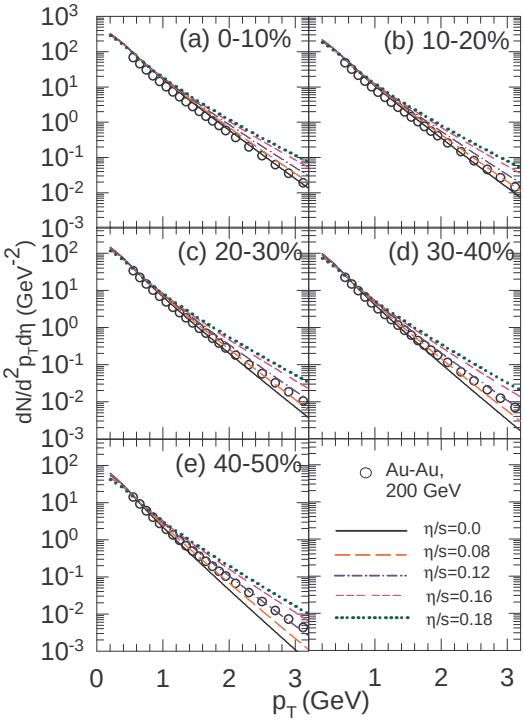

Figure 5.4: PHENIX measurements for charged particles p_T distribution in 0-50% Au-Au collisions (open circles) [151] are compared with hydrodynamic simulations (different lines) for η/s=0-0.18 (bottom to top).

ing the value of ϵ_0 to reproduce the value of the measured charged particle multiplicity-density for 0-5% Au-Au collision at $\sqrt{s_{NN}}$ = 200 GeV. The centrality dependence of the result indicates that within the experimental errors associated with the charged particle multiplicity density, this observable is not very sensitive to the various input values of η/s.

Centrality dependence of charged particles p_T spectra : PHENIX measurements for charged particles p_T spectra in 0-10%, 10-20%, 20-30%, 30-40%, and 40-50% centrality collisions at mid-rapidity (open circles) [151] are compared with hydrodynam-

ical simulations (curves) in figure 5.4. The viscous hydrodynamic simulation has been carried out for five different η/s=0 (black solid), 0.08 (red dashed), 0.12 (dash dotted), 0.16 (dash-dash-dash), and 0.18 (green dotted curve). As discussed in chapter-3, the shear viscosity increases the transverse velocity (v_T) of the fluid and hence makes the p_T spectra flatter. This effect of shear viscosity on spectra is evident in figure 5.4. Compared to the ideal fluid, in viscous evolution, high p_T production of charged hadrons is enhanced. In order to get a quantitative estimate of the matching between the experimental data and the hydrodynamic simulation we have carried out a χ^2 analysis. The χ^2 per degrees of freedom is defined as

$$\frac{\chi^2}{N} = \frac{1}{N}\sum_{i=1}^{N}\left[\frac{TH(i) - EX(i)}{E(i)}\right]^2, \tag{5.1}$$

where $TH(i)$ is the theoretical estimates, $EX(i)$and $E(i)$ are corresponding experimental measurement and related errors, and N is the number of experimental data points. In table 5.2, χ^2 values are listed. From the comparison of experimentally measured p_T spectra for centrality 0-50% with viscous hydrodynamics simulation we can conclude that PHENIX data on charged particles p_T spectra in 0-10% collisions do not demand any viscosity. Whereas for other centralities the experimental data is well reproduced with a small ($\sim$ 0.08-0.12) value of η/s.

Centrality dependence of charged hadron elliptic flow : The viscous hydrodynamics simulations (curves) along with the experimentally measured centrality dependence of charged hadron elliptic flow (open boxes) as a function of p_T for Au-Au collision

Table 5.2: χ^2/N values for the fit to the PHENIX data for different values of viscosity to entropy ratio.

	χ^2/N				
Data set	$\eta/s = 0.0$	η/s=0.08	η/s=0.12	η/s=0.16	η/s=0.18
charged particles multiplicity	0.14	0.29	0.44	0.15	**0.05**
spectra: 0-10%	**11.97**	22.34	41.81	77.75	107.2
spectra: 10-20%	**4.70**	11.0	27.30	63.30	95.0
spectra: 20-30%	**2.95**	5.10	19.90	62.50	102.5
spectra: 30-40%	5.40	**2.70**	14.50	59.60	105.0
spectra: 40-50%	14.20	**3.50**	6.40	44.70	84.90
v_2 integrated	7.91	**6.87**	7.30	8.08	8.93
v_2: 0-10%	**1.52**	13.48	24.30	34.45	38.36
v_2: 10-20%	80.29	10.17	**0.23**	5.19	12.49
v_2: 20-30%	165.51	30.56	**2.67**	2.75	6.40
v_2: 30-40%	111.25	11.87	**1.00**	6.10	11.03
v_2: 40-50%	184.10	39.69	12.23	5.89	**3.53**

at $\sqrt{s_{NN}}$= 200 GeV [153] are shown in five panels of the figure 5.5. Like the p_T spectra, charged hadron v_2 do not demands any viscosity in most central (0-10%) collision. It is also evident from the χ^2 value as shown in table 5.2 . As already discussed in chapter-3, the momentum anisotropy (ϵ_p) decreases in shear viscous evolution compared to ideal fluid and hence v_2 decreases with increasing value of η/s. This trend is observed in the simulations shown in figure 5.5. From the comparison between experimental data and viscous hydrodynamic simulations we observe that in peripheral collisions the fluid is more viscous (with a higher value of η/s) than in central collisions. In summary, charged hadron v_2 data in 0-10% is best explained by simulations with η/s=0, 10-20% for η/s=0.12 and the higher centralities for η/s around 0.16.

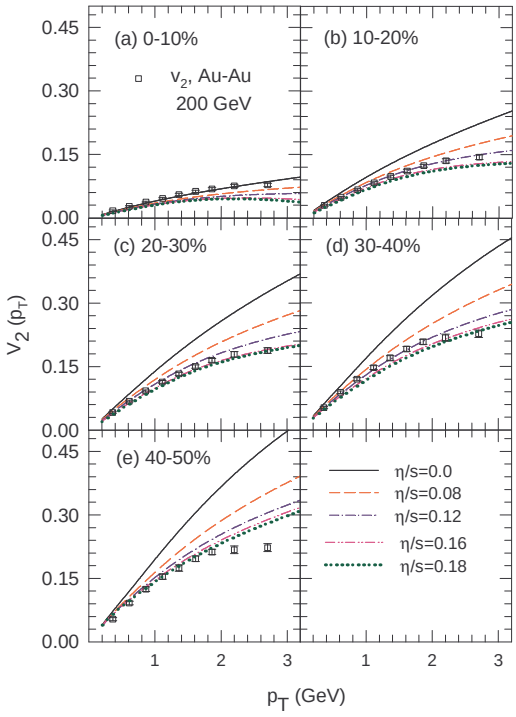

Figure 5.5: In five panels, PHENIX measurements for charged particles elliptic flow in 0-10%, 10-20%, 20-30%, 30-40% and 40-50% for Au-Au collisions at $\sqrt{s_{NN}}$=200 GeV are shown by the open boxes [153]. The solid, short dashed, dashed dotted and long dashed lines are hydrodynamic model simulation for elliptic flow for fluid viscosity η/s=0 (black solid curve), 0.08 (red dashed curve), 0.12 (blue dash dotted curve), 0.16 (pink dash-dot-dot curve), and 0.18 (green dotted curve) respectively.

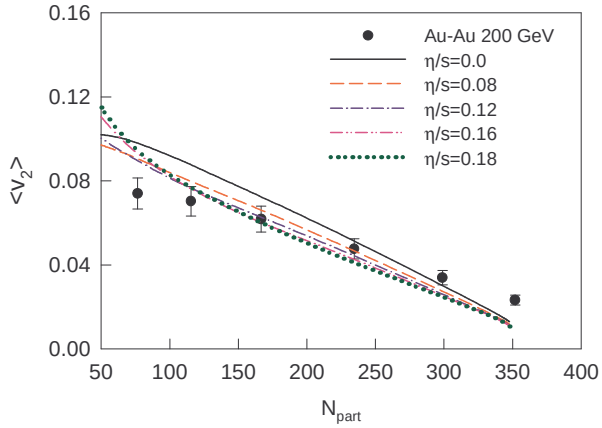

Figure 5.6: The p_T integrated elliptic flow at midrapidity as a function of N_{part} measured by STAR collaboration [161] for $\sqrt{s_{NN}}$=200 GeV Au-Au collision are shown by solid circles. The hydrodynamical simulation for η/s=0 (black solid curve), 0.08 (red dashed curve), 0.12 (blue dash dotted curve), 0.16 (pink dash-dot-dot curve), and 0.18 (green dotted curve) are also shown.

Centrality dependence of charged hadron integrated elliptic flow : Figure 5.6 shows the p_T integrated v_2 measured by the STAR collaboration [161] for $\sqrt{s_{NN}}$ = 200 GeV Au-Au collision at midrapidity as a function of number of participating nucleons. Our viscous hydrodynamics simulation results for different values of η/s are also shown. The solid black line is the simulated result for ideal fluid (η/s=0), the results for η/s = 0.08, 0.12, 0.16, and 0.18 are shown as red dashed curve, blue dash dotted curve , pink dash-dot-dot, and green dotted curves respectively. We find that our simulations explain the data for mid-central collisions (0-10% to 30-40%). For 0-5% central collision the simulation results are lower than the experimental data. This difference between simulation and data could be understood by considering different initial conditions such as (a) transverse energy density profile based on Color Glass Condensate (CGC) or (b) a fluctuating initial condition by using event by event hydrodynamics. Results with CGC initial conditions are discussed in appendix C. For 40-50% collision, the simulated

results are higher compared to the experimental data. This indicates that the higher value of η/s is needed to explain the data. However, simulation with higher values of η/s within the current simulation framework is difficult to carry out because of large viscous correction to the equilibrium energy momentum tensor.

Centrality dependence of charged hadron v_4 : The flow associated with the fourth harmonic (v_4) of the Fourier expansion of the azimuthal angle (ϕ) distribution of produced particles with respect to reaction plane angle (Ψ) is defined as $\langle cos4(\phi - \Psi)\rangle$. The open boxes in 5.7 are the experimental measurements for v_4 in $\sqrt{s_{NN}}$ = 200 GeV Au-Au collision [153].

The corresponding hydrodynamics simulations are shown by curves for η/s=0 (solid black), 0.08 (red dashed), and 0.12 (dash dotted). Like v_2 the values of v_4 also decreases with increase in η/s. The experimental v_4 data for 0-10% , 10-20%, and 20-30% centralities are underestimated in ideal fluid simulations. v_4 for 30-40% and 40-50% centralities agrees with the ideal hydrodynamics simulation. This observation is in sharp contrast to what we have seen above for the case of elliptic flow in figure 5.5. In order to understand the v_4 results, it is important to investigate in future the role of initial conditions in viscous hydrodynamics simulation. The results with a CGC based initial conditions for the viscous hydrodynamics simulations are discussed in appendix C. These observations also emphasizes the need to experimentally measure the higher harmonics of flow for charged hadrons.

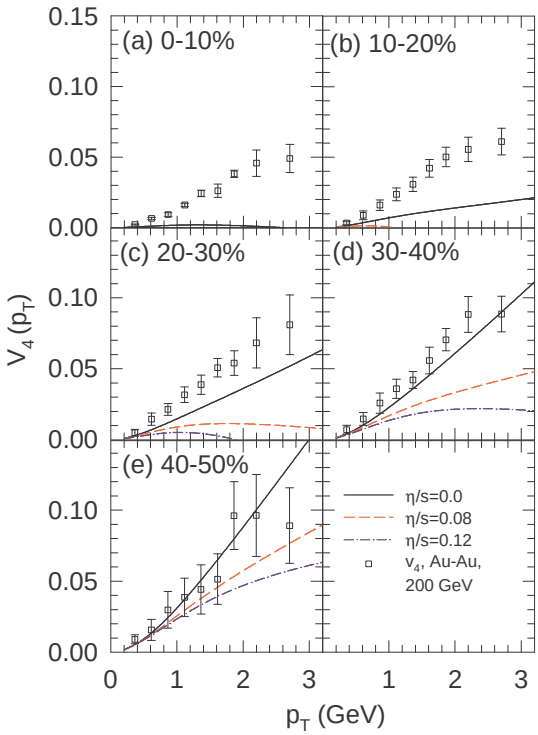

Figure 5.7: The open boxes are PHENIX measurements for charged particles v_4 in 0-10%, 10-20%, 20-30%, 30-40%, and 40-50% Au-Au collisions at $\sqrt{s_{NN}}$=200 GeV [153]. The solid, dashed, and dashed dotted lines are hydrodynamic model simulation for v_4 for fluid viscosity η/s=0 (black solid curve), 0.08 (red dashed curve), and 0.12 (blue dash dotted curve) respectively.

5.2.3 Comparison to other estimates of η/s

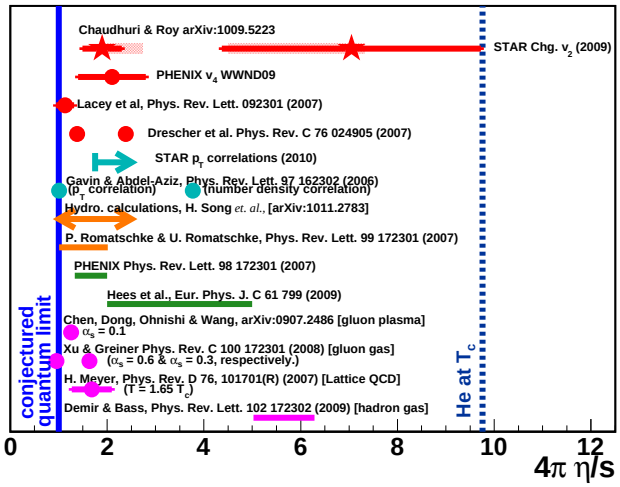

Figure 5.8: Extracted values of η/s for Au-Au collision at $\sqrt{s_{NN}} = 200$ GeV by different model calculations using different experimental observables. The solid vertical line at the left shows the lower limit of η/s in unit of $1/(4\pi)$ [68]. For comparison we have also shown the η/s of He at T_c (blue dashed line).

The figure 5.8 shows the extracted values of η/s in different model calculations for Au-Au collisions at $\sqrt{s_{NN}}$=200 GeV. Most of the estimates are obtained by comparing experimental data for elliptic flow with model calculations. Some of the estimates used p_T correlations and heavy meson v_2 data. The theoretical calculations include simulations with transport based approach as well as 2+1D and 3+1D viscous hydrodynamics with various initials conditions. Also shown are the results from lattice QCD calculation. Our estimate of η/s based on the results discussed in the previous paragraphs are shown on the top row of figure 5.8 as red star. All these results indicates that the η/s value of the QGP fluid produced at top RHIC energies lies within 1-5 $\times 1/4\pi$ and is below the η/s value of helium (blue dashed line) at T_c. The spread in the estimated values of η/s reflects the current uncertainties associated with the theoretical calculations.

5.3 η/s at LHC

In this section we will discuss the comparison between the experimental data for Pb-Pb $\sqrt{s_{NN}}$=2.76 TeV collision at mid-rapidity to the viscous hydrodynamics simulations. The centrality dependence of charged particle pseudorapidity density, p_T spectra (0-5%), average v_2, and v_2 vs. p_T are used to extract η/s.

5.3.1 Input to viscous hydrodynamics

We have discussed the inputs necessary for 2+1D viscous hydrodynamics simulation several times. Here we will only mention their values appropriate for Pb-Pb $\sqrt{s_{NN}}$=2.76 TeV collision.

- **Initial time :** 0.6 fm,
- **Initial energy density profile :** $\varepsilon(\mathbf{b}, x, y) = \varepsilon_0[(1-x)N_{part}(\mathbf{b}, x, y)+xN_{coll}(\mathbf{b}, x, y)]$,
- **Fraction of hard scattering :** x=0.9,
- **Initial energy density and temperature :** See table 5.3.
- **Initial transverse velocity :** $v_x(x, y) = v_y(x, y) = 0$,
- **Initial shear stresses :**$\pi^{xx} = \pi^{yy} = 2\eta/3\tau_0$, π^{xy}=0,
- **Relaxation time for shear stress :** $\tau_\pi = 3\eta/2p$

Table 5.3: ε_0 and T_i values for various η/s.

η/s	0	0.08	0.12	0.16
ε_0 (GeV/fm^3)	153.0 ± 6.0	135.0 ± 5.5	123.8 ± 5.2	111.3 ± 4.6
T_i (MeV)	557 ± 5	541 ± 6	530 ± 5	516 ± 4

- **Freezeout temperature :** $T_{fo} = 130$ MeV.

In figure 5.9 we show the estimate of the initial central energy density ε_0 for various η/s so as to match the experimentally measured charged hadron multiplicity-density at midrapidity for 0-5% Pb-Pb collision at $\sqrt{s_{NN}} = 2.76$ TeV measured by the ALICE collaboration [110]. Their values along with the uncertainties and the corresponding initial temperatures are given in table 5.3. The uncertainties are due to the errors associated with the experimental measurement of charged hadron multiplicity density which is shown as a red shaded band in figure 5.9. Viscous fluid evolution is associated with entropy generation, to produce a fixed multiplicity, lower values of ε_0 are required compared to the ideal fluid. The initial temperature achieved in central Pb-Pb collision at LHC is about 1.6 times larger than at RHIC.

5.3.2 Results

With all the model parameters fixed we can study the centrality dependence of simulated charged particles multiplicity, p_T spectra, and v_2 in $\sqrt{s}_{NN}$=2.76 TeV Pb-Pb collisions.

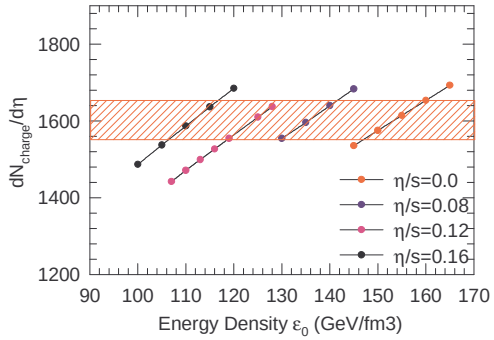

Figure 5.9: The experimental measurement of charged hadron multiplicity-density at midrapidity for 0-5% Pb-Pb collision at $\sqrt{s_{NN}} = 2.76$ TeV by the ALICE collaboration is shown by red shaded region with the corresponding error [110]. Charged hadron multiplicity obtained from ideal and viscous hydrodynamics simulation for varying ε_0 are shown by the lines and symbols.

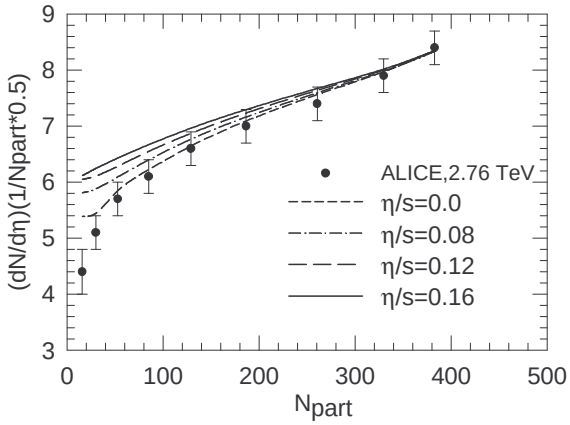

Figure 5.10: ALICE measurements for centrality dependence of charged particles multiplicity per participating nucleon pair (solid circles) [110] are compared with hydrodynamical simulations for η/s=0 (small dashed), 0.08 (dash dotted), 0.12 (long dashed), and 0.16 (solid curve).

Charged hadron multiplicity per participant pair : In figure 5.10 simulation results (curves) for charged particles multiplicity per participant pairs are compared with the ALICE measurements (solid circles)[110]. Even though, fluid was initialized to reproduce experimental multiplicity in 0-5% collisions, in peripheral collisions, viscous fluid produces more particles than an ideal fluid. The reason is understood. Viscous effects depend on the velocity gradients. Velocity gradients are more in a peripheral collisions than in a central collisions, so is the viscous effect. To be quantitative about the fit to the data in ideal and viscous hydrodynamics, we have computed χ^2 values for the fits, they are listed in table 5.4. Best fit to the data is obtained in the ideal fluid approximation. The results with viscous evolution gives a higher (a factor of 2-5) χ^2 value. We can conclude that ALICE charged particle multiplicity data in $\sqrt{s}_{NN}$=2.76 TeV Pb-Pb collisions do not demand any viscosity.

Charged particle p_T spectra in 0-5% collision : ALICE measurements for charged particles p_T spectra in 0-5% collisions at mid-rapidity (solid circles) [152] are compared with hydrodynamical simulations (curves) in figure 5.11. We have initialized the fluid to reproduce p_T integrated charged particles multiplicity in 0-5% collision. Such an initialisation do reproduces experimental p_T spectra reasonably well. Effect of viscosity on spectra is also evident. Compared to the ideal fluid, in viscous evolution, high p_T production is enhanced. In table 5.4, χ^2 values for the fits are listed. Charged particle p_T spectra in 0-5% collision is equally well explained in ideal (χ^2/N= 10.26) and viscous (η/s=0.08) fluid (χ^2/N= 10.58) evolution. We can conclude that ALICE data on charged particles p_T spectra in 0-5% collisions, demand the fluid viscosity with range

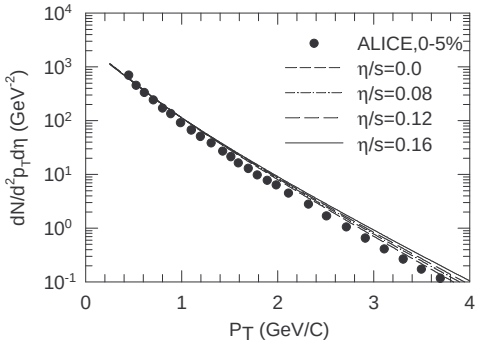

Figure 5.11: The solid circles are the ALICE measurements for charged particles p_T distribution in 0-5% Pb-Pb collisions [152]. The lines are hydrodynamic simulations for η/s=0-0.16 (bottom to top).

η/s=0-0.08.

Centrality dependence of differential elliptic flow : ALICE collaboration employed various methods, e.g. 2 and 4 particle cumulant, q-distribution, Lee-Yang zero method etc, to measure charged particles elliptic flow in Pb-Pb collisions [154]. Flow in 4-particle cumulant method, Lee-Yang zero method and q-distribution is consistent with each other. 2-particle cumulant method however results in ∼15% higher flow. In figure 5.12, ALICE measurements for elliptic flow $v_2\{4\}$, in 4-particle cumulant method, in 10-20% ,20-30%, 30-40%, and 40-50% collision centralities are shown (the solid circles) [154]. ALICE collaboration measured elliptic flow upto $p_T \approx 5$ GeV. In figure 5.12, we have shown the measurements only upto p_T=3 GeV. Hydrodynamical model are not well suited for large p_T. Sources other than thermal also contribute to the particle production at large p_T. The continuous, small dashed, dashed dot, and medium dashed lines in figure 5.12 are simulated elliptic flow for pions in hydrodynamic evolution of fluid with viscosity to entropy density ratio η/s=0.0, 0.08, 0.12, and 0.16 respectively.

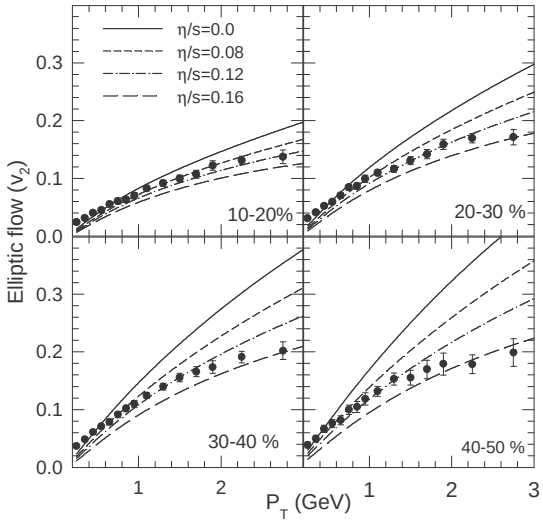

Figure 5.12: In four panels, ALICE measurements for charged particles elliptic flow in 10-20%, 20-30%, 30-40%, and 40-50% Pb-Pb collisions are shown by solid circles [154]. The solid, short dashed, dashed dotted and long dashed lines are hydrodynamic model simulation for elliptic flow for fluid viscosity η/s=0, 0.08, 0.12, and 0.16 respectively.

As expected with increasing η/s the $v_2(p_T)$ decreases. We observe that for peripheral collisions experimental data need more viscous fluid than in central collisions.

Centrality dependence of integrated elliptic flow : In figure 5.13 ALICE measurements for integrated elliptic flow in 4-particle cumulant method are compared with hydrodynamical simulations for elliptic flow. Elliptic flow depend sensitively on viscosity, flow reducing with increasing viscosity. Reduction is more in peripheral than in central collisions. As argued previously, viscous effects are more in peripheral than in central collisions. For viscosity, η/s=0.16, in very peripheral collisions, experimental centrality dependence is not reproduced, data are under predicted. χ^2/N values for the fits to the data are noted in table 5.4. Unlike the centrality dependence of charged particles multiplicity or p_T spectra (0-5%), best fit to the ALICE data on integrated

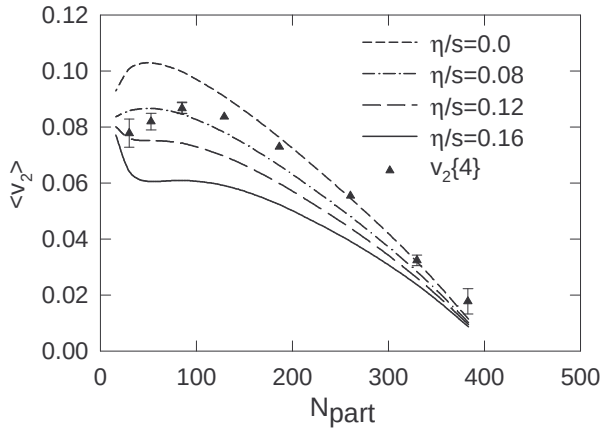

Figure 5.13: The p_T integrated elliptic flow at midrapidity as a function of N_{part}, measured by the ALICE collaboration for $\sqrt{s_{NN}}$=2.76 TeV Pb-Pb collision are shown by solid triangles [154]. The hydrodynamics simulation for η/s=0 (small dashed curve), 0.08 (dash dotted curve), 0.12 (long dashed curve), and 0.16 (solid black curve), are also shown.

elliptic flow is obtained for η/s=0.08.

Discussion : In the present analysis we have used some specific initial conditions, e.g. initial time τ_0=0.6 fm, initial fluid velocity $v_T = 0$, hard scattering fraction $x = 0.9$, boost-invariant shear stress tensor etc. All possible initial conditions are not explored. The systematic uncertainty in η/s due to various uncertainties in the initial conditions was estimated as large as 175% [124]. A combined χ^2 analysis of the simulated results for various η/s and the experimental data on the charged particle multiplicity, p_T spectra (0-5% centrality), $v_2(p_T)$ vs. p_T (10-50% centrality), and integrated v_2 are shown in figure 5.14 (solid circles). Parabolic fit (solid curve) to the combined χ^2/N versus η/s gives the minimum at η/s=0.08 with the corresponding error ±0.02. The presently extracted value of $\eta/s = 0.08 \pm 0.02$ from the experimental data will be even more uncertain, if all possible initial conditions are accounted for.

Table 5.4: χ^2/N values for the fit to the ALICE data for different values of viscosity to entropy ratio.

	χ^2/N			
Data set	$\eta/s = 0.0$	η/s=0.08	η/s=0.12	η/s=0.16
charged particles multiplicity	**0.93**	2.57	4.07	5.11
0-5% p_T spectra	**10.26**	10.58	18.87	25.57
v_2 integrated	14.71	**2.06**	8.88	35.53
v_2: 10-20%	6.72	**4.72**	7.75	15.24
v_2: 20-30%	22.57	**8.24**	8.79	19.20
v_2: 30-40%	42.68	13.09	**10.32**	24.77
v_2: 40-50%	32.69	9.63	**4.30**	9.15

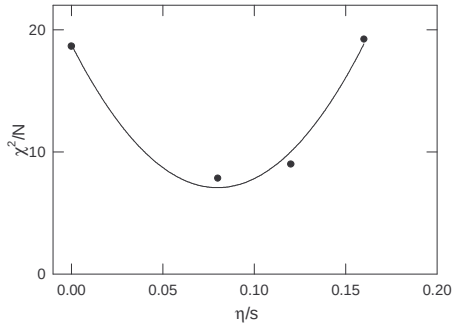

Figure 5.14: χ^2/N values for the fits to the ALICE combined data set (see text). The solid line is a parabolic fit to the χ^2 values.

5.3.3 Comparison to other estimates of η/s

χ^2 analysis of all the combined data discussed above (figure 5.14) shows that the shear viscosity to entropy density ratio is very close to the string theoretical prediction of the lower limit of η/s. Our estimated η/s is compared to other model calculations in figure 5.15. All the model calculations indicates that the values of η/s of the QCD matter formed in heavy-ion collision at LHC lies between 1-4$\times(1/4\pi)$. The specific shear viscosity was obtained in reference [157] by using A Multi Phase Transport model (AMPT). They explain the experimentally measured charged particle pseudorapidity density per participating nucleon pair, elliptic flow ($v_2(p_T)$) in 40-50% centrality, and the centrality dependence of v_2 for Pb-Pb collision at $\sqrt{s_{NN}} = 2.76$ TeV. The model parameters that describe the ALICE data are initial temperature T=468 MeV, and parton-parton cross section of 1.5 mb (the corresponding value of strong coupling constant α_s= 0.47 and screening mass $\mu = 1.8fm^{-1}$). Considering only up and down quarks the shear viscosity to entropy density ratio was calculated by the following formula

$$\eta/s \approx \frac{3\pi}{40\alpha_s^2} \frac{1}{\left(9+\frac{\mu^2}{T^2}\right) ln\left(\frac{18+\frac{\mu^2}{T^2}}{\frac{\mu^2}{T^2}}\right) - 18}. \tag{5.2}$$

The estimated η/s for LHC energy was calculated to be 0.273 (shown in figure 5.15).

Bozek [162] has estimated the specific shear viscosity of the fluid for LHC energy by using a 2+1D viscous hydrodynamics model. The initial parameters used in his calculation are similar to that used by the present author except (a) entropy density was initialized with hard scattering fraction $x \sim 0.15$. In addition to shear viscosity, bulk viscosity (ζ/s=0.04) in the hadronic phase was considered. Freezeout and resonance

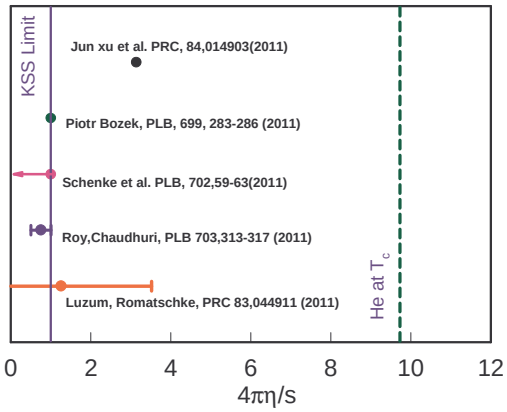

Figure 5.15: Extracted values of η/s for Pb-Pb collision at $\sqrt{s_{NN}}$ = 2.76 TeV by different model calculations. The solid vertical line at the left shows the lower limit of η/s in unit of $1/(4\pi)$ [68]. For comparison we have also shown the η/s of He at T_c (green dashed line).

decay was based on THERMINATOR event generator [163]. Experimental data are best fitted with $\eta/s \sim 0.08$.

A 3+1D viscous hydrodynamics calculation with fluctuating initial conditions was done by Schenke et. al in reference [164]. They explain the $v_2(p_T)$ and p_T integrated v_2 for different centralities. Their calculation shows that the experimental data measured at LHC by the ALICE collaboration are best described for η/s value 0.08 or smaller. Luzum et al. [78] have estimated η/s by using a 2+1D viscous hydrodynamics simulation with smooth initial conditions for LHC energy to be same as at RHIC, η/s=0.1$\pm$ 0.1 (theory) $\pm$ 0.08 (experiment).

Chapter 6

Summary and Outlook

The transport coefficients of the QCD matter are important physical quantities of interest. One way to estimate the transport coefficients of the QCD matter is to do a non-perturbative QCD calculation on lattice [70, 71, 127]. However, current calculations on lattice have large uncertainties. The alternate approach is to compare results from the model calculation, e.g. second order viscous hydrodynamics, to those measured in the experiments involving high energy heavy ion collision. This is because the collisions at the Relativistic Heavy-Ion Collider (RHIC) and the Large Hadron Collider (LHC) have confirmed the formation of a deconfined state of quarks and gluons called the quark-gluon-plasma (QGP) [5, 41, 122]. The data from these experiments thus provide an unique opportunity to extract the transport coefficients of the QGP state.

This later approach forms the major part of this thesis work. Our studies presented here have concentrated on extracting the shear viscosity to entropy density ratio (η/s)

at RHIC and LHC energies. The value of η/s of the QGP is found to lie between 1-4 times the KSS bound [68] and is consistent with similar calculations done by other groups [76, 78, 165, 166, 167, 168, 169, 170, 171, 172, 157, 162, 164]. Towards achieving this goal of extracting η/s of the QCD matter, several steps were undertaken, we discuss these briefly below.

Development of 2+1D viscous hydrodynamics numerical code : For the simulation results presented in this thesis we have used the 2+1D viscous hydrodynamics code "'AZHYDRO-KOLKATA"' [83, 84]. It is based on the second order Israel-Stewart theory of causal viscous hydrodynamics, which solves the energy-momentum conservation equation, and relaxation equations for shear and bulk viscosity by assuming longitudinal boost invariance. Numerical solution of these equations are done with the help of a multi dimensional flux corrected transport algorithm called Smoothed And Sharp Transport Algorithm (SHASTA). Details of the numerical set up are discussed in chapter-2. The major contribution of this thesis work towards the development of the viscous hydrodynamics code "'AZHYDRO-KOLKATA"' is through the implementation of bulk viscosity to both energy-momentum and relaxation equations. In addition, bulk viscous correction to the freezeout distribution function is also included. The detail study of the temporal evolution of shear and bulk stress, temperature, transverse velocity, spatial and momentum eccentricity, and the effect of shear and bulk viscosity on invariant yield and differential elliptic flow as a function of p_T are discussed in chapters 3 and 4.

To solve these hydrodynamic equations we need to provide initial conditions. In this thesis we have used a two component Glauber model based initial condition to calculate the initial energy density in transverse plane. In such an approach, the hard scattering fraction parameter (x) plays an important role. We have studied in detail the effect of varying hard scattering fraction x in the initialization of energy density on charged hadron p_T spectra and $v_2(p_T)$ for different collision centralities [109]. The details of this study is presented in appendix B. For comparing to experimental data the x value is fixed to that which best described the measured $dN_{ch}/d\eta$ as a function of collision centrality. The choice of a different initialization based on Color Glass Condensate model on p_T spectra and v_2 is discussed in appendix C.

In order to solve the energy-momentum conservation equations we need to provide an Equation of State (EoS). Equation of state is constructed by combining a recent lattice QCD calculation with 2+1 flavors [10], physical quark mass and quark hadron transition with a crossover temperature at ~ 170 MeV for vanishing net baryon density with a hadron resonance gas model considering all hadrons and resonances below mass 2.5 GeV.

We have used Cooper-Frey freezeout prescription to calculate hadron spectra from a constant temperature freezeout hypersurface. The resonance decay contribution to the thermal pion yield calculated on the freezeout surface is also included. The following decay channels of unstable hadrons with the corresponding branching ratios has been considered, $\rho^{0,-} \to \pi^-\pi^{+,0}, K^{*-,0} \to \pi^- K^{0,+}, \Delta \to \pi^- N, \omega \to \pi^+\pi^-\pi^0, \eta \to \pi^+\pi^-\pi^0$. We find the resonance contribution to the total pion yield at freezeout temperature of

130 MeV is about $\sim$ 30% and 50% at $\sqrt{s_{NN}}$=200 GeV and 2.76 TeV respectively.

Extracting η/s of the matter formed in heavy-ion collisions: Most of the studies presented in this thesis have focused primarily on comparison of our simulated results to two experimental data sets (i) Au-Au collision at $\sqrt{s_{NN}}$=200 GeV and (ii) Pb-Pb collision at $\sqrt{s_{NN}}$=2.76 TeV. The details of which have been presented in chapter-5.

For Au-Au collisions the experimental data includes $dN_{ch}/d\eta$ vs. N_{part}, $dN/d^2p_Td\eta$ vs. p_T, v_2 vs. N_{part}, $v_2(p_T)$ vs. p_T, and $v_4(p_T)$ vs. p_T. The collision centrality studied for these data sets at midrapidity are 0-10%, 10-20%, 20-30%, 30-40%, and 40-50%. The viscous hydrodynamics simulations were carried out for the following temperature independent input values of η/s=0.0, 0.08 , 0.12, 0.16, and 0.20. The observable $dN_{ch}/(0.5N_{part}d\eta)$ vs N_{part} is found to be insensitive to the various input values of η/s used in the simulation within the experimental errors associated with the charged particle multiplicity density. We find that shear viscosity increases the transverse velocity (v_T) of the fluid and hence p_T spectra becomes flatter. Compared to ideal fluid, in viscous evolution, high p_T production is enhanced. We find that the charged particles p_T spectra in 0-10% Au-Au collisions at $\sqrt{s_{NN}}$=200 GeV do not demand any viscosity. Whereas for other centralities the experimental data are well reproduced by viscous hydrodynamics simulations with a small ($\sim$ 0.08-0.12) value of η/s. The momentum anisotropy (ϵ_p) decreases in shear viscous evolution compared to the ideal fluid and hence v_2 decreases with increasing values of η/s. We find that the data on $v_2(p_T)$ vs. p_T is most sensitive to the value of η/s. From the comparison

between experimental data and viscous hydrodynamic simulations we observe that for peripheral collisions the fluid is more viscous (with higher values of η/s) compared to central collisions. The charged hadron v_2 data in 0-10% is best explained for simulations with η/s=0, 10-20% for η/s=0.12 and the remaining centralities for η/s around 0.16. Similar conclusions are drawn for v_2 vs. N_{part}. We find in simulations, like v_2, the values of v_4 also decreases with increase in η/s. The experimental data for 0-10% , 10-20%, and 20-30% centralities are above the ideal hydrodynamics simulation. Data for 30-40% and 40-50% centralities agrees with the ideal hydrodynamics simulation. This observation is in sharp contrast to what we have seen for the case of elliptic flow. In order to understand the v_4 results, it is important to investigate in future the role of initial conditions in viscous hydrodynamics simulation. These observation also emphasizes the need to experimentally measure the higher harmonics of flow for charged hadrons.

For Pb-Pb collisions the experimental data includes $dN_{ch}/d\eta$ vs. N_{part} (0-70% collision centrality), $dN/d^2p_Td\eta$ vs. p_T (0-5% collision centrality), v_2 vs. N_{part} (0-70% collision centrality), and $v_2(p_T)$ vs. p_T (10-20%, 20-30%, 30-40% and 40-50% collision centralities). The differences in the collision centralities compared to Au-Au collisions are primarily due to the availability of the experimental data at the time of this study. The viscous hydrodynamics simulations were carried out for the following temperature independent values of η/s=0.0, 0.08 , 0.12, and 0.16. The general conclusions for the various observables are similar to that seen for Au-Au collisions. The charged particles multiplicity data in $\sqrt{s_{NN}}$=2.76 TeV Pb-Pb collisions do not demand any viscosity [105]. We observe that $v_2(p_T)$ vs. p_T for peripheral collisions needs higher values of η/s compared to central collisions [119]. This is also true for the centrality dependence of

p_T integrated v_2. The best fit to the Pb-Pb data on integrated elliptic flow considered in this study is obtained for viscous hydrodynamic simulations with η/s=0.08. In the present analysis we have used some specific initial conditions, e.g. initial time τ_i=0.6 fm, initial zero fluid velocity, hard scattering fraction 0.9, boost-invariant shear stress tensor etc. All possible initial conditions are not explored in the work presented here. The systematic uncertainty in η/s due to various uncertainties in initial conditions could be as large as 175%. The presently extracted value of $\eta/s = 0.08 \pm 0.02$ will be even more uncertain, if all possible initial conditions are accounted for.

We observed for the RHIC energy, the extracted value of η/s lies between 1-4$\times 1/4\pi$, and at LHC the η/s is similar and lies close to $1/4\pi$. This led to the conclusion that a strongly coupled quark gluon plasma has been created in the heavy-ion collisions at both RHIC and LHC energy.

Outlook : In recent times there has been much progress in the field of application of relativistic viscous hydrodynamics to the high energy heavy-ion collisions. To explain the centrality dependence of charged hadron elliptic flow and p_T spectra, the shear viscosity was included in the hydrodynamics simulation. The experimentally measured odd harmonics of flow coefficients like v_3, v_5 etc. can now be explained with the inclusion of fluctuating initial conditions in hydrodynamics simulations. To explain the rapidity dependence of various experimental observables 3+1D viscous hydrodynamics have been developed [108]. In addition to the important role of knowing the proper initial conditions in high energy heavy-ion collisions on such hydrodynamic simulations

(e.g Glauber vs. CGC) there are still some open issues which should be studied in the future.

- Some recent calculations find that the initial magnetic field produced in heavy-ion collision at relativistic energies is of the order of eB $\sim 10^4\ MeV^2$ [173]. If sufficiently large magnetic field persists up to the thermalization time then this would have considerable effect on the subsequent fluid evolution. The current fluid evolution equations then needs to be modified to include the effect of the magnetic field.

- Initial reaction zone for heavy-ion collisions at non-zero impact parameter can have $\sim$ 1000 unit of angular momentum (in unit of $\hbar$)[174]. This would lead to a large vorticity in the fluid in order to conserve the initial angular momentum. Finite vorticity of the fluid will have measurable effects on the flow observables.

- The dissipative correction to the freezeout distribution function plays an important role on the p_T spectra calculated in the Cooper-Frey freezeout prescription and v_2. There are still theoretical uncertainties in prescription for dissipative correction to the freeze-out distribution function for both shear and bulk viscosity [84]. This needs to be settled in order to correctly estimate the η/s of QGP.

- We have used a temperature independent form of input η/s and a temperature dependent ζ/s for our viscous hydrodynamics simulations. However it is expected that η/s is also temperature dependent [74]. The present theoretical knowledge of the temperature dependence of both the shear and bulk viscosity for QCD

matter is quite uncertain. The higher values of shear stresses can also induce the phenomenon of cavitation as discussed in reference [175].

- RHIC beam energy scan program provides experimental data for $\sqrt{s_{NN}}$ = 7.7 - 39 GeV, corresponding to baryon chemical potential values between 450 - 100 MeV respectively [176]. These data, when compared to viscous hydrodynamic simulations will allow for obtaining the η/s of the QCD matter in the T, μ_B plane of the QCD phase digram. For this, one needs to solve the viscous hydrodynamic equations at finite baryon density (for calculations presented in this thesis corresponding to $\sqrt{s_{NN}}$ = 200 and 2760 GeV this effect is neglected). In addition the role of chemical freeze-out also needs to be investigated in details.

Appendix A

Hydrodynamics equations in curvilinear co-ordinate

The metric tensor for (τ, x, y, η) co-ordinate system is

$$g^{\mu\nu} = (1, -1, -1, -\frac{1}{\tau^2}), \quad g_{\mu\nu} = (1, -1, -1, -\tau^2). \tag{A.1}$$

The energy momentum conservation equations in the general curvilinear co-ordinate has the following form,

$$\partial_\mu; T^{\mu\nu} = \partial_\mu T^{\mu\nu} + \Gamma^\mu_{\mu\alpha} T^{\alpha\nu} + \Gamma^\nu_{\mu\alpha} T^{\mu\alpha}, \tag{A.2}$$

where the symbol $\Gamma^\nu_{\mu\alpha}$ is the Christoffel symbol of second kind. The only non-vanishing Christoffel symbols in (τ, x, y, η) co-ordinates are

$$\Gamma^\eta_{\tau\eta} = \Gamma^\eta_{\eta\tau} = \frac{1}{\tau}, \tag{A.3}$$

and

$$\Gamma^\tau_{\eta\eta} = \tau. \tag{A.4}$$

Case-I For ν=0, we have from equation A.2,

$$\begin{aligned}
\Rightarrow \partial_\tau T^{\tau\tau} + \partial_x T^{x\tau} + \partial_y T^{y\tau} + \Gamma^\mu_{\mu\alpha} T^{\alpha\tau} + \Gamma^\tau_{\mu\alpha} T^{\mu\alpha} &= 0 \\
\Rightarrow \partial_\tau T^{\tau\tau} + \partial_x T^{x\tau} + \partial_y T^{y\tau} + \Gamma^\eta_{\eta\tau} T^{\tau\tau} + \Gamma^\tau_{\eta\eta} T^{\eta\eta} &= 0 \\
\Rightarrow \partial_\tau T^{\tau\tau} + \partial_x T^{x\tau} + \partial_y T^{y\tau} + \frac{T^{\tau\tau}}{\tau} + \tau\left[\frac{P+\Pi+\tau^2\pi^{\eta\eta}}{\tau}\right] &= 0 \\
\Rightarrow \partial_\tau\left(\tau T^{\tau\tau}\right) + \partial_x\left(\tau T^{\tau\tau}\frac{T^{x\tau}}{T^{\tau\tau}}\right) + \partial_y\left(\tau T^{\tau\tau}\frac{T^{y\tau}}{T^{\tau\tau}}\right) &= -\left[P+\Pi+\tau^2\pi^{\eta\eta}\right] \\
\Rightarrow \partial_\tau\left(\tilde{T}^{\tau\tau}\right) + \partial_x\left(\tilde{T}^{\tau\tau}\bar{v_x}\right) + \partial_y\left(\tilde{T}^{\tau\tau}\bar{v_y}\right) &= -\left[P+\Pi+\tau^2\pi^{\eta\eta}\right] \quad \text{(A.5)}
\end{aligned}$$

Case-II For $\nu = 1$ the equation A.2 gives

$$\begin{aligned}
\partial_\tau T^{\tau x} + \partial_x T^{xx} + \partial_y T^{yx} + \Gamma^\mu_{\mu\alpha} T^{\alpha x} + \Gamma^x_{\mu\alpha} T^{\mu\alpha} &= 0 \\
\Rightarrow \partial_\tau T^{\tau x} + \partial_x T^{xx} + \partial_y T^{yx} + \Gamma^\eta_{\eta\tau} T^{\tau x} &= 0 \\
\Rightarrow \partial_\tau T^{\tau x} + \partial_x T^{xx} + \partial_y T^{yx} + \frac{T^{\tau x}}{\tau} &= 0 \\
\Rightarrow \partial_\tau\left(\tau T^{\tau x}\right) + \partial_x\left(\tau T^{xx}\right) + \partial_y\left(\tau T^{yx}\right) &= 0 \\
\Rightarrow \partial_\tau\left(\tau T^{\tau x}\right) + \partial_x\left[\tau\left\{T^{\tau x} - \pi^{\tau x}\right\} v_x\right] + \partial_y\left[\tau\left\{T^{\tau x} - \pi^{\tau x}\right\} v_y\right] &= -\partial_x\left[\tau\left\{P+\Pi+\pi^{xx}\right\}\right] - \partial_y\left[\tau\pi^{xx}\right] \\
\Rightarrow \partial_\tau\left[\widetilde{T}^{\tau x}\right] + \partial_x\left[\left\{\widetilde{T}^{\tau x} - \widetilde{\pi}^{\tau x}\right\} v_x\right] + \partial_y\left[\left\{\widetilde{T}^{\tau x} - \widetilde{\pi}^{\tau x}\right\} v_y\right] &= -\partial_x\left[\widetilde{P}+\widetilde{\Pi}+\widetilde{\pi}^{xx}\right] - \partial_y\left[\widetilde{\pi}^{yx}\right] \quad \text{(A.6)}
\end{aligned}$$

To derive the last two lines we have used the following expressions,

- $\widetilde{T}^{\mu\nu} = \tau T^{\mu\nu}$,
- $T^{\tau x} = (\epsilon + P + \Pi)\,\gamma_\perp^2 v_x + \pi^{\tau x}$,
- $T^{xx} = (\epsilon + P + \Pi)\,\gamma_\perp^2 v_x^2 + (P + \Pi) + \pi^{xx}$,
- $T^{\tau y} = (\epsilon + P + \Pi)\,\gamma_\perp^2 v_x v_y + \pi^{yx}$,

where the T^{xx} and T^{yx} are expressed in terms of $T^{\tau x}$ in the following way

- $T^{xx} = \left[T^{\tau x} - \pi^{\tau x}\right] v_x + (P + \Pi) + \pi^{xx}$,
- $T^{yx} = \left[T^{\tau x} - \pi^{\tau x}\right] v_y + \pi^{yx}$.

Case-III Similarly for $\nu = 2$ we have

$$\Rightarrow \partial_\tau \left[\widetilde{T}^{\tau y}\right] + \partial_x \left[\left\{\widetilde{T}^{\tau y} - \widetilde{\pi}^{\tau y}\right\} v_x\right] + \partial_y \left[\left\{\widetilde{T}^{\tau y} - \widetilde{\pi}^{\tau y}\right\} v_y\right] = -\partial_y \left[\widetilde{p} + \widetilde{\Pi} + \widetilde{\pi}^{yy}\right] - \partial_x \left[\widetilde{\pi}^{xy}\right] \quad \text{(A.7)}$$

Finally the equations A.5, A.6, A.7 are rearranged in the following form to implement them in the SHASTA algorithm,

$$\begin{aligned}
\partial_\tau \left(\tilde{T}^{\tau\tau}\right) + \partial_x \left(\tilde{T}^{\tau\tau} \bar{v_x}\right) + \partial_y \left(\tilde{T}^{\tau\tau} \bar{v_y}\right) &= -\left[P + \Pi + \tau^2 \pi^{\eta\eta}\right] \\
\partial_\tau \left[\widetilde{T}^{\tau x}\right] + \partial_x \left[v_x \widetilde{T}^{\tau x}\right] + \partial_y \left[v_y \widetilde{T}^{\tau x}\right] &= -\partial_x \left[\widetilde{P} + \widetilde{\Pi} + \widetilde{\pi}^{xx} - v_x \widetilde{\pi}^{\tau x}\right] - \partial_y \left[\widetilde{\pi}^{yx} - v_y \widetilde{\pi}^{\tau x}\right] \\
\partial_\tau \left[\widetilde{T}^{\tau y}\right] + \partial_x \left[v_x \widetilde{T}^{\tau y}\right] + \partial_y \left[v_y \widetilde{T}^{\tau y}\right] &= -\partial_y \left[\widetilde{P} + \widetilde{\Pi} + \widetilde{\pi}^{yy} - v_y \widetilde{\pi}^{\tau y}\right] - \partial_x \left[\widetilde{\pi}^{xy} - v_x \widetilde{\pi}^{\tau y}\right].
\end{aligned}$$

For completeness we write down here the relaxation equations of $\pi^{\mu\nu}$ and Π,

$$\begin{aligned}
\partial_\tau \pi^{xx} + \partial_x (v_x \pi^{xx}) + \partial_y (v_y \pi^{xx}) &= -\frac{1}{\tau_\pi \gamma} \left(\pi^{xx} - 2\eta\sigma^{xx}\right) - \frac{1}{\gamma} I_1^{xx} + \pi^{xx} \left(\partial_x v^x + \partial_y v^y\right), \\
\partial_\tau \pi^{yy} + \partial_x (v_x \pi^{yy}) + \partial_y (v_y \pi^{yy}) &= -\frac{1}{\tau_\pi \gamma} \left(\pi^{yy} - 2\eta\sigma^{yy}\right) - \frac{1}{\gamma} I_1^{yy} + \pi^{yy} \left(\partial_x v^x + \partial_y v^y\right), \\
\partial_\tau \pi^{xy} + \partial_x (v_x \pi^{xy}) + \partial_y (v_y \pi^{xy}) &= -\frac{1}{\tau_\pi \gamma} \left(\pi^{xy} - 2\eta\sigma^{xy}\right) - \frac{1}{\gamma} I_1^{xy} + \pi^{xy} \left(\partial_x v^x + \partial_y v^y\right).
\end{aligned}$$

and

$$\partial_\tau \Pi + \partial_x (v_x \Pi) + \partial_y (v_y \Pi) = -\frac{1}{\tau_\Pi \gamma} \left[\Pi + \zeta\theta + \frac{1}{2} \Pi \tau_\Pi \theta + \zeta T \Pi D \left(\frac{\tau_\Pi}{\zeta T}\right)\right] + \Pi \left(\partial_x v^x + \partial_y v^y\right). \quad \text{(A.8)}$$

The terms γ, $I_1^{\mu\nu}$, τ_π, and τ_Π are already defined in chapter-2.

Appendix B

Effect of hard scattering fraction

In this appendix we discuss the effect of varying hard scattering fraction x in the initialization of energy density in transverse plane on charged hadron p_T spectra and $v_2(p_T)$ for different collision centralities. The use of a two component Glauber model initialization for the energy density profile is motivated by the findings in [177]. In reference [177] the multiplicity of charged hadron per unit pseudo-rapidity in p-p collisions $n_{pp} = \frac{dN_{ch}}{d\eta}$ was explained by assuming that a fraction x of multiplicity is generated due to hard 'processes' and the rest $(1-x)$ is due to soft processes. Assuming that hard processes scales with the binary collision numbers (N_{coll}) and the soft processes scales with the participant numbers (N_{part}), the pseudo-rapidity density in nucleus-nucleus collisions was then parameterized as,

$$\frac{dN}{d\eta} = n_{pp}\left[(1-x)\frac{N_{part}}{2} + xN_{coll}\right]. \tag{B.1}$$

Where one computes the N_{part} and N_{coll} from Glauber model. PHOBOS collaboration studied the geometric scaling of pseudo-rapidity density in $\sqrt{s_{NN}}$=19.6 and 200 GeV

Au-Au collisions [178]. According to their finding for both the collision energies, hard scattering fraction is approximately constant, $x = 0.13 \pm 0.01(stat) \pm 0.05(sys)$.

Following equation B.1, in a non-central Au-Au collision for impact parameter b, the initial energy density in the transverse plane can be parameterized as,

$$\epsilon(x, y; b) = \epsilon_0 \left[(1 - x)N_{part}(x, y; b) + xN_{coll}(x, y; b)\right], \tag{B.2}$$

where $N_{part}(x, y; b)$ and $N_{coll}(x, y; b)$ are the transverse density distribution for the participant pairs and the collision number respectively. Ideal hydrodynamics, with Glauber model initialization, with hard scattering fraction $x = 0.25$, explains a variety of experimental data, e.g. identified particle's multiplicity, mean momentum, p_T spectra, elliptic flow etc [179]. Glauber model initialization of the energy density, with $x = 0.13$, also gives a reasonable description to the experimental data [160]. One inconsistency however remained. Glauber model initialization with hard scattering fraction $x = 0.25$ or $x = 0.13$, under predict experimental elliptic flow in very central, e.g. 0-10% collisions.

Dissipative effects can not be the reason. Inclusion of dissipative effects only reduces elliptic flow. To understand the relation between elliptic flow in central Au-Au collisions and the geometric scaling of initial energy density as in equation B.2, we have simulated $\sqrt{s_{NN}}$=200 GeV Au-Au collisions with Glauber model initial condition at two extreme limits of the hard scattering fraction, $x = 0$ and $x = 1$. Two limits corresponds to very different collision dynamics, for $x = 0$, initial energy density scales with participant

density implying that Au-Au collisions are completely dominated by the soft processes. For $x = 1$, Au-Au collisions are completely dominated by the hard processes and the initial energy density scales with the density of binary collision numbers. Actual scenario is in between the two extreme limits.

Details of the hydrodynamic model has already been discussed in Chapter-2 and can also be found in [179]. We assume that the fluid is thermalized in the time scale τ_0=0.6 fm [179]. At τ_0=0.6 fm, energy density in the transverse plane is distributed as in equation B.2, with hard scattering fraction (i) $x = 0$ or (ii) $x = 1$. Irrespective of the hard scattering fraction, initial fluid velocity is assumed to be zero, $v_x(x, y) = v_y(x, y) = 0$ and the fluid is assumed to undergo kinetic freeze-out at temperature T_{fo}=150 MeV. For this study we have used lattice+hrg EoS [124] where the confinement-deconfinement transition is a cross-over at T_{co}=196 MeV [180].

With hard scattering fraction fixed, either $x = 0$ or $x = 1$, central energy density ϵ_0 is the only parameter left in the modeling of the initial energy density profile. We fix ϵ_0 by fitting the PHENIX data on charged particles p_T spectra in 0-10% Au-Au collisions [151]. For $x = 0$, best fit to the 0-10% data is obtained with ϵ_0=36.1 GeV/fm^3. PHENIX data require ∼30% higher central energy density, ϵ_0=48 GeV/fm^3, if Au-Au collision is completely dominated by the hard processes ($x = 1$). The solid and the dashed lines in figure B.1a are fit to the data with hard scattering fraction $x = 1$ and $x = 0$ respectively. Data are well fitted. Charged particles p_T spectra in central Au-Au collision is insensitive to the hard scattering fraction x in the Glauber model of initial condition.

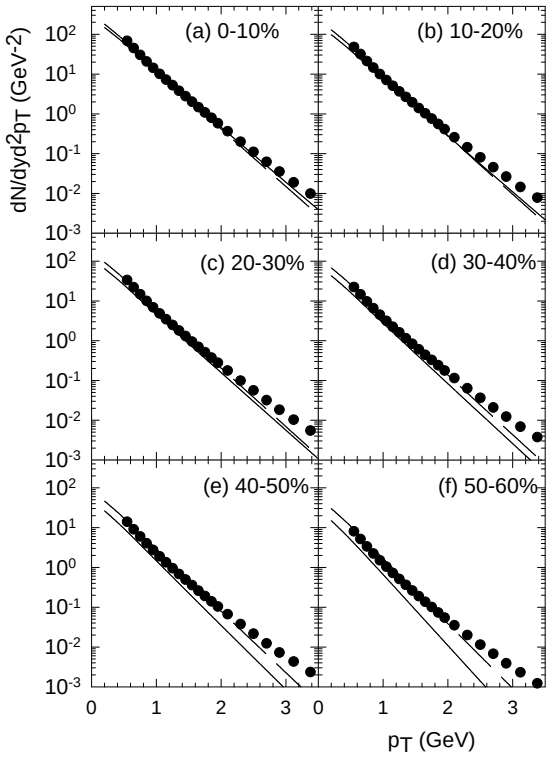

Figure B.1: In panels (a-f) PHENIX data [151] on the charged particle transverse momentum spectra in 0-60% Au-Au collisions are compared with hydrodynamic model predictions. The dashed lines are the predictions when initial energy density scales with participant density ($x = 0$). The solid line are predictions when energy density scales with density distribution of binary collision numbers ($x = 1$).

With initial energy density fixed, we can predict for the p_T spectra in all the other collision centralities. In figure B.1, in panels (b-f), model predictions for the charged particles p_T spectra in 10-20%, 20-30%, 30-40%, 40-50%, and 50-60% Au-Au collisions are compared with the PHENIX data [151]. When central energy density is fixed to reproduce charged particles p_T spectra in 0-10% collisions, Glauber model initialisation with $x = 1$, also give reasonable description to the spectra in 10-20% and 20-30% centrality collisions. But in more peripheral collisions, PHENIX data are under predicted.

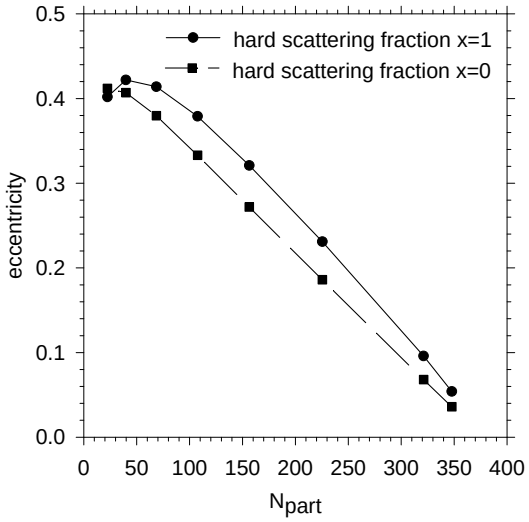

Figure B.2: Initial eccentricity of the collision zone as a function of participant numbers. The filled circles and squares are eccentricity with hard scattering fraction 0 and 1 respectively.

Initialization with hard scattering fraction $x = 0$ however continue to explain data till very peripheral collisions, though description to the data deteriorates at larger p_T or in more peripheral collisions. It appears that if in Au-Au collisions, energy density scales with participant density ($x = 0$), charged particles p_T spectra in 0-60% Au-Au collisions are reasonably well explained. On the contrary, if energy density scales with binary collision number density ($x = 1$), charged particles p_T spectra, only in central (0-30%) collisions is explained.

Let us now concentrate on the centrality dependence of simulated elliptic flow. In a hydrodynamic model, elliptic flow depends on the initial spatial eccentricity, $\varepsilon_x = \frac{\langle y^2 - x^2 \rangle}{\langle x^2 + y^2 \rangle}$, $\langle ... \rangle$ denotes energy density weighted averaging. In figure B.2, centrality dependence of ε_x, in the two extreme limits $x = 0$ (filled circles) and $x = 1$ (filled

squares) are shown. ε_x is more if Au-Au collisions are dominated by the hard processes ($x = 1$) rather than the soft processes ($x = 0$). Glauber model initialization of energy density with hard scattering fraction $x = 1$ will generate more elliptic flow than the initialization with $x = 0$.

In figure B.3, we have compared the simulated v_2 with PHENIX measurements [158] by three different methods (i) event plane method from two independent sub-detectors, $v_2\{BBC\}$, (ii)$v_2\{ZDC - SMD\}$ and (iii) two particle cumulant $v_2\{2\}$.

The solid and dashed lines in figure B.3 corresponds to Glauber model initial conditions with $x = 1$ and $x = 0$ respectively. As expected from the eccentricity study (figure B.2), in all the collision centralities, Glauber model initialization with $x = 1$ generate more flow than the initialization with $x = 0$. Unlike the p_T spectra in central Au-Au collisions, which do not distinguish between the initial conditions with $x = 1$ and $x = 0$, elliptic flow, being a more sensitive observable, can distinguish between them. It is very interesting to note that Glauber model initialization with hard scattering fraction $x = 1$ well explain the PHENIX data on elliptic flow in 0-10% Au-Au collisions. However, in all the other collision centralities elliptic flow is over predicted. For example, at $p_T \approx$1.5 GeV, simulated flow with $x = 1$ over predict experiments by $\sim$20%, 25%, 35%, 45%, and 60% in 10-20%, 20-30%, 30-40%, 40-50%, and 50-60% Au-Au collisions respectively. Glauber model initialization with hard scattering fraction $x = 0$ gives a lower value of eccentricity and elliptic flow in 0-10% Au-Au collisions is underpredicted e.g., at $p_T \sim$1.5 GeV, it under predicts the experimental data by $\sim$35%. In all the other collision centrality agreement with data are comparatively bet-

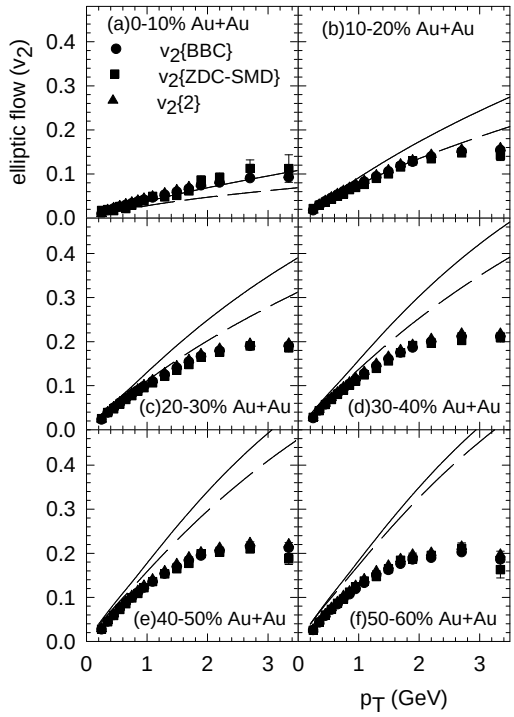

Figure B.3: The filled circles, squares and triangles are PHENIX measurements [158] for elliptic flow in 0-60% Au-Au collisions. The solid and dashed lines are elliptic flow in hydrodynamic simulations with hard scattering fraction x=1 and x=0 respectively.

ter. In 10-20% and 20-30% Au-Au collisions, Glauber initialisation with $x = 0$ give very good description of the data up to p_T ∼1.5 GeV. In more peripheral collisions, flow is over predicted. Even then agreement with data is better than that obtained with hard scattering fraction $x = 1$. For example at p_T ≈1.5 GeV, simulated flow over predicts PHENIX data by ∼ 15%, 25%, and 50% in 30-40%, 40-50%, and 50-60% collisions respectively.

Present analysis indicates that in 0-10% Au-Au collisions, simultaneous description of p_T spectra and elliptic flow require hard scattering fraction $x = 1$ in the Glauber

model of initial condition. In less central collisions however, simultaneous description of p_T spectra and elliptic flow are best obtained with hard scattering fraction $x = 0$. The result implies that geometric scaling of Au-Au collisions changes with collision centrality. In a central collision, energy density scales with binary collision number density while in a less central collision, energy density scales with participant density. Arguably, transition from binary collision number scaling to participant scaling can not be as sharp as conjectured here. More detailed analysis is required to find the width and exact location of the transition.

Such a transition may have implications for the hydrodynamical analysis also. Note that for binary collision number scaling, fluid has to be initialized at higher energy density (ε_0=48 GeV/fm^3 for $x = 1$ and ε_0=36.1 GeV/fm^3 for $x = 0$). We have assumed similar thermalization time τ_0=0.6 fm for both the scaling conditions. Since thermalsation time scale is expected to be inversely proportional to the energy density, it is likely that the fluid in central Au-Au collisions will thermalise in a shorter time scale compared to the thermalization time of the fluid in less central collisions.

The result may also have implication on the dynamics of the pre-equilibrium stage. Hydrodynamic models assume local thermalization. The fluid produced in Au-Au collisions evolves through a pre-equilibrium stage to equilibration. At present, we have limited knowledge about the pre-equilibrium stage. Present results suggests that in 0-10% Au-Au collisions, pre-equilibrium stage is dominated by binary collisions, but in a less central collision, pre-equilibrium stage is dominated by the 'wounded' nucleons.

In the present analysis, the effect of viscosity is neglected.

Effect of viscosity is to enhance particle production mainly at large p_T, and also to reduce elliptic flow. One observes from figure B.1 and B.3, that in 0-10% Au-Au collisions, if initial energy density scales with collision number density, ideal fluid dynamics hardly leaves any scope for viscous enhancement of p_T spectra or for viscous suppression of elliptic flow. Assumption of viscous fluid evolution can only worsen the fit to the elliptic flow. We conclude that the PHENIX data on the charged particles p_T spectra and elliptic flow in 0-10% Au-Au collisions do not demand any viscosity. Viscosity however can be important in peripheral collisions. In peripheral collisions, experimental p_T spectra and elliptic flow are better explained if energy density scales with participant density. However, at large p_T elliptic flow is over predicted. With viscous suppression agreement with data will be better as shown in this thesis.

In the present calculations we have not included eccentricity fluctuation. In [160], effect of eccentricity fluctuation on elliptic flow was studied in detail. Eccentricity fluctuation increases elliptic flow. A 3+1D hydrodynamics calculation with eccentricity fluctuations also provide a reasonable explanation of the central v_2 data from PHENIX [108].

Appendix C

2+1D viscous hydrodynamics with Color Glass Condensate based initial condition

In this appendix we discuss the 2+1D relativistic viscous hydrodynamic simulations with initial conditions based on the Color-Glass-Condensate (CGC) approach [106, 181]. We compare the simulated results to calculations with Glauber based initial conditions and experimental data at RHIC. We have used the KLN (Kharzeev-Levin-Nardi) k_T-factorization approach [182], due to Drescher *et al.* [111]. The energy-momentum conservation equations and relaxation equations for shear stress, other initial conditions, equation of state and freeze-out conditions are same as discussed in chapter-5 for Au-Au collisions at $\sqrt{s_{NN}} = 200$ GeV.

We follow references [78, 183] and consider that the initial energy density can be

obtained from the gluon number density through the thermodynamic relation,

$$\epsilon(\tau_i, \mathbf{x}_T, b) = \mathrm{C} \times \left[\frac{dN_g}{d^2\mathbf{x}_T dY}(\mathbf{x}_T, b)\right]^{4/3}, \tag{C.1}$$

where $\frac{dN_g}{d^2\mathbf{x}_T dY}$ is the gluon number density evaluated at central rapidity $Y = 0$ and the overall normalization C is a free parameter. C is fixed to reproduce the experimentally measured charged particle multiplicity density at midrapidity. The values of C used in the simulations for different input values of η/s are given in Table C.1. The number density of gluons produced in a collision of two nuclei with mass number A is given by

$$\frac{dN_g}{d^2\mathbf{x}_T dY} = \mathcal{N} \int \frac{d^2\mathbf{p}_T}{p_T^2} \int^{p_T} d^2\mathbf{k}_T\, \alpha_s(k_T)\, \phi_A(x_1, (\mathbf{p}_T + \mathbf{k}_T)^2/4; \mathbf{x}_T)\, \phi_A(x_2, (\mathbf{p}_T - \mathbf{k}_T)^2/4; \mathbf{x}_T), \tag{C.2}$$

where $\mathbf{p}_T$ and Y are the transverse momentum and rapidity of the produced gluons, respectively. $x_{1,2} = p_T \times \exp(\pm Y)/\sqrt{s}$ is the momentum fraction of the colliding gluon ladders with $\sqrt{s}$ the center of mass collision energy and $\alpha_s(k_T)$ is the strong coupling constant at momentum scale $k_T \equiv |\mathbf{k}_T|$. $\mathcal{N}$ is the normalization constant. The unintegrated gluon distribution functions are taken as

$$\phi(x, k_T^2; \mathbf{x}_T) = \frac{1}{\alpha_s(Q_s^2)} \frac{Q_s^2}{\max(Q_s^2, k_T^2)} P(\mathbf{x}_T)(1-x)^4, \tag{C.3}$$

$P(\mathbf{x}_T)$ is the probability of finding at least one nucleon at transverse position $\mathbf{x}_T$ and is defined as $P(\mathbf{x}_T) = 1 - \left(1 - \frac{\sigma T_A}{A}\right)^A$, where $T_A = \int_{-\infty}^{\infty} dz \rho(z)$ is the thickness function and σ is the nucleon-nucleon cross section taken as 42 mb. The saturation scale at a given momentum fraction x and transverse coordinate $\mathbf{x}_T$ is given by $Q_s^2(x, \mathbf{x}_T) = 2\,\mathrm{GeV}^2 \left(\frac{T_A(\mathbf{x}_T)/P(\mathbf{x}_T)}{1.53/\mathrm{fm}^2}\right) \left(\frac{0.01}{x}\right)^\lambda$. The growth speed is taken to be $\lambda = 0.28$.

Space-time evolution : Figure C.1 shows the constant temperature contours corresponding to $T_{co} = 175$ MeV and $T_{fo} = 130$ MeV in the τ-x plane (at $y = 0$) indicating

Table C.1: Values of the normalization constant C used in CGC model for initial transverse energy density.

η/s	C (GeV/$fm^{1/3}$) CGC
0.0	0.11
0.08	0.095
0.12	0.085
0.16	0.070
0.18	0.065

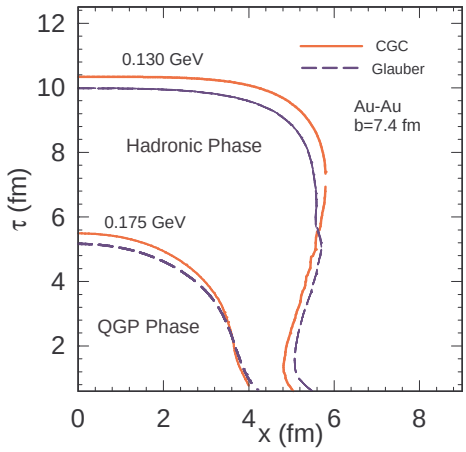

Figure C.1: Constant temperature contours denoting the space time boundaries of the QGP and hadronic phases from a 2+1D viscous hydrodynamic simulation with η/s = 0.08 for Au-Au collisions at impact parameter 7.4 fm. The solid red curves are simulations with initial transverse energy density profile based on CGC model while the dashed black curves correspond to initial conditions based on Glauber model.

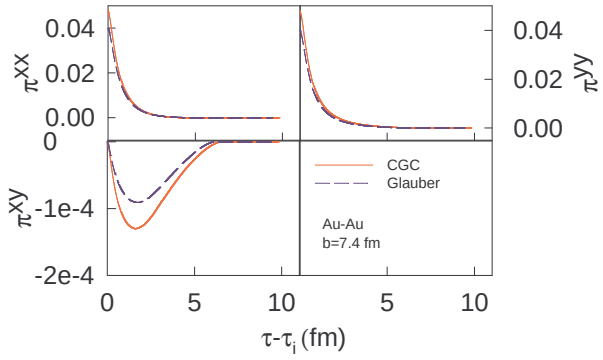

Figure C.2: The spatially averaged shear viscous stresses π^{xx}, π^{yy}, and π^{xy} as a function of evolution time for Au-Au collisions at impact parameter 7.4 fm and $\eta/s = 0.08$. The solid red and black dashed curves corresponds to simulations with CGC and Glauber based initial conditions respectively.

the boundaries for the QGP and hadronic phases respectively. The solid red curves corresponds to initial transverse energy density profile based on CGC model and the dashed black curve corresponds to results based on Glauber model initial conditions. We observe that the lifetime of QGP and hadronic phases are slightly extended for the simulations based on CGC initial conditions compared to Glauber based initial conditions. While the spatial extent of the hadronic phase is slightly smaller for the simulations with CGC initial conditions relative to Glauber based conditions.

Temporal evolution of shear stress : The temporal evolution of spatially averaged π^{xx}, π^{yy}, and π^{xy} are shown in figure C.2 for CGC (solid red curve) and Glauber (black dashed curve) initialization of energy density. All the three components of $\pi^{\mu\nu}$ becomes zero after time $\sim$ 7 fm irrespective of the CGC or Glauber model initialization. At initial time the values of spatially averaged π^{xx} and π^{yy} are observed to be larger for

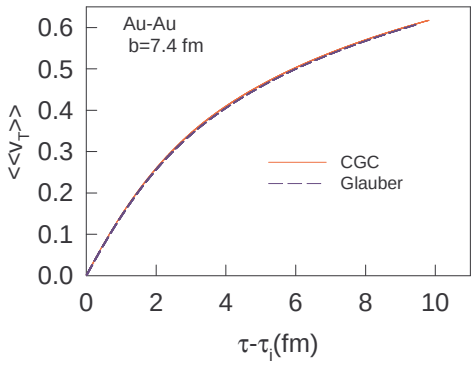

Figure C.3: Temporal evolution of spatially averaged transverse velocity $\langle\langle v_T \rangle\rangle$. The results are from a 2+1D viscous hydrodynamic simulation with $\eta/s = 0.08$. The solid red curve corresponds to simulated result with CGC based initial transverse energy density profile. The black dashed line is the simulated result with Glauber based initial conditions.

CGC compared to the Glauber initialization. However, the difference vanishes quickly ~ 3 fm. For π^{xy} a noticeable difference is seen for CGC and Glauber model initialization within time ~ 6 fm.

Average transverse velocity and eccentricity : Figure C.3 shows the temporal evolution of the spatially averaged transverse velocity ($\langle\langle v_T \rangle\rangle$) of the fluid with Glauber based and CGC based initial transverse energy density profile with fluid viscosity $\eta/s = 0.08$. The simulation is for Au-Au collisions at impact parameter, b = 7.4 fm. Solid red curve is for CGC based initial condition and the dashed black curve is for the Glauber based initial condition. We observe almost no change in the $\langle\langle v_T \rangle\rangle$ as a function of time for the two initial conditions studied. This effect should be reflected in the slope of the invariant yield of the charged hadrons as a function of transverse momentum being the

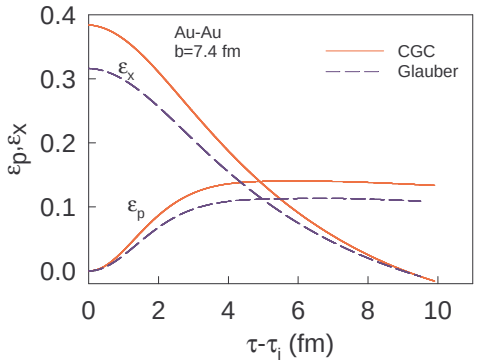

Figure C.4: The temporal evolution of spatial eccentricity (ε_x) and momentum anisotropy (ε_p) for Au-Au collisions at b=7.4 fm. The solid red curves corresponds to viscous hydrodynamics ($\eta/s = 0.08$) simulated results with CGC based initial condition and the black dashed lines corresponds to results with Glauber based initial condition.

same for both the initial conditions.

Figure C.4 shows the temporal evolution of the spatial eccentricity (ε_x) and the momentum space anisotropy (ε_p) of the viscous fluid ($\eta/s = 0.08$) with Glauber and CGC based initial conditions for Au-Au collisions at impact parameter, b = 7.4 fm. Solid red curve is for the CGC based initial condition and the dashed black curve is for the Glauber based initial condition. We find both ε_x and ε_p are higher for the simulated results with CGC based initial condition compared to initial condition based on Glauber model. As the simulated elliptic flow v_2 in hydrodynamic model is directly related to the temporal evolution of the momentum anisotropy, we expect the v_2 for the CGC based initial condition to be larger than the corresponding values for the Glauber based initial condition.

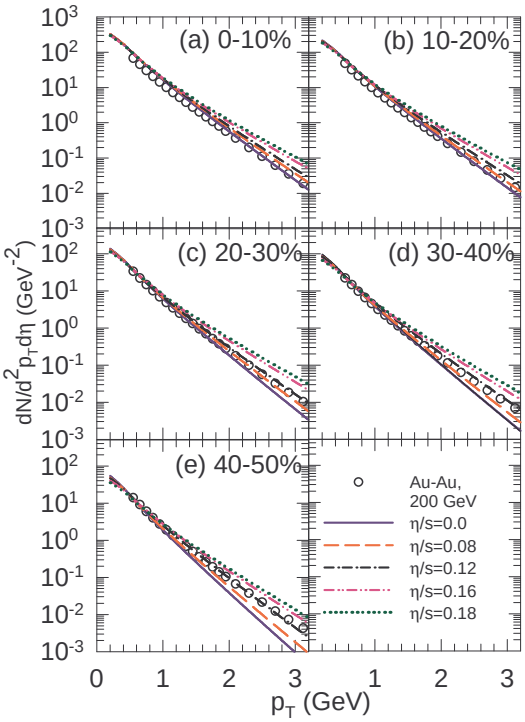

Figure C.5: Invariant yield of charged hadrons as a function of transverse momentum at midrapidity for Au-Au collisions at $\sqrt{s_{\rm NN}} = 200$ GeV. The open circles corresponds to experimental data measured by the PHENIX collaboration [151]. The lines represent results from a 2+1D relativistic viscous hydrodynamic model with a CGC based initial transverse energy density profile and for different η/s values.

Now we proceed to compare the simulated results based on CGC initial conditions to experimental data at RHIC. The experimental data used for comparison to our simulated results are from the PHENIX collaboration at RHIC [184, 151]. The observables used are invariant yield of charged hadrons, elliptic flow, and hexadecapole flow as a function of p_T for Au-Au collisions at pseudorapidity $\mid \eta \mid < 0.35$ for $\sqrt{s_{\rm NN}} = 200$ GeV.

Comparison to experimental data - Invariant yield : Figure C.5 shows invariant yield of charged hadrons as a function of transverse momentum at midrapidity for Au-Au collisions at $\sqrt{s_{\rm NN}}$ = 200 GeV for five different collision centralities (0-10%, 10-20%, 20-30%, 30-40%, and 40-50%). The open circles are the experimental data from the PHENIX collaboration [151]. The lines are simulated spectra with a CGC based initial transverse energy density profile. The fluid viscosity varies between η/s=0-0.18. We find the 0-10% experimental data is best explained by simulation with $\eta/s = 0.0$. Whereas data for collision centralities between 20-30% to 40-50% supports a η/s value within 0.08 to 0.12. Similar conclusions were drawn in chapter-5 for Glauber based initial conditions. This also means that the invariant yield of charged hadrons are not very sensitive to the choice of a Glauber based or CGC based initial conditions. The average transverse velocity at the freeze-out which determines the slope of the p_T spectra was observed to be similar for the fluid evolution with Glauber and CGC based initial conditions (see figure C.3).

Comparison to experimental data - Elliptic flow : Figure C.6 shows the elliptic flow (v_2) as a function of the transverse momentum (p_T) for charged hadrons at midrapidity in Au-Au collisions at $\sqrt{s_{\rm NN}}$ = 200 GeV. The results are shown for five different collision centralities (0-10%, 10-20%, 20-30%, 30-40%, and 40-50%). The open circles are the experimental data from the PHENIX collaboration [184]. Also shown for comparison the simulated results for ideal fluid evolution with Glauber based initial conditions. We find the $v_2(p_T)$ for CGC based initial condition is larger compared to corresponding results from Glauber based initial conditions (shown in chapter-5). This

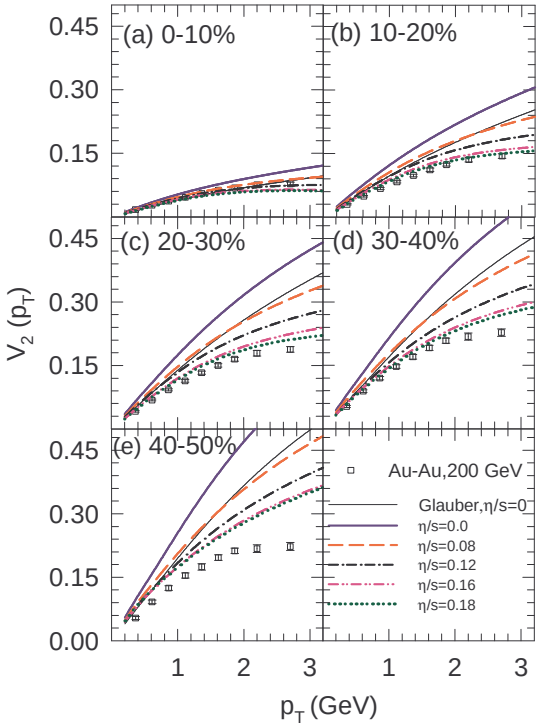

Figure C.6: Elliptic flow of charged hadrons as a function of transverse momentum at midrapidity for Au-Au collisions at $\sqrt{s_{\rm NN}} = 200$ GeV. The open circles corresponds to experimental data measured by the PHENIX collaboration [184]. The lines represent results from a 2+1D relativistic viscous hydrodynamic model with a CGC based initial transverse energy density profile and different η/s values.

can be understood from the fact that CGC based initial condition leads to a higher value of momentum anisotropy compared to Glauber based initial condition (as seen in figure C.4). The general conclusion that the experimental data prefers a higher value of η/s as we go from central to peripheral collisions as seen for viscous hydrodynamic simulations with Glauber based initial conditions (in chapter-5) also holds for those with the CGC based initial conditions. However, we find from the comparison of experimental data to simulations based on CGC initial conditions that the $v_2(p_T)$ data for 0-10% collisions is best explained for simulated results with η/s between 0.08-0.12. This is in contrast to what we saw from the comparisons of data to simulations with Glauber based initial conditions, where the data preferred $\eta/s = 0.0$ (see chapter-5). For more peripheral collisions (centralities beyond 20-30%), it seems data would prefer a higher value of $\eta/s \sim 0.18$. We do not present simulation results for $\eta/s > 0.18$ as the viscous hydrodynamic simulated spectra distributions show a large deviations from ideal fluid simulation results. This leads to a breakdown of the simulation frame work which is designed to be valid for case of small deviations of observables from ideal fluid simulations.

Comparison to experimental data - hexadecapole flow : Figure C.7 shows the hexadecapole flow (v_4) as a function of the transverse momentum (p_T) for charged hadrons at midrapidity in Au-Au collisions at $\sqrt{s_{\rm NN}} = 200$ GeV. The results are shown for five different collision centralities (0-10%, 10-20%, 20-30%, 30-40%, and 40-50%). The open circles are the experimental data from the PHENIX collaboration [184]. Simulated results for only ideal fluid evolution using Glauber based initial condition are

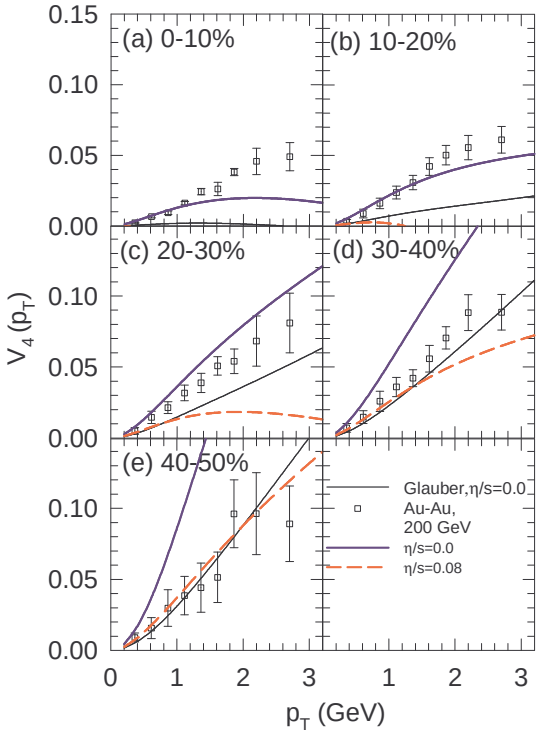

Figure C.7: Hexadecapole flow of charged hadrons as a function of transverse momentum at midrapidity for Au-Au collisions at $\sqrt{s_{\rm NN}} = 200$ GeV. The open circles corresponds to experimental data measured by the PHENIX collaboration [184]. The curves represent results from a 2+1D relativistic viscous hydrodynamic model with both Glauber based (same as in chapter-5) and CGC based initial transverse energy density profile and different η/s values.

shown (solid black curve, same as in chapter-5). While for the CGC based initial conditions the simulated results are shown for $\eta/s = 0.0$ (purple solid thick curve) and 0.08 (orange dashed curve). We find that $v_4(p_T)$ from ideal hydrodynamic simulations with Glauber based initial conditions under predict the experimental data for all the collision centralities except for the most peripheral collisions (40-50%). Comparison between the simulated results with CGC based initial condition and experimental data shows that the preferred η/s lies between 0.0 and 0.08 for the collision centralities studied.

Appendix D

Pion and Kaon p_T spectra at RHIC energy

In this appendix we discuss the comparison of ideal hydrodynamics simulation of p_T spectra for pions and kaons to the corresponding experimental measurements for Au-Au collisions at $\sqrt{s_{NN}}$=200 GeV for different centralities. The ideal hydrodynamic simulation is done for a lattice+hrg EoS with chemical equilibrium in the hadronic phase. The construction of lattice+hrg EoS is already discussed in chapter-2.

Initial conditions : At the initial time τ_0=0.6 fm, the fluid velocity is assumed to be zero, $v_x(x,y) = v_y(x,y) = 0$, the initial energy density of the fluid in the transverse plane is distributed as,

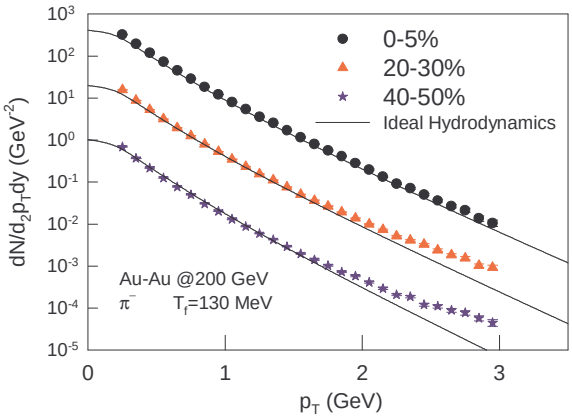

Figure D.1: PHENIX measurement of invariant yield of $(\pi^+ + \pi^-)/2$ as a function of transverse momentum p_T for Au-Au $\sqrt{s_{NN}}$ =200 GeV collision are shown for 0-5%, 20-30%, and 40-50% centrality collision [185]. Ideal hydrodynamics simulation results are shown by curves.

$$\varepsilon(\mathbf{b}, x, y) = \varepsilon_i \left[\frac{(1-x)}{2} N_{part}(\mathbf{b}, x, y) + x N_{coll}(\mathbf{b}, x, y) \right], \tag{D.1}$$

The details of which is also discussed in chapter-2. Freeze-out temperature is chosen to be T_{fo}=130 MeV.

With the initial conditions as described above, we have computed transverse momentum spectra of pions and kaons. In figure D.1, simulated pion spectra from ideal fluid evolution in 0-5%, 20-30%, and 40-50% Au-Au collisions are shown by curves. Corresponding experimental measurement by PHENIX collaboration are shown by symbols [185]. The total pion spectra for the hydrodynamics simulation was obtained by considering resonance decay contribution to the thermal pion yield for freezeout temperature T_{fo}=130 MeV.

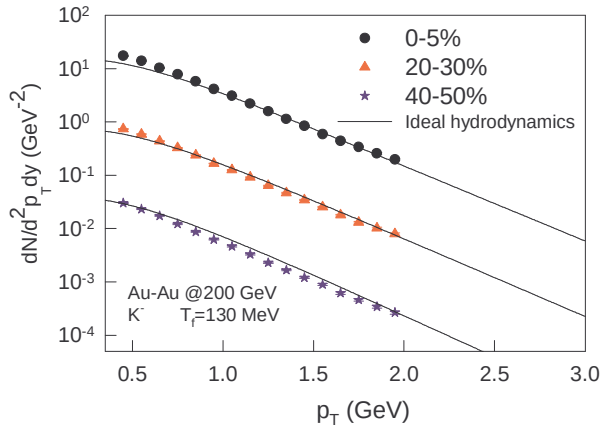

Figure D.2: PHENIX measurement of invariant yield of $(K^+ + K^-)/2$ as a function of transverse momentum p_T for Au-Au $\sqrt{s_{NN}}$ =200 GeV collision are shown for 0-5%, 20-30%, and 40-50% centrality collision [185]. Ideal hydrodynamics simulation results are shown by curves.

In figure D.2, PHENIX data [185] for $\frac{K^+ + K^-}{2}$ (symbols) are compared with ideal hydrodynamic model predictions (curves) . Pion and Kaon spectra in the centrality range 0-50% are well explained in ideal fluid evolution with kinetic freezeout temperature T_{fo}=130 MeV.

Appendix E

Shear viscous correction to the equilibrium freezeout distribution function

In Cooper Frey prescription, the particle's momentum distribution is obtained by integrating the one particle distribution function over the freeze-out hyper surface Σ_μ.

$$E\frac{dN}{d^3p} = \frac{g}{(2\pi)^3}\int d\Sigma_\mu p^\mu f(p^\mu u_\mu, T), \tag{E.1}$$

where g is the degeneracy factor of the particles. $f(p^\mu u_\mu, T)$ is the one particle Juttner distribution function. The above equation can also be written in terms of transverse momentum (p_T) and momentum-space rapidity (y) as,

$$\frac{dN}{d^2p_T dy} = \frac{g}{(2\pi)^3}\int_\Sigma d\Sigma_\mu p^\mu f(p^\mu u_\mu, T). \tag{E.2}$$

In the presence of viscosity the equilibrium distribution function modified as

$$f = f_{eq} + \delta f. \tag{E.3}$$

Considering only shear viscosity we have,

$$\delta f_{shear} = \frac{1}{2(\epsilon + p)T^2} f_0 \left(1 + f_0\right) p^\mu p^\nu \pi_{\mu\nu} \tag{E.4}$$

The four momentum of the fluid element is $p^\mu = (m_T cosh y, p_x, p_y, m_T sinh y)$ where $m_T = \sqrt{m_0^2 + p_T^2}$ and the momentum rapidity is $y = \frac{1}{2} ln \frac{E+p_z}{E-p_z}$. Thus,

$$\begin{aligned} p_\mu p_\nu \pi^{\mu\nu} &= m_T^2(\pi^{\tau\tau} + \tau^2\pi^{\eta\eta})cosh^2(\eta - y) \\ -2m_T(p_x\pi^{\tau x} + p_y\pi^{\tau y})cosh(\eta - y) + p_x^2\pi^{xx} + p_y^2\pi^{yy} + 2p_x p_y \pi^{xy} - m_T^2\tau^2\pi^{\eta\eta} \\ &= a_1 cosh^2(\eta - y) + a_2 cosh(\eta - y) + a_3. \end{aligned} \tag{E.5}$$

Where

$$\begin{aligned} a_1 &= m_T^2(\pi^{\tau\tau} + \tau^2\pi^{\eta\eta}), \\ a_2 &= -2m_T(p_x\pi^{\tau x} + p_y\pi^{\tau y}), \\ a_3 &= p_x^2\pi^{xx} + p_y^2\pi^{yy} + 2p_x p_y \pi^{xy} - m_T^2\tau^2\pi^{\eta\eta}. \end{aligned}$$

The freeze-out hypersurface in (τ, x, y, η) co-ordinate with boost invariance is given as

$$d\Sigma_\mu = \left(m_T cosh\eta, -\frac{\partial\tau_f}{\partial x}, -\frac{\partial\tau_f}{\partial y} m_T sinh\eta\right) \tau_f dx dy d\eta. \tag{E.6}$$

Then the dot product of p^μ with $d\Sigma_\mu$ results in,

$$p^\mu . d\Sigma_\mu = \left(m_T cosh(\eta - y) - \vec{p}_T . \vec{\nabla}_T \tau_f\right) \tau_f dx dy d\eta. \tag{E.7}$$

The shear viscous correction to the invariant yield is,

$$\frac{dN_{neq}}{dy d^2 p_T} = \frac{g}{(2\pi)^3} \int_\Sigma d\Sigma_\mu p^\mu \delta f(x, p)$$

$$= \frac{g}{(2\pi)^3}\int \tau_f dxdyd\eta \frac{1}{2(\varepsilon+p)T^2}\frac{1}{e^{[\beta(p^\mu u_\mu-\mu)]}\pm 1}p^\mu p^\nu \pi^{\mu\nu}$$
$$\Big[m_T cosh(\eta-y)-\vec{p}_T.\vec{\nabla}_T\tau_f(x,y)\Big]$$
$$= \frac{g}{2(\epsilon+p)T^2\,(2\pi)^3}\int \tau_f dxdyd\eta \sum_{n=1}^{\infty}(\mp 1)^{n+1}e^{-n\beta[\gamma(m_T cosh(\eta-y)-\vec{p}_T.\vec{v}_T)-\mu]}$$
$$p_\mu p_\nu \pi^{\mu\nu}\Big[m_T cosh(\eta-y)-\vec{p}_T.\vec{\nabla}_T\tau_f(x,y)\Big]$$
$$= \frac{g}{2(\epsilon+p)T^2\,(2\pi)^3}\int \tau_f dxdy \sum_{n=1}^{\infty}(\mp 1)^{n+1}e^{n\beta[\gamma\vec{p}_T\vec{v}_T+\mu]}$$
$$\int_{-\infty}^{\infty} d\eta\left(a_1 cosh^2(\eta-y)+a_2 cosh(\eta-y)+a_3\right)\Big[m_T cosh(\eta-y)-\vec{p}_T.\vec{\nabla}_T\tau_f(x,y)\Big]. \quad \text{(E.8)}$$

Denoting the first part of the right hand side of the above equation by I_1 we have

$$\frac{dN_{neq}}{dyd^2p_T} = 2I_1\int_0^{\infty} d\eta[a_1 m_T cosh^3(\eta-y)-a_1\vec{p}_T.\vec{\nabla}_T\tau_f(x,y)cosh^2(\eta-y)$$
$$+a_2 m_T cosh^2(\eta-y)-a_2\vec{p}_T.\vec{\nabla}_T\tau_f(x,y)cosh(\eta-y)$$
$$+a_3 m_T cosh(\eta-y)-a_3\vec{p}_T.\vec{\nabla}_T\tau_f]e^{-n\beta\gamma m_T cosh(\eta-y)}. \quad \text{(E.9)}$$

Where

$$I_1 = \frac{g}{2(\epsilon+p)T^2\,(2\pi)^3}\int \tau_f dxdy \sum_{n=1}^{\infty}(\mp 1)^{n+1}e^{n\beta[\gamma\vec{p}_T\vec{v}_T+\mu]}.$$

We will use the following definition of modified Bessel function and the relationship of hyperbolic functions to further simplify the equation E.9. The n-th order modified Bessel function of the second kind is defined as

$$k_n(x) = \int_0^{\infty} cosh(nt)e^{-xcosht}dt. \quad \text{(E.10)}$$

The hyperbolic functions are,

$$cosh^2 t = \frac{1}{2}\left[cosh(2t)+1\right], \quad \text{(E.11)}$$

and

$$cosh^3 t = \frac{1}{4}\left[cosh(3t) + 3cosht\right]. \tag{E.12}$$

Using these relations into equation E.9 and also defining $\beta_T = \beta\gamma m_T$ and changing the integration variable as $(\eta - y) = t$ we have

$$\begin{aligned}\frac{dN_{neq}}{dyd^2p_T} = 2I_1[&\frac{a_1 m_T}{4}\int_0^\infty cosh(3t)e^{-n\beta_T cosht}dt + \frac{3a_1 m_T}{4}\int_0^\infty cosht\ e^{-n\beta_T cosht}dt \\ &-\frac{a_1}{2}\vec{p}_T.(\vec{\nabla}_T\tau_f)\int_0^\infty cosh(2t)\ e^{-n\beta_T cosht}dt - \frac{a_1}{2}\vec{p}_T.(\vec{\nabla}_T\tau_f)\int_0^\infty e^{-n\beta_T cosht}dt \\ &+\frac{a_2 m_T}{2}\int_0^\infty cosh(2t)e^{-n\beta_T cosht}dt + \frac{a_2 m_T}{2}\int_0^\infty e^{-n\beta_T cosht}dt \\ &-a_2\vec{p}_T.(\vec{\nabla}_T\tau_f)\int_0^\infty cosht\ e^{-n\beta_T cosht}dt + a_3 m_T\int_0^\infty cosht\ e^{-n\beta_T cosht}dt \\ &-a_3\vec{p}_T.(\vec{\nabla}_T\tau_f)\int_0^\infty e^{-n\beta_T cosht}dt].\end{aligned} \tag{E.13}$$

Using equation E.10 and the value of I_1 in the above equation we arrive at the final form of the invariant yield as,

$$\begin{aligned}\frac{dN_{neq}}{dyd^2p_T} = &\frac{g}{(\epsilon+p)T^2\left(2\pi\right)^3}\int\tau_f dxdy\sum_{n=1}^{\infty}(\mp1)^{n+1}e^{n\beta[\gamma\vec{p}_T\vec{v}_T+\mu]}[m_T(\frac{a_1}{4}k_3(n\beta_T) + \frac{3a_1}{4}k_1(n\beta_T) \\ &+\frac{a_2}{2}k_2(n\beta_T) + \frac{a_2}{2}k_0(n\beta_T) - \vec{p}_T.(\vec{\nabla}_T\tau_f)[\frac{a_1}{2}k_2(n\beta_T) + a_2k_1(n\beta_T) + (\frac{a_1}{2}+a_3)k_0(n\beta_T)]).\end{aligned}$$

Bibliography

[1] D. J. Gross and F. Wilczek, Phys. Rev. Lett. **30**, 1343 (1973).

[2] H. D. Politzer, Phys. Rev. Lett. **30**, 1346 (1973).

[3] Frank Wilczek, Fantastic Realities 49 Mind Journeys and A Trip to Stockholm. World Scientific.

[4] T. D. Lee and G. C. Wick, Phys. Rev. D **9**, 2291 (1974).

[5] M. Gyulassy and L. McLerran, Nucl. Phys. A **750**, 30 (2005) [nucl-th/0405013].

[6] J. C. Collins and M. J. Perry, Phys. Rev. Lett. **34**, 1353 (1975).

[7] E. V. Shuryak, Phys. Rept. **61**, 71 (1980).

[8] S. Bethke, Nucl. Phys. Proc. Suppl. **121**, 74 (2003) [hep-ex/0211012].

[9] S. Durr, Z. Fodor, J. Frison, C. Hoelbling, R. Hoffmann, S. D. Katz, S. Krieg and T. Kurth *et al.*, Science **322**, 1224 (2008) [arXiv:0906.3599 [hep-lat]].

[10] S. Borsanyi *et al.*, JHEP **1011**, 077 (2010) [arXiv:1007.2580 [hep-lat]].

[11] Z. Donko, P. Hartmann and G. J. Kalman, arXiv:0710.5229 [nucl-th].

[12] M. H. Thoma, J. Phys. G **31**, L7 (2005) [Erratum-ibid. **G31**, 539 (2005)] [arXiv:hep-ph/0503154].

[13] T. D. Lee, Nucl. Phys. A **750**, 1 (2005).

[14] J. Liao and E. Shuryak, Phys. Rev. C **75**, 054907 (2007) [arXiv:hep-ph/0611131].

[15] S. Mrowczynski and M. H. Thoma, Ann. Rev. Nucl. Part. Sci. **57**, 61 (2007) [arXiv:nucl-th/0701002].

[16] J. L. Nagle, Eur. Phys. J. C **49**, 275 (2007) [arXiv:nucl-th/0608070].

[17] E. Shuryak, hep-ph/0703208 [HEP-PH].

[18] http://qgp.phy.duke.edu/

[19] B. Abelev *et al.* [ALICE Collaboration], Phys. Rev. Lett. **105**, 252301 (2010) [arXiv:1011.3916 [nucl-ex]].

[20] H. Song, S. A. Bass and U. Heinz, Phys. Rev. C **83**, 024912 (2011) [arXiv:1012.0555 [nucl-th]].

[21] Z. W. Lin, C. M. Ko, B. A. Li, B. Zhang and S. Pal, Phys. Rev. C **72**, 064901 (2005) [arXiv:nucl-th/0411110].

[22] M. Bleicher *et al.*, J. Phys. G **25**, 1859 (1999) [arXiv:hep-ph/9909407].

[23] S. S. Adler *et al.* [PHENIX Collaboration], Phys. Rev. Lett. **91**, 072301 (2003) [arXiv:nucl-ex/0304022].

[24] B. B. Back *et al.* [PHOBOS Collaboration], Phys. Rev. Lett. **91**, 072302 (2003) [arXiv:nucl-ex/0306025].

[25] J. Adams *et al.* [STAR Collaboration], Phys. Rev. Lett. **91**, 072304 (2003) [arXiv:nucl-ex/0306024].

[26] I. Arsene *et al.* [BRAHMS Collaboration], Phys. Rev. Lett. **91**, 072305 (2003) [arXiv:nucl-ex/0307003].

[27] X. N. Wang and M. Gyulassy, Phys. Rev. Lett. **68**, 1480 (1992).

[28] I. Vitev and M. Gyulassy, Phys. Rev. Lett. **89**, 252301 (2002) [arXiv:hep-ph/0209161];

[29] M. Gyulassy, P. Levai and I. Vitev, Phys. Rev. Lett. **85**, 5535 (2000) [arXiv:nucl-th/0005032].

[30] X. -N. Wang, Phys. Rev. C **70**, 031901 (2004) [nucl-th/0405029].

[31] M. L. Miller, K. Reygers, S. J. Sanders and P. Steinberg, Ann. Rev. Nucl. Part. Sci. **57**, 205 (2007) [nucl-ex/0701025].

[32] B. Mohanty, New J. Phys. **13**, 065031 (2011) [arXiv:1102.2495 [nucl-ex]].

[33] B. I. Abelev *et al.* [STAR Collaboration], Phys. Rev. Lett. **97**, 152301 (2006) [arXiv:nucl-ex/0606003].

[34] A. Adare *et al.* [PHENIX Collaboration], Phys. Rev. C **83**, 024909 (2011) [arXiv:1004.3532 [nucl-ex]].

[35] A. Adare *et al.* [PHENIX Collaboration], Phys. Rev. Lett. **101**, 232301 (2008) [arXiv:0801.4020 [nucl-ex]].

[36] S. S. Adler *et al.* [PHENIX Collaboration], Phys. Rev. Lett. **96**, 202301 (2006) [nucl-ex/0601037].

[37] J. Adams *et al.* [STAR Collaboration], Phys. Lett. B **637**, 161 (2006) [arXiv:nucl-ex/0601033].

[38] J. Alam, P. Roy and A. K. Dutt-Mazumder, hep-ph/0604131.

[39] J. Y. Ollitrault, Phys. Rev. D **46**, 229 (1992).

[40] A. M. Poskanzer and S. A. Voloshin, Phys. Rev. C **58**, 1671 (1998) [arXiv:nucl-ex/9805001].

[41] J. Adams *et al.* [STAR Collaboration], Nucl. Phys. A **757**, 102 (2005) [nucl-ex/0501009].

[42] P. Huovinen, P. F. Kolb, U. W. Heinz, P. V. Ruuskanen and S. A. Voloshin, Phys. Lett. B **503**, 58 (2001) [arXiv:hep-ph/0101136].

[43] D. Molnar and S. A. Voloshin, Phys. Rev. Lett. **91**, 092301 (2003) [arXiv:nucl-th/0302014].

[44] T. Matsui and H. Satz, Phys. Lett. B **178**, 416 (1986).

[45] C-Y Wong, Introduction to High-Energy Heavy-Ion Collision, World Scientific.

[46] A. Adare *et al.* [PHENIX Collaboration], Phys. Rev. Lett. **98**, 232301 (2007) [nucl-ex/0611020].

[47] L. Yan, P. Zhuang and N. Xu, Phys. Rev. Lett. **97**, 232301 (2006) [nucl-th/0608010].

[48] J. Alam, S. Sarkar, P. Roy, T. Hatsuda and B. Sinha, Annals Phys. **286**, 159 (2001) [hep-ph/9909267].

[49] J. I. Kapusta, P. Lichard and D. Seibert, Nucl. Phys. A **544**, 485C (1992).

[50] R. Chatterjee, L. Bhattacharya and D. K. Srivastava, Lect. Notes Phys. **785**, 219 (2010) [arXiv:0901.3610 [nucl-th]].

[51] L. D. McLerran and T. Toimela, Phys. Rev. D **31**, 545 (1985).

[52] C. Gale and J. I. Kapusta, Phys. Rev. C **35**, 2107 (1987).

[53] R. Rapp and J. Wambach, Adv. Nucl. Phys. **25**, 1 (2000) [arXiv:hep-ph/9909229].

[54] A. Adare *et al.* [PHENIX Collaboration], Phys. Rev. Lett. **104**, 132301 (2010) [arXiv:0804.4168 [nucl-ex]].

[55] S. Turbide, R. Rapp and C. Gale, Phys. Rev. C **69**, 014903 (2004) [arXiv:hep-ph/0308085].

[56] J. Rafelski and B. Muller, Phys. Rev. Lett. **48**, 1066 (1982) [Erratum-ibid. **56**, 2334 (1986)].

[57] P. Koch, B. Muller and J. Rafelski, Phys. Rept. **142**, 167 (1986).

[58] J. Rafelski, Eur. Phys. J. ST **155**, 139 (2008) [arXiv:0710.1931 [nucl-th]].

[59] A. Shor, Phys. Rev. Lett. **54**, 1122 (1985).

[60] J. Cleymans and A. Muronga, Phys. Lett. B **388**, 5 (1996) [nucl-th/9607042].

[61] J. Cleymans, M. Marais and E. Suhonen, Phys. Rev. C **56**, 2747 (1997) [nucl-th/9705014].

[62] B. I. Abelev *et al.* [STAR Collaboration], Phys. Lett. B **673**, 183 (2009) [arXiv:0810.4979 [nucl-ex]].

[63] T. Akesson *et al.* [Axial Field Spectrometer Collaboration], Nucl. Phys. B **203**, 27 (1982) [Erratum-ibid. B **229**, 541 (1983)].

[64] F. Reif, Fundamental of statistical and thermal physics. McGraw-HILL Book Company.

[65] S. Jeon, Phys. Rev. D **52**, 3591 (1995) [arXiv:hep-ph/9409250].

[66] T. Schafer and D. Teaney, Rept. Prog. Phys. **72**, 126001 (2009) [arXiv:0904.3107 [hep-ph]].

[67] R. Kubo J. Phys. Soc. Jap. 12, 570 (1957); R. Kubo Rept. Prog. Phys. 29, 255 (1966).

[68] P. Kovtun, D. T. Son and A. O. Starinets, Phys. Rev. Lett. **94**, 111601 (2005) [arXiv:hep-th/0405231].

[69] S. Weinberg, Astrophys. J. **168**, 175 (1971).

[70] H. B. Meyer, Phys. Rev. Lett. **100**, 162001 (2008).

[71] A. Nakamura and S. Sakai, Phys. Rev. Lett. **94**, 072305 (2005) [hep-lat/0406009].

[72] P. Danielewicz and M. Gyulassy, Phys. Rev. D **31**, 53 (1985).

[73] H. Song, "Causal Viscous Hydrodynamics for Relativistic Heavy Ion Collisions," [arXiv:0908.3656 [nucl-th]].

[74] H. Niemi, G. S. Denicol, P. Huovinen, E. Molnar and D. H. Rischke, Phys. Rev. Lett. **106**, 212302 (2011) [arXiv:1101.2442 [nucl-th]].

[75] T. Hirano, P. Huovinen and Y. Nara, Phys. Rev. C **84**, 011901 (2011) [arXiv:1012.3955 [nucl-th]].

[76] H. Song, S. A. Bass, U. Heinz, T. Hirano and C. Shen, Phys. Rev. Lett. **106**, 192301 (2011) [arXiv:1011.2783 [nucl-th]].

[77] M. Luzum and P. Romatschke, Phys. Rev. Lett. **103**, 262302 (2009) [arXiv:0901.4588 [nucl-th]].

[78] M. Luzum and P. Romatschke, Phys. Rev. C **78**, 034915 (2008) [Erratum-ibid. C **79**, 039903 (2009)] [arXiv:0804.4015 [nucl-th]].

[79] R. S. Bhalerao, J. P. Blaizot, N. Borghini and J. Y. Ollitrault, Phys. Lett. B **627**, 49 (2005) [arXiv:nucl-th/0508009].

[80] P. Bozek, Phys. Rev. C **81**, 034909 (2010) [arXiv:0911.2397 [nucl-th]].

[81] G. S. Denicol, T. Kodama and T. Koide, J. Phys. G **37**, 094040 (2010) [arXiv:1002.2394 [nucl-th]].

[82] K. Dusling and D. Teaney, Phys. Rev. C **77**, 034905 (2008) [arXiv:0710.5932 [nucl-th]].

[83] A. K. Chaudhuri, arXiv:0801.3180 [nucl-th].

[84] V. Roy and A. K. Chaudhuri, Phys. Rev. C **85**, 024909 (2012) [arXiv:1109.1630 [nucl-th]].

[85] S. Z. Belenkij and L. D. Landau, Hydrodynamic theory of multiple production of particles, Nuovo Cimento, supplement, 3, 15 (1956).

[86] J. D. Bjorken, Phys. Rev. D **27**, 140 (1983).

[87] P. Benincasa, A. Buchel and A. O. Starinets, Nucl. Phys. B **733**, 160 (2006) [arXiv:hep-th/0507026].

[88] J. Noronha-Hostler, J. Noronha and C. Greiner, Phys. Rev. Lett. **103**, 172302 (2009) [arXiv:0811.1571 [nucl-th]].

[89] C. Eckart, Phys. Rev. **58**, 267 (1940).

[90] C. Eckart, Phys. Rev. **58**, 919 (1940).

[91] Landau L.D,and Lifshitz E.M. 1959. Fluid Mechanics, page 308-312.

[92] W. Israel and J. M. Stewart, Annals Phys. **118**, 341 (1979) ; Ann. Phys. (N.Y.) 100, 310 (1976).

[93] B. Betz, G. S. Denicol, T. Koide, E. Molnar, H. Niemi and D. H. Rischke, EPJ Web Conf. **13**, 07005 (2011) [arXiv:1012.5772 [nucl-th]].

[94] A. Muronga, Phys. Rev. C **76**, 014910 (2007) [nucl-th/0611091].

[95] A. Muronga, Phys. Rev. C **76**, 014909 (2007) [nucl-th/0611090].

[96] P. Romatschke, Int. J. Mod. Phys. E **19**, 1 (2010) [arXiv:0902.3663 [hep-ph]].

[97] W. A. Hiscock and L. Lindblom, Phys. Rev. D **31**, 725 (1985).

[98] I. Muller, Z. Phys. **198**, 329 (1967).

[99] M. Grmela and H. C. Ottinger, Phys. Rev. E **56**, 6620 (1997).

[100] S. R. de Groot, W. A. van Leeuwen, Ch. G. van weert. Relativistic Kinetic Theory, principles and applications, North-Holland Publishing Company.

[101] U. W. Heinz, H. Song and A. K. Chaudhuri, Phys. Rev. C **73**, 034904 (2006) [arXiv:nucl-th/0510014].

[102] R. Baier, P. Romatschke, D. T. Son, A. O. Starinets and M. A. Stephanov, JHEP **0804**, 100 (2008) [arXiv:0712.2451 [hep-th]].

[103] J. P. Boris and D. L. Book, J. Comput. Phys. **11**, 38 (1973).

[104] D. H. Rischke, S. Bernard and J. A. Maruhn, Nucl. Phys. A **595**, 346 (1995) [nucl-th/9504018].

[105] A. K. Chaudhuri and V. Roy, Phys. Rev. C **84**, 027902 (2011) [arXiv:1102.4936 [nucl-th]].

[106] L. D. McLerran and R. Venugopalan, Phys. Rev. D **49**, 3352 (1994) [arXiv:hep-ph/9311205].

[107] E. Iancu and R. Venugopalan, In *Hwa, R.C. (ed.) et al.: Quark gluon plasma* 249-3363 [hep-ph/0303204].

[108] B. Schenke, S. Jeon and C. Gale, Phys. Rev. Lett. **106**, 042301 (2011) [arXiv:1009.3244 [hep-ph]].

[109] V. Roy and A. K. Chaudhuri, Phys. Rev. C **81**, 067901 (2010) [arXiv:1003.5791 [nucl-th]].

[110] K. Aamodt *et al.* [ALICE Collaboration], Phys. Rev. Lett. **106**, 032301 (2011) [arXiv:1012.1657 [nucl-ex]].

[111] H. -J. Drescher, A. Dumitru, A. Hayashigaki and Y. Nara, Phys. Rev. C **74**, 044905 (2006) [nucl-th/0605012].

[112] Y. Aoki, G. Endrodi, Z. Fodor, S. D. Katz and K. K. Szabo, Nature **443**, 675 (2006) [arXiv:hep-lat/0611014].

[113] P. Huovinen and P. Petreczky, Nucl. Phys. A **837**, 26 (2010) [arXiv:0912.2541 [hep-ph]].

[114] Edward W. Kolb and Michael S. Turner, The Early Universe, Addison-Wesley.

[115] P. F. Kolb, J. Sollfrank and U. W. Heinz, Phys. Rev. C **62**, 054909 (2000) [hep-ph/0006129].

[116] F. Cooper, G. Frye and E. Schonberg, Phys. Rev. D**11**, 192 (1975).

[117] J. Sollfrank, P. Koch and U. W. Heinz, Phys. Lett. B **252**, 256 (1990).

[118] T. Hirano and K. Tsuda, Phys. Rev. C **66**, 054905 (2002) [nucl-th/0205043].

[119] V. Roy and A. K. Chaudhuri, Phys. Lett. B **703**, 313 (2011) [arXiv:1103.2870 [nucl-th]].

[120] F. Cooper and G. Frye, Phys. Rev. D **10**, 186 (1974).

[121] A. Muronga and D. H. Rischke, nucl-th/0407114.

[122] K. Adcox *et al.* [PHENIX Collaboration], Nucl. Phys. A **757**, 184 (2005).

[123] I. Arsene *et al.* [BRAHMS Collaboration], Nucl. Phys. A **757**, 1 (2005).

[124] A. K. Chaudhuri, Phys. Lett. **B681**, 418-422 (2009).

[125] T. Hirano, U. W. Heinz, D. Kharzeev, R. Lacey and Y. Nara, Phys. Lett. B **636**, 299 (2006).

[126] S. Sakai and A. Nakamura, PoSLAT **2007**, 221 (2007).

[127] F. Karsch, D. Kharzeev and K. Tuchin, Phys. Lett. B **663**, 217 (2008).

[128] J. I. Kapusta, arXiv:0809.3746 [nucl-th].

[129] S. Jeon, Phys. Rev. D **52**, 3591 (1995).

[130] A. Wiranata and M. Prakash, Nucl. Phys. A **830**, 219C (2009).

[131] M. Prakash, M. Prakash, R. Venugopalan and G. Welke, Phys. Rept. **227**, 321 (1993).

[132] K. Paech and S. Pratt, Phys. Rev. C **74**, 014901 (2006).

[133] G. Torrieri, B. Tomasik and I. Mishustin, Phys. Rev. C **77**, 034903 (2008).

[134] A. Monnai and T. Hirano, Phys. Rev. C **80**, 054906 (2009).

[135] K. Dusling and T. Schaefer, arXiv:1109.5181 [hep-ph].

[136] W. Israel, Nonstationary Irreversible Thermodynamics: A Causal Relativistic Theory, Annals of Physics 100,310-331 (1976).

[137] A. Muronga, Phys. Rev. C **76**, 014909 (2007).

[138] E. Molnar, H. Niemi and D. H. Rischke, Eur. Phys. J. C **65**, 615 (2010).

[139] G. S. Denicol, T. Kodama, T. Koide and Ph. Mota, Phys. Rev. C **80**, 064901 (2009).

[140] D. Kharzeev and K. Tuchin, JHEP **0809**, 093 (2008).

[141] J. W. Chen and J. Wang, Phys. Rev. C **79**, 044913 (2009).

[142] D. Davesne, Phys. Rev. **C53**, 3069-3084 (1996).

[143] T. Hirano and Y. Nara, Phys. Rev. C **79**, 064904 (2009).

[144] P. Bozek, arXiv:1110.6742 [nucl-th].

[145] V. Roy and A. K. Chaudhuri, Phys. Rev. C **81**, 067901 (2010).

[146] P. F. Kolb, U. W. Heinz, P. Huovinen, K. J. Eskola and K. Tuominen, Nucl. Phys. A **696**, 197 (2001).

[147] X. G. Huang, T. Kodama, T. Koide and D. H. Rischke, Phys. Rev. C **83**, 024906 (2011).

[148] M. Luzum and J. -Y. Ollitrault, Phys. Rev. C **82**, 014906 (2010).

[149] A. K. Chaudhuri, J. Phys. G **G37**, 075011 (2010).

[150] S. S. Adler *et al.* [PHENIX Collaboration], Phys. Rev. C **71**, 034908 (2005) [Erratum-ibid. C **71**, 049901 (2005)] [nucl-ex/0409015].

[151] S. S. Adler *et al.* [PHENIX Collaboration], Phys. Rev. C **69**, 034910 (2004) [nucl-ex/0308006].

[152] K. Aamodt *et al.* [ALICE Collaboration], Phys. Lett. B **696**, 30 (2011) [arXiv:1012.1004 [nucl-ex]].

[153] A. Adare *et al.* [PHENIX Collaboration], Phys. Rev. Lett. **107**, 252301 (2011) [arXiv:1105.3928 [nucl-ex]].

[154] K. Aamodt *et al.* [The ALICE Collaboration], Phys. Rev. Lett. **105** (2010) 252302 [arXiv:1011.3914 [nucl-ex]].

[155] M. I. Gorenstein, M. Hauer and O. N. Moroz, Phys. Rev. C **77**, 024911 (2008) [arXiv:0708.0137 [nucl-th]].

[156] O. N. Moroz, arXiv:1112.0277 [hep-ph].

[157] J. Xu and C. M. Ko, Phys. Rev. C **84**, 014903 (2011) [arXiv:1103.5187 [nucl-th]].

[158] S. Afanasiev *et al.* [PHENIX Collaboration], Phys. Rev. C **80**, 024909 (2009) [arXiv:0905.1070 [nucl-ex]].

[159] P. Bozek, Phys. Rev. C **83**, 044910 (2011) [arXiv:1012.5927 [nucl-th]].

[160] T. Hirano and Y. Nara, Phys. Rev. C **79**, 064904 (2009) [arXiv:0904.4080 [nucl-th]].

[161] B. I. Abelev *et al.* [STAR Collaboration], Phys. Rev. C **77**, 054901 (2008) [arXiv:0801.3466 [nucl-ex]].

[162] P. Bozek, Phys. Lett. B **699**, 283 (2011) [arXiv:1101.1791 [nucl-th]].

[163] A. Kisiel, T. Taluc, W. Broniowski and W. Florkowski, Comput. Phys. Commun. **174**, 669 (2006) [nucl-th/0504047].

[164] B. Schenke, S. Jeon and C. Gale, Phys. Lett. B **702**, 59 (2011) [arXiv:1102.0575 [hep-ph]].

[165] R. A. Lacey *et al.*, Phys. Rev. Lett. **98**, 092301 (2007) [arXiv:nucl-ex/0609025].

[166] S. Gavin and M. Abdel-Aziz, Phys. Rev. Lett. **97**, 162302 (2006) [arXiv:nucl-th/0606061].

[167] P. Romatschke and U. Romatschke, Phys. Rev. Lett. **99**, 172301 (2007) [arXiv:0706.1522 [nucl-th]].

[168] A. Adare *et al.* [PHENIX Collaboration], Phys. Rev. Lett. **98**, 172301 (2007) [nucl-ex/0611018].

[169] H. van Hees, M. Mannarelli, V. Greco and R. Rapp, Eur. Phys. J. C **61**, 799 (2009) [arXiv:0808.3710 [hep-ph]].

[170] Z. Xu and C. Greiner, Phys. Rev. Lett. **100**, 172301 (2008) [arXiv:0710.5719 [nucl-th]].

[171] H. B. Meyer, Phys. Rev. D **76**, 101701 (2007) [arXiv:0704.1801 [hep-lat]].

[172] N. Demir and S. A. Bass, Phys. Rev. Lett. **102**, 172302 (2009) [arXiv:0812.2422 [nucl-th]].

[173] D. E. Kharzeev, L. D. McLerran and H. J. Warringa, Nucl. Phys. A **803**, 227 (2008) [arXiv:0711.0950 [hep-ph]].

[174] F. Becattini, F. Piccinini and J. Rizzo, Phys. Rev. C **77**, 024906 (2008) [arXiv:0711.1253 [nucl-th]].

[175] J. R. Bhatt, H. Mishra and V. Sreekanth, Phys. Lett. B **704**, 486 (2011) [arXiv:1103.4333 [hep-ph]].

[176] B. Mohanty [STAR Collaboration], J. Phys. G **38**, 124023 (2011) [arXiv:1106.5902 [nucl-ex]].

[177] D. Kharzeev and M. Nardi, Phys. Lett. B **507**, 121 (2001).

[178] B. B. Back *et al.* [PHOBOS Collaboration], Phys. Rev. C **70**, 021902 (2004).

[179] P. F. Kolb and U. Heinz, in *Quark-Gluon Plasma 3*, edited by R. C. Hwa and X.-N. Wang (World Scientific, Singapore, 2004), p. 634.

[180] M. Cheng *et al.*, Phys. Rev. D **77**, 014511 (2008).

[181] L. D. McLerran and R. Venugopalan, Phys. Rev. D **49**, 2233 (1994) [arXiv:hep-ph/9309289].

[182] D. Kharzeev, E. Levin and M. Nardi, Nucl. Phys. A **730** (2004) 448 [Erratum-ibid. A **743** (2004) 329].

[183] A. Dumitru, E. Molnar and Y. Nara, Phys. Rev. C **76**, 024910 (2007) [arXiv:0706.2203 [nucl-th]].

[184] A. Adare *et al.* [PHENIX Collaboration], Phys. Rev. Lett. **105**, 062301 (2010) [arXiv:1003.5586 [nucl-ex]].

[185] S. S. Adler *et al.* [PHENIX Collaboration], Phys. Rev. C **69**, 034909 (2004) [arXiv:nucl-ex/0307022].